Modelling and simulation of compacting sedimentary basins



Jane J. E. Lee
Mansfield College
University of Oxford

A thesis submitted for the degree of
Doctor of Philosophy
Trinity term 2019

Abstract

Hydrocarbons are found in rocks within sedimentary basins below the Earth's surface. Whilst they remain a primary energy source, many hydrocarbon fields are nearing depletion, and new, more advanced exploration and recovery techniques are required to find new reserves and to sustain production. One such technique aims at predicting the evolution of pressure, porosity, and temperature profiles within basins from past to present, to determine whether there is potential for hydrocarbon generation in a certain location and also to reduce drilling risk.

In this thesis, we identify and mathematically model the primary geological processes within a sedimentary basin. We develop a fundamental model which describes both the mechanical and chemical compaction of sediments, and their influence on the porosity, pressure, and temperature profiles. We write our model in a general form which then sets up the framework on which we can add geological features, such as sills and fault lines. Such a generalised model, which can include these features in multiple dimensions, is rarely seen in literature.

We use the finite element method to develop a solver which can tackle our full model in multiple dimensions, and we test the validity of the solver through the method of manufactured solutions and error analysis. We discuss additional numerical techniques that can be used to model the deforming basin with respect to compaction and sedimentation. Our model is solved for the simplest case first, before we present simulations for varying geological situations. We examine the effects of a constant versus a porosity-dependent permeability model, varying rock viscosity values, different compaction models, and mechanical or chemical compaction (the latter of which is frequently neglected in literature and in industry). Then, we present simulations for basins in the presence of complex geological features, such as laterally varying stresses, faults, and sills. Finally, we summarise our key findings.

Acknowledgements

Whilst only my name appears on the front of this thesis, there are countless numbers of individuals and groups of people that have contributed towards its completion.

First and foremost, I want to thank my supervisors: Kathryn Gillow, Robert Van Gorder, and Jonathan Whiteley. Kathryn, you have been more than a supervisor since my Master's degree, and I am grateful for all the mental and mathematical support you have given me over the years. Not only have you patiently supervised my research, but you have been a huge mentor. Robert, your help and advice have been unceasingly valuable, and I cannot put into words how much I appreciate the number of hours, whatever timezone you may be in, that you have spent on supervising my research. You went above and beyond the normal expectations of an academic supervisor throughout the many years I worked with you. Jonathan, I thank you for your unparalleled knowledge in areas that I sometimes needed a lot of help with, and your patience and time in this project have proved to be invaluable. To all three of you, I am honoured to be able to say that I was your doctorate student, and I owe this thesis to you.

In addition to my academic supervisors, I would like to thank my supervisors at PDS: Remco Groenenberg, Sebastiaan Kole, Konstantinos Leventis, and William Senior. In particular, my sincerest gratitudes go to Bill, who spent hours alongside his normal work schedule to discuss my project, and to Remco, who provided me with crucial geological knowledge. Further, I would like to thank Steve Daum for his guidance and personal advice, as well as PDS' financial support over the years.

I have been lucky to have this unbelievably fantastic team, but there are several other individuals who have helped this thesis to be shaped. In particular, I would like to thank Chris Breward, Chris Farmer, Ian Hewitt, and Colin Please, for their selfless support and advice on my model and

more. Much of the numerical discussions concerning `deal.ii` came from personal communication with Wolfgang Bangerth and other developers of the package. I sincerely thank each and every one of you that took the time to advise me on the numerical developments in this thesis.

Besides the incredible academic help I had, I am truly grateful for the amount of administrative support I had through many ups and downs in my doctorate career. To Laura and Amanda, you were beyond understanding and sympathetic, however small or large the issues were. To Sandy, I cannot put into words how significant your presence has been during my time at Oxford and I cannot thank you enough.

Finally to those who stuck by me, holding my hand and head throughout this all, I thank you, and I feel so grateful to have you all in my life. To Ozzy and Graham, thank you for enduring me all those years, giving me endless mathematical and personal advice and confidence, supporting me whatever the cause, and sticking up for me. To Niall, thanks for helping me even after you left, and for all the memories of grinding through into the early mornings together that pushed me to get to the end. To Guy, Sam, Johnny, and Tiff, thank you for being the best housemates and friends anyone could ask for. To Mark Bellamy, thank you for pulling me out of a dark place and helping me better structure all aspects of my life. To Christina, Minty, Cat, the rest of my LBs, and all my Blues, KLA, and Park End comrades, thank you for helping me to de-stress and brighten my days and nights. To Vincent, thank you for making sure I eat, and for your sincere and genuine motivation throughout my research. To my parents, thank you for just having my best interest at heart. To my brother, I thank you for true unconditional love and for non-judgemental support. You're the best brother anyone could ask for. To Josh, you have had to deal with the craziest of all my insanities and the biggest of my ups and downs. You may not understand a single page of this thesis, but you have been my rock, and your support got the words on the paper. Finally and above all, my utmost thanks to God, to whom I give all the glory, for making all this happen.

Contents

1 Introduction **1**

1.1 Geological background 1

1.1.1 Compaction and sedimentation 2

1.1.2 Geological features in sedimentary basins 3

1.2 Existing modelling work 4

1.2.1 Early gravitational or mechanical compaction models 4

1.2.2 Pressure Solution 8

1.2.3 Other compaction models 10

1.2.4 Modelling of geological phenomena 11

1.2.5 Complete pressure-temperature models 12

1.3 Existing work and interests of our industrial partner 13

1.4 Aims of thesis 14

1.4.1 Multi-dimensional coupled model 15

1.4.2 Behaviour of a more complete model 17

1.4.2.1 Effect of permeability on compaction 17

1.4.2.2 A new model for porosity incorporating chemical compaction 17

1.4.2.3 Viscosity effects on the complete model 18

1.4.3 Modelling of faults and other geological features 18

1.4.3.1 Lateral stresses in the basin 18

1.4.3.2 Faults 19

1.4.3.3 Sills 19

1.5 Structure of thesis 19

2 A mathematical model for a compacting basin **21**

2.1 Assumptions and domain setup 22

2.2 A model for a compacting basin 23

2.2.1 Model derivation 24

2.2.1.1 Conservation of mass . . . 24
2.2.1.2 Conservation of momentum . . . 25
2.2.1.3 Compaction equation . . . 27
2.2.1.4 Conservation of heat energy . . . 30
2.2.2 Discussion of boundary and initial conditions . . . 30
2.2.3 Summary of model . . . 31
2.3 Physical properties and constitutive equations . . . 33
2.3.1 Summary of material properties . . . 33
2.3.2 Constitutive equations . . . 34
2.3.2.1 Permeability model . . . 34
2.3.2.2 Rock viscosity model . . . 36
2.3.2.3 Rock rheology models for deviatoric stress . . . 36
2.3.2.4 Thermal conductivity . . . 37
2.3.2.5 Modelling parameters in the compaction equation . . . 38
2.4 Nondimensionalisation and scaling . . . 39
2.4.1 Nondimensionalisation . . . 39
2.4.2 Summary of dimensionless parameters and groups . . . 42
2.5 Summary of Chapter 2 . . . 43
2.5.1 The developed model . . . 43
2.5.2 Relevance to existing models . . . 44

3 Numerical modelling of a basin and solver development 47
3.1 Model decomposition . . . 47
3.1.1 Derivation of rock and fluid subsystems . . . 48
3.1.1.1 Rock subsystem equations . . . 48
3.1.1.2 Fluid subsystem equations . . . 49
3.1.2 Definition of each subsystem . . . 49
3.1.3 Solution sequence . . . 51
3.2 Numerical method and tools . . . 53
3.2.1 A brief introduction to `deal.ii` . . . 53
3.2.2 The finite element method . . . 54
3.3 Weak forms and system discretisation . . . 56
3.3.1 Discretised rock equations . . . 56
3.3.2 Discretised fluid problem . . . 58
3.3.3 Discretisation of the porosity subsystem . . . 60
3.3.4 Discretisation of the temperature subsystem . . . 61

3.4 Solver construction and method of manufactured solutions 62
3.5 Verification of solver 62
3.5.1 Error analysis and convergence 63
3.5.2 Rock subsystem 64
3.5.3 Fluid subsystem 66
3.5.4 Porosity subsystem 68
3.5.4.1 Spatial convergence 68
3.5.4.2 Temporal convergence 69
3.5.5 Temperature subsystem 70
3.5.5.1 Spatial convergence 71
3.5.5.2 Temporal convergence 71
3.6 Compacting domain 72
3.7 Sedimentation 74
3.8 Summary of Chapter 3 76

4 Simulation results using the full solver **77**
4.1 Solver parameters 77
4.1.1 Definition of parameters 77
4.2 Base results 80
4.3 Three-dimensional results 82
4.4 Results neglecting sedimentation 82
4.4.1 Comparison to results with sedimentation 85
4.5 Constant permeability models 86
4.5.1 Comparison between results for different values of λ 87
4.5.1.1 Porosity 87
4.5.1.2 Pore fluid pressure 90
4.5.2 Summary of results using constant permeability 91
4.6 Porosity-dependent permeability model 93
4.7 Different compaction mechanisms 94
4.8 The viscosity effect 96
4.9 Different effective stress models 98
4.10 Summary of Chapter 4 100
4.10.1 Base results for sedimentation and compaction 100
4.10.2 The effect of λ 100
4.10.3 Comparison between constant and porosity-dependent permeability models 102

4.10.4 Mechanical and chemical compaction . . . 102
4.10.5 The viscosity effect . . . 103
4.10.6 Different effective stress models . . . 103
4.10.7 Concluding remarks . . . 104

5 Compacting basins in the presence of complex geological features 106
5.1 Laterally varying stresses . . . 106
5.1.1 Summary of the effect of varying rock stress conditions . . . 109
5.2 Geological faults . . . 110
5.2.1 Modelling of faults . . . 111
5.2.2 Grid refinement . . . 112
5.2.3 Vertical faults . . . 113
5.2.4 Multidirectional faults . . . 117
5.2.5 Discussion of results . . . 120
5.3 Sills and dykes . . . 120
5.3.1 Simulation results with a sill intrusion . . . 121
5.3.1.1 Temperature results . . . 121
5.3.1.2 Porosity results . . . 125
5.3.2 Summary of simulations with a sill . . . 126
5.4 Summary of Chapter 5 . . . 127

6 Conclusions 129
6.1 Summary of derived model and solver . . . 129
6.2 Summary of results and findings . . . 130
6.3 Possible directions for future work . . . 134

Bibliography 137

Chapter 1

Introduction

Hydrocarbons are found in rocks within basins below the Earth's surface. They remain a primary energy source in the world, yet the oil and gas industry faces many technological challenges in the exploration and recovery of hydrocarbons (Campbell and Laherrère, 1998). Many known reservoirs and hydrocarbon fields are becoming depleted, with production significantly in decline with current technological resources (Bentley, 2002). It is therefore of interest to develop advanced recovery techniques to acquire more oil out of reservoirs previously considered fully depleted. Furthermore, the industry must now explore more challenging environments, possibly deeper into the subsurface where higher pressure and temperature regimes exist, or in areas with more complex geological settings. A further search for oil and gas in the subsurface hence requires essential advances, in order to develop efficient and accurate information on reservoirs within sedimentary basins for their further exploration, and to meet future demands of hydrocarbons (Anderson, 1998).

1.1 Geological background

A sedimentary basin is a vast depressed region on Earth which has filled with sediments over millions of years, formed by subsidence due to processes such as sediment loading and tectonism, such as oceanic rifting, subduction, and continental collision (Allen and Allen, 2013). A basin can be more than 15km in depth, with a lateral radius ranging from 10km to 1000km (Hantschel and Kauerauf, 2009). These sedimentary basins are made up of fluid trapped in deposited layers consisting of many different sediments. Over time, the sediments and the inner fluid compact due to the accumulated weight from slowly depositing sediments along with other chemical processes. The trapped fluid can become pressurised, depending on the rate of deposition, and by natural compaction purely due to weight. Chemical reactions between the sediments and fluid,

as well as the changes in temperature (mainly due to the heat flux supplied to the bottom of the basin from the Earth's core), can also add to the compaction process.

A crucial component in basin and petroleum systems modelling (BPSM) is to understand the pore pressure, porosity, and temperature profiles within a sedimentary basin, which requires a thorough analysis of the mechanisms and geological phenomena underlying the formation of the basin (Yalçin, 1991). The knowledge of the pore pressure and temperature histories of a basin in particular then allows one to assess the potential for the generation of hydrocarbons and their accumulation into reservoirs within sedimentary basins. Ultimately, the aim of BPSM is to predict the location of such accumulations, their volumes, and the properties of the fluids in the reservoirs.

Using current data in existing sedimentary basins, we are able to recreate the growth and evolution of a sedimentary basin, and obtain an estimation of the pressure, porosity, and temperature profiles of the basin since its genesis. A sedimentary basin is subject to multiple geological phenomena throughout its lifetime (Hantschel and Kauerauf, 2009). It is important to examine the effects of each feature on the basin and its pressure, temperature, and porosity profiles, in order to explore further hydrocarbon potential and for safe recovery techniques. For example, some geological features such as salt domes can create impermeable layers within the basin, between which the pressure of the fluids trapped in the basin can become extremely large, thereby making it dangerous to drill into without further precaution from the pressure data. We now discuss some of the most common geological phenomena and features.

1.1.1 Compaction and sedimentation

The mechanisms and geological phenomena involved in an evolving basin are understandably complex. The primary processes that cause a variation in pressure in a basin, in particular, are sedimentation and subsequent compaction (Allen and Allen, 2013). Compaction is caused by many various phenomena, but the two largest contributors are mechanical and chemical compaction.

Mechanical compaction results in a change in pressure due to the overburden weight from continuous sediment deposition (loading), or due to a simple rearrangement of the sedimentary grains at the microscopic scale. The porosity in the sediment matrix is then decreased, and in cases where compaction takes place faster than the rate at which fluid can be expelled from the pores, the fluid pressure increases from its hydrostatic state. The difference between the increased pore pressure and the hydrostatic pressure in the pores is called overpressure.

Chemical compaction, on the other hand, can occur due to geochemical reactions (Hantschel and Kauerauf, 2009) such as 'pressure solution', where sediments dissolve at grain-to-grain contact points under pressure and precipitate elsewhere. This is one of the most significant chemical compaction mechanisms, though is said to take place deeper in the basin beyond a depth of 1.5km (Angevine and Turcotte, 1983).

There are many other (albeit minor) contributing factors to chemical compaction. Aquathermal fluid expansion is where a fluid expands due to temperature variations (Walderhaug et al., 2001; Luo and Vasseur, 1992). Hence, the expansion of fluid can cause further overpressure due to the increase in volume within the same volume of rock matrix. Diagenesis is the process where sediments react and form into other types of sediments, whilst sometimes simultaneously releasing extra fluid, and thereby affecting the pore pressure. New materials can deposit or form within the matrix from processes like cementation, subsequently decreasing porosity and hence causing overpressure, and this is said to take place in depths around 3km-4.5km (Bjørlykke and Egeberg, 1993).

Sedimentation takes place sporadically throughout geological times. The basin is able to grow and become deeper due to this process. Depending on the geological period, different types of rocks are formed on top of each layer and this depends on the sediments being deposited. It is sedimentation that provides a constant feed of overlying weight to the basin, thereby allowing compaction to take place over a long period of time.

1.1.2 Geological features in sedimentary basins

Besides compaction due to internal processes, there are many other external geological phenomena which may cause the basin geometry to change, further affecting the pressure and temperature within it. Processes brought about by tectonism can cause the rock layers to crack, causing large discontinuities in the rock in basins. These can cause fault lines along which the portion of the basin may further subside (see Figure 1.1). This subsidence, as well as the fault lines themselves, will affect the fluid and rock movement, and consequently affect the pressure, temperature, and porosity.

Sills are magmatic intrusions which are caused by magma creeping through fault lines, or from dykes (vertical intrusions), and other fractures in the basin. Sills occur in the horizontal orientation, and create new layers between rocks. Sills can be as thin as a few centimetres, to as large as hundreds of metres thick. These magmatic intrusions generate a significant source of heat, thereby affecting the temperature



Figure 1.1: Faults seen in Arches National Park in Utah. The sedimentary layers can be seen to have displaced along each fault line. Photo is credited to Recker (2013).



Figure 1.2: Illustration of a sill in Svalbard, Norway. The dark layers are the sill intrusions in the basin made up of limestone (white layers). Photo credited to The Norwegian Polar Institute.

within the surrounding rocks. This in turn can affect the porosity and pressures within the rock and fluid. An example of a basin with sills is shown in Figure 1.2.

1.2 Existing modelling work

There exists a vast amount of literature examining the evolution of sedimentary basins in multiple fields — from geology and geochemistry, to mathematics and computational science. It is of wide interest to understand the pressure, porosity, and temperature evolution within a basin since its first deposition. We present a review of the most prominent works in the study of compacting basins in this section.

1.2.1 Early gravitational or mechanical compaction models

The initial stages of modelling compaction focussed purely on the reduction of porosity by itself, rather than also modelling the pressure and other factors in the basin. These simple compaction models have been discussed at length since the 1920s. Hedberg (1926) notes: "Early suggestions of the possible importance of compaction as a source of folding aroused widespread interest, and not many writers have given the subject consideration and many oil field structures have been attributed either to lateral variation in the compressibility of sedimentary strata or to the settling of sediments over buried hills."

Following this initial suggestion, authors began to develop porosity-depth relations for compaction, with Athy (1930) and Hedberg (1926, 1936) being the forerunners in this field. Athy (1930), noting that few quantitative data on the relationship between material parameters and compaction exist, found the well-known porosity-depth model via efficient laboratory methods (Athy, 1930), given by

$$\phi = \phi_0 \exp(-bz), \tag{1.2.1}$$

where ϕ is the porosity, ϕ_0 is the 'average porosity of surface clays', b is some fitted constant found empirically depending on the rock type, and z is the depth measured from the top surface of the basin. The model he derived originates from data taken from basins in north-central Oklahoma. This empirical model is given theoretical support by Korvin (1984), who mathematically derived Athy's law as above using statistical physics and assuming that compaction is caused by gravitational and mechanical compaction only.

Similarly, using data from Venezuela, Hedberg (1936) later developed a porosity-pressure relation at various depths. Casting doubt on the accuracy of depth-porosity relationships, the author argued that porosity is fundamentally more dependent on pressure. Dividing observations into three distinct stages of increasing pressure, the author analysed the data and speculated the main causes for a reduction in porosity. He approximated the general relationship between pressure and porosity by the exponential equation (Hedberg, 1936)

$$\phi = 40.22(0.9998)^p, \tag{1.2.2}$$

where p is the pressure in pounds per square inch.

In more recent years, there have been many developments to the early compaction models, since, though widely accepted and used, Athy's law as given in (1.2.1) has been vastly critiqued by many authors. Some claim that this function is not recommended as it is said to be only valid for basins at hydrostatic pressure (King Hubbert and Rubey, 1959), and it is said to result in the over-prediction of excess pressures in the presence of compaction (Wangen, 1992). It is also clear that it does not incorporate any effects of loading and excess pressure. Indeed, it is also claimed that the model is only valid for shallow depths of around 1–2km, much shallower than most geological basins.

Instead, many variations of Athy's law are used when modelling sediment compaction, with many authors choosing to replace the depth in (1.2.1) with the vertical

effective stress, σ, which is defined as the difference between the overburden pressure and pore pressure, such that

$$\phi = \phi_0 \exp(-b\sigma), \tag{1.2.3}$$

where b here is another appropriate constant coefficient. This is then able to incorporate any loading effects and porosity changes caused by sedimentary processes.

Schneider et al. (1996) used this Athy-type formula in their porosity-effective stress relationship using a constant coefficient for the value of b in (1.2.3). However, many authors choose to use the functional form,

$$\phi = \phi_0 \exp(-b(\phi)\sigma). \tag{1.2.4}$$

For example, Giles et al. (1998) propose

$$b(\phi) = \frac{c}{(\rho_b(\phi) - \rho)g}, \tag{1.2.5}$$

with constant rock density assuming little or no chemical diagenesis, based on the model by Sclater and Christie (1980). In the above, c is a constant porosity compressibility, ρ_b is the bulk sediment density, ρ is the water density which the authors suggest depend on the temperature and salinity, and g is the gravitational coefficient.

Other early empirical models and analysis from observations regarding porosity-depth-pressure relations are chronologically presented in Rieke and Chilingarian (1974). A thorough discussion on the theoretical and empirical observations on porosity-depth and porosity-effective stress relationships can be found in Giles et al. (1998).

Since the development of numerous compaction models, a more complete one-dimensional modelling and theoretical analysis of the compaction process using arguments from first principles have been well-documented by various authors. Note that most of the models are in a single space dimension only, since in general, mechanical compaction on its own is essentially a vertical process. Temperature considerations are usually not included in these porosity-pressure models.

One of the first notable transient consolidation models considering mechanical compaction was devised by Smith (1971). Considering a few different geological situations, Smith was able to model the porosity of a layer composed of a single lithology. Smith began from mass conservation arguments coupled with Darcy's law, and used Athy's compaction model (1.2.1) as before, and a Kozeny-Carman type permeability model for the permeability, k, taking $k \sim \phi^a/(1-\phi)^c$, where the constants a and c are found empirically and depend on the rock material (Smith, 1971; Costa, 2006; Pirson, 1963). Smith then derived the following time-depth-dependent governing

equation for the porosity of a shale layer with an impermeable base and constant sediment deposition:

$$\frac{1}{1-\phi}\int_{z=0}^{Z}\frac{\partial\phi}{\partial t}\,dz=\frac{kg(\rho_s-\rho_f)(1-\phi)}{\mu b\phi}\left(\frac{\partial\phi}{\partial z}-b\phi\right), \tag{1.2.6}$$

where $b=1.4\times10^{-3}\,\mathrm{m}^{-1}$ which Smith took from Athy (1930). Here, Z is the depth of the sediments with $z=0$ denoting the bottom, μ is the viscosity, ρ_s and ρ_f are the solid and fluid densities, respectively, and b is the compaction coefficient as before. Alternatively, for a volume of sediments overlying a hydrostatically pressured unit, the porosity profile can be determined from

$$\log\frac{\phi_T}{\phi_0}-(\phi_T-\phi_0)=b\int_{z=0}^{T}(1-\phi)\,dz, \tag{1.2.7}$$

where ϕ_T and ϕ_0 are the porosities at the top and the bottom of the shale layer, and $z=T$ corresponds to the top of the layer. This can be further extended to incorporate the porosity profile after the deposition of a succeeding layer on top of the shale unit, by adding the term

$$b\frac{\rho_r-\rho_f}{\rho_s-\rho_f}D \tag{1.2.8}$$

to the right hand side of (1.2.7), where ρ_r is the bulk density of the topmost unit, and D is its thickness.

Thereafter, a nonlinear porosity equation for a continuously depositing unit was formed by Audet and McConnell (1992). Here, they used the soil mechanics compaction theory (so that the effective stress is a function of the porosity) coupled with an exponential permeability model, and began their simulation at a time where no sediments have been deposited. Analysis from conservation of mass and momentum with Darcy's law, led to a dimensionless governing law:

$$\frac{\partial\phi}{\partial t}=-\lambda\frac{\partial}{\partial z}\left[(1-\phi)^2k(\phi)\left(1+\frac{1}{1-\phi}\frac{\partial\sigma}{\partial\phi}\frac{\partial\phi}{\partial z}\right)\right], \tag{1.2.9}$$

where λ is a dimensionless parameter referred to as the sedimentation parameter, given by

$$\lambda=\frac{\kappa_0}{V_0}\left(\frac{\rho_s}{\rho_f}-1\right), \tag{1.2.10}$$

where κ_0 is the surface hydraulic conductivity and V_0 is a characteristic velocity. Note that following Terzaghi's principle, Audet and McConnell (1992) were able to find the pore pressure given some depth via the effective stress, as well as the velocity profiles. The resulting porosity and pressure profiles from this model gave physically

realistic results — for a high sedimentation parameter denoting high permeability, the pressure remained closer to hydrostatic, with a low sedimentation parameter creating excess pore pressure. This was the expected result, since fluid can migrate out of the unit more easily with a higher permeability, and therefore high pressures in the pores are not as easily maintained. Hence, Audet and McConnell (1992) were able to characterise how the compaction is affected by the material properties through a single dimensionless parameter.

Audet and Fowler (1992) and Fowler and Yang (1998) derived a similar model to (1.2.9), incorporating the elastic rheology of the sediments via strain-stress tensors, and arrived at a slightly modified dimensionless parameter, λ, defined to be

$$\lambda = \frac{k_0(\rho_s - \rho_f)g}{\mu \dot{m}_s^0}, \tag{1.2.11}$$

where k_0 is a suitable scaling for the permeability and $\dot{m}_s^0$ is a typical value of sedimentation rate. With this definition of λ, they expected that $\lambda = 1$ defined a transition zone between fast and slow sedimentation. In fact, Fowler and Yang (1998) were able to find asymptotic solutions for large and small λ. Qualitatively, they found that in the slow compaction limit of λ smaller than 1, the sediments were deposited quickly enough for the porosity to remain at the depositional value except within a thin region at the base of the unit. On the other hand, for large λ, the porosity profile corresponded to that of Athy's (1.2.1), and the pore pressure was near hydrostatic, for sufficiently small times. Gutierrez and Wangen (2005) found similar physical results, but using a logarithmic compaction model and an exponential permeability model.

1.2.2 Pressure Solution

The geological term called 'pressure solution' is a common phenomenon within basins whereby grains dissolve upon contact with other grains under high pressure and precipitate elsewhere in the available pore space. This rearrangement in the porous matrix can lead to a reduction in porosity and potential excess pressure. Pressure solution is usually thought to be a viscous compaction process.

Fowler and Yang (1999) presented a comprehensive viscous model in their paper, in which they claimed that at depths greater than 1km and around 4.5km, the process of pressure solution becomes significant and the compaction changes from an elastic one to a viscous one. The main difference between this model and the purely elastic model discussed in the previous section was the inclusion of the rheological constitutive and

compaction laws:

$$-\dot{\epsilon}_{ii} = \frac{1}{\xi} p_e, \tag{1.2.12}$$

where $\dot{\epsilon}_{ii}$ is the trace of the strain rate tensor $\dot{\epsilon}_{ij}$, ξ is a parameter defined by

$$\xi = \frac{\rho_s R T \bar{d}^3}{16 \nu_m M_s c_0 w D_{gb}}, \tag{1.2.13}$$

and p_e is the effective pressure which is related to the solid velocity $\mathbf{u}$ by

$$p_e = -\xi \nabla \cdot \mathbf{u}. \tag{1.2.14}$$

Here, R is the gas constant, T is the absolute temperature, $\bar{d}$ is the average grain diameter, ν_m is the molar volume of water, M_s is the molecular weight of quartz, c_0 is the equilibrium concentration of the material, and D_{gb} is the grain boundary diffusion coefficient along the grain contact boundaries of width w.

The dimensionless parameter characterising compaction remained the same as in (1.2.11), and asymptotic solutions could be found again for slow compaction and fast compaction. The results, including the transition region into excess pressure generation, of the former were similar to that of a purely elastic compaction. However, whilst the elastic fast compaction case gave an exponential function of depth (Fowler and Yang, 1998), the porosity profile was concave near the top of the sediment domain.

Extending this to include temperature effects in a sedimentary layer undergoing compaction by pressure solution, Yang (2000) set the grain boundary diffusion coefficient, D_{gb}, as in the above, to be a function of temperature (following an Arrhenius dependence):

$$D_{gb}(T) = D \exp\left(-\frac{E_a}{RT}\right), \tag{1.2.15}$$

where E_a is the effective activation energy, taken to be approximately 0.65 $\mathrm{kcal\,mol^{-1}}$ for quartz-water systems, and D is some constant. Viscosity was assumed to be independent of temperature in Yang's model. This resulted in an additional dimensionless parameter, β, which characterises the effect of a temperature gradient on the porosity and pressure, and is defined by

$$\beta = \frac{\gamma d}{T_0}. \tag{1.2.16}$$

Here, γ is the thermal gradient, d is a typical length-scale, and T_0 is the surface temperature used for scaling. From this, Yang (2000) concluded that in the more interesting case of fast compaction (corresponding to $\lambda \gg 1$), a larger thermal gradient resulted in a slightly larger reduction in porosity. This change was small, relative to the difference in orders of magnitudes of the thermal gradient considered. Qualitatively,

the influence of a thermal gradient was not significant, and the porosity profile did not differ largely from the equilibrium state explicitly found in Yang (1999). Hence, Yang (2000) concluded that temperature effects are only of secondary importance, in agreement with the more qualitative and numerical speculations by Angevine and Turcotte (1983).

Although not directly linked to compaction, the analysis of pressure solution mechanisms in terms of creep laws (e.g., Shimizu (1995)) and reaction rates may be of interest a priori to porosity analysis. A general discussion of this geological process, including its various effects on different rocks, and its relation to time, mineralogy, and solution chemistry, can be found in Tada and Siever (1989).

1.2.3 Other compaction models

Chemical diagenesis includes any process with which the porous matrix is deformed via geochemical reactions. Much of the literature concentrates on mineral reactions such as dissolution and dehydration, which act to increase the porosity. Other mechanisms including precipitation and cementation may in turn decrease the porosity, thereby altering the pressure profile in a sedimentary layer. Diagenetic processes, cementation, and aquathermal pressuring have been explored as the main compacting mechanisms by many authors (Yang, 1997; Domenico and Palciauskas, 1979; Wangen, 1998; Bjørlykke and Egeberg, 1993; Walderhaug, 1996).

It is widely debated whether chemical diagenesis is a large contributing factor to porosity changes and generation of excess pressures. Osborne and Swarbrick (1997) presented a thorough review of the mechanisms for existence of overpressure in sedimentary basins, in which they concluded that diagenesis with or without hydration is of secondary importance. They stated that 'based on the available data, there is no strong evidence that diagenesis is a direct cause of overpressuring or underpressuring'. In fact, they said that the development of overpressure in low-permeability shales may act to inhibit dehydration in some minerals. However, it is agreed that diagenesis may have more significance in altering pressure profiles in the case of a closed system, such as in the presence of almost impermeable seals and other structural barriers affecting fluid flow. Further, some claim that these chemical compaction processes are only significant at temperatures above 70 degrees Celsius (Bjørlykke and Egeberg, 1993).

There is not much literature considering both mechanical and chemical compaction in the same model, with most work usually neglecting chemical compaction. Schneider et al. (1996) considered both mechanisms for compaction, but their work focused on the calibration of the coefficients encountered in their model (the rock viscosity in

particular, where the rock is modelled as a viscous fluid), rather than solving the model given empirical data.

1.2.4 Modelling of geological phenomena

A few, but not many, two-dimensional studies have been carried out for mechanical compaction (Bitzer, 1999; Wangen, 2001). The scarcity of two- or three-dimensional models can be explained by authors assuming that compaction is primarily a vertical process. However, we believe that in the presence of more realistic geological phenomena, two or three dimensions are essential to capture more accurate information in realistic basin models. Of the existing multi-dimensional models, these are usually examined only numerically and lack a solid mathematical foundation, or authors eventually simplify to the one-dimensional model when it comes to solving the model (for example, Fowler and Yang (1999) and Wangen (2001)).

Modelling the onset of structural phenomena such as sills and faults is difficult, but necessary. Faults occur usually at an angle, and therefore require considerations in two-dimensions at least, since they will affect the direction of flow. Whilst magmatic intrusions may not have a significant direct effect on the pressure profile for a sedimentary unit, sills or dykes (vertical magmatic intrusions) will affect the temperature profile, and their presence will act as a significant heat source within the basin. In the case of a dyke, the heat dissipation will take place laterally, and the second dimension becomes crucial. As a result, in order to properly account for such structures, we need to model the pressure and temperature profiles in both vertical and horizontal directions.

The current literature mostly uses an *a posteriori* inclusion of the above mentioned structures into fixed basin geometries, rather than allowing the structures to evolve naturally in the models. Some descriptions of the criteria for inducing a fault from overpressured fracturing based on maximum displacement of 'compartments' have been proposed (King Hubbert and Rubey, 1959), and Mann and Mackenzie (1989) also suggest dividing fault compartments into multiple 'cells', where the fluid flow is considered vertically only in each cell, in order to determine the overpressure profiles in faulted layers. However, theoretical studies or mathematical formulations of basin scale structures are scarce.

In addition to compartmentalisation, there have been some case studies and numerical simulations on lateral flows and the effect of seals on overpressure (e.g. Mann and Mackenzie (1989) and Hunt (1990)), and often faults have been modelled analogously to seals or compartment boundaries which trap fluid (Wangen, 2001).

Such faults are referred to as sealing or closed faults. However, fluid flow is thought to follow fault lines (open or non-sealing faults) which, in fact, act as paths that guide the flow (Hantschel and Kauerauf, 2009), rather than mimic the effect within seals where flow is hindered.

The only model we have encountered for compaction which incorporates fault lines as paths that permit flow is by Wangen (2002). Wangen defined the fluid rate Q_f between two fault compartments, assumed to be driven by the excess pressure difference, $p_1 - p_2$, by

$$Q_f = \frac{A_f k}{\mu z_f}(p_1 - p_2), \tag{1.2.17}$$

where A_f is the cross-sectional area of the fault zone with offset depth z_f. Wangen proceeded to simulate a two-dimensional model with the fault line, but it is unclear what exactly is being solved, and a complete two-dimensional mathematical model for the pressure found in the basin is not provided.

A very small amount of literature (e.g. Kjeldstad et al. (2003)) exists on the mathematical and numerical modelling of sills or dykes, with most presenting simulations of basins in place of specific solution methods applied to a concrete mathematical model. In particular, we have yet to find any literature theorising the effects of such structures on the co-dependent pressure, porosity, and temperature profiles within a basin, as a complete system that is able to describe the important fundamental geological processes at once.

1.2.5 Complete pressure-temperature models

The fluid pressure, porosity, and temperature are amongst the more important unknowns in the evolution of sedimentary basins in BPSM. In reality, each of these variables depends on each other, and we believe that these cannot be uncoupled into separate models, or only appear as known values within material constitutive equations. Those that include temperature considerations in the pressure model, for example Wangen (2001), do not model temperature from first principles of energy conservation, with the temperature instead included as a parameter for solving the pressure and porosity. Most other existing work in literature decouples the temperature in particular, and thermal considerations are generally considered alone (Speece et al., 1985; Wangen, 1992).

In addition to the fluid properties, porosity, and temperature, we believe that understanding the sediment properties is also important. In most literature, the rock pressures or velocities are not solved for. The latter is particularly important

for understanding the deformation of the basin over time. We have only seen rock properties in the capacity of a boundary condition, where the top boundary moves with respect to the sedimentation rate and the rock velocity, and the rock velocity in this case is usually substituted for the effective stress at the top boundary (e.g., Fowler and Yang (1999)). However, the internal deformation of the rock is incredibly important, especially when two-dimensional effects come into place, and therefore we believe that being able to model the rock properties is crucial to understanding compaction of basins.

1.3 Existing work and interests of our industrial partner

The data we use throughout this thesis is provided by our industrial partner, Petrotechnical Data Systems (PDS). Further to the existing modelling work outlined in the previous section, we summarise some of the existing numerical developments that have been made within PDS (Senior et al., 2016).

The numerical simulations modelling compaction by PDS assume that compaction is a purely vertical process, and assume that the porosity is only dependent on the depth as given by the simplest form of Athy's law (1.2.1). The 2D simulations they have are produced by dividing the domain into strips and solving a simple set of vertical equations in each strip, rather than from a complete two-dimensional model. The strips are then put together to create a 2D simulation. PDS understand that in reality, this is a significant simplification, and are particularly interested in being able to model a compacting basin in multiple dimensions.

The pore pressure and the temperature are not coupled in the model currently used by PDS, with the assumption being that they are not largely interrelated, and as such they are treated separately rather than concurrently in their simulations. This simplification is made in order to maximise computational efficiency, but PDS believe that they should be coupled in reality. Hence, testing whether they should indeed be coupled, and simply being able to couple all the variables is a feature which is of interest to PDS. Further, no rock variables are solved for and the rock viscosity where applicable is assumed to be constant. If the rock variables were to be known, this would provide PDS with more accurate information on the fluid profiles as well as the constitutive equations that depend on the rock properties. Though the solutions for the rock pressure and velocity on their own are not directly informative for industrial

purposes, PDS would like to be able to use their profiles to better estimate material parameters.

The modelling of external phenomena in basins is of utmost importance to PDS, given their ubiquity and complexity in the real geological world. Currently, faults are not modelled in the equations used by PDS, with PDS instead including their presence by a brute force method and by manipulating the geometry of the basin manually. If possible, PDS would like to model these structures in a general form via a more theoretical method. Sills are modelled by the source term in the temperature equation but recall that PDS currently solve for the temperature separately from the pressure, and therefore, the effects of the sill on the basin are not properly documented. PDS are interested to see whether the sill would indeed impact the pore pressures and the porosity within the basin.

In general, the models currently in use by PDS are disjointed, required to be solved separately, and are not easy to modify in such a way that they unify multiple phenomena into a single, comprehensive model. Hence, PDS are interested in having one complete model within which many different geological features can be included at once. Ideally, the complete model needs to be easily modified to account for or remove certain features depending on the geological era or situation.

1.4 Aims of thesis

We collaborate with our industrial partner, Petrotechnical Data Systems (PDS), to derive a more complete model and a respective computational solver that is able to more accurately determine the evolution of a sedimentary basin and that can improve on the existing work discussed in Sections 1.2 and 1.3. Therefore, in this thesis, we address some of the downfalls of existing models, and explore new ways to incorporate more realistic geological phenomena into compaction models. Further, we show that our new model and solver provide results that are in line with existing geological research and intuition, and provide insight into the mechanisms which affect compaction behaviour. In this way, we challenge some of the assumptions widely used in literature and in industry (as reported by our industrial partner), so that we have a better understanding of the phenomena which others could include for more accurate results. We outline our new ideas here in this section.

1.4.1 Multi-dimensional coupled model

We have already discussed the importance of knowing the pressure, porosity, and temperature profiles within sedimentary basins. The main motivations for these are to understand the more expansive locations for hydrocarbon potential and to use the properties within a basin to determine more efficient and safe recovery techniques of oil that is difficult to extract (due to reservoir location or geometry, for example), or particularly viscous.

Many models concentrate solely on the fluid pressure build up inside the basin and decouple the temperature, thus removing any thermal relationship to the pressure and compaction processes in the basin. This is due to many authors claiming that the temperature is not a significant factor in the compaction process, as also assumed by PDS in their existing models. Some researchers use thermal material properties, such as specific heat capacities and temperature as part of the viscosity, to model the overpressure, but in these cases the temperature is not solved simultaneously with the overpressure. Motivated in part by such omissions, in this thesis we derive a complete coupled model that involves all the variables at once.

Further, the rock behaviour is not usually incorporated into the model. We believe that the sediments which surround the trapped fluid would have a direct impact on the compaction process. Recall that our industrial collaborators also neglect the simulation of any rock behaviour, but they are interested in being able to incorporate them into future simulations. Hence, we develop a model which can incorporate the movement of rock as well as the fluid. For the rock, we do this by assuming the sediments behave like a highly viscous fluid and derive conservation laws from first principles. We make this assumption by noting that sediment movement is similar to creep and that the bulk of sediments will undergo shearing motion continuously and indefinitely. We also derive conservation laws from first principles for the fluid. These depend on the porosity and temperature, which we model separately. We model the temperature using the conservation of energy law from first principles. Note that additionally, we are able to model the domain deformation due to sedimentation and compaction, in a manner where one or the other can be neglected (usually sedimentation, since deposition does not always occur continuously over time unlike compaction).

Regarding the porosity, we incorporate both mechanical and chemical compaction in such a way that we may separate the influence of one from another. In this way, we can 'switch off' one of the mechanisms if necessary. The development of our more complex compaction model is motivated by the suggestions from other authors that the mechanisms take place at different locations within the basin, and hence we derive

the porosity in such a way that this is able to be accommodated if the user wishes. Further, we model compaction by relating the porosity with the rock properties we find (which other authors do not explicitly consider in their models), and derive a new model in terms of the pressures instead of the vertical effective stress. This, in turn, also means that two- or three-dimensional behaviour can be incorporated more accurately, since the vertical effective stress by definition only involves the vertical depth or height, and not the position along the width of the basin.

Indeed, recall that in most literature and in existing simulations used by PDS, authors also simplify their models into the one-dimensional model, even if initially derived to accommodate two or more dimensions. This is motivated by compaction being a mostly vertical process, and therefore, a multi-dimensional model is often solved by dividing the domain in vertical strips. However, it is clear from looking at physical basins present around Earth that most basins undergo some lateral behavioural changes, and hence the simplified one-dimensional models do not take into account the complex geological features that take place in realistic situations. The omission of such features or using a one-dimensional model may result in the neglect of significant lateral behaviour. Alternatively, one may need to divide the domain into a significantly increased number of vertical strips, thereby affecting computational efficiency. Hence, PDS are interested in being able to model the lateral variations within a basin properly using a full multi-dimensional model and respective solver without the need to use vertical strips. Hence we derive a multi-dimensional model where the fluid and rock pressures and velocities, the porosity, and temperature are fully coupled and interrelated.

Further, we derive the model in such a way that it is easy to incorporate complex geological features, such as deformation of the basin due to compaction or sedimentation, varying external stresses, source terms, and more, since we formulate the model in such a way where specific terms can be switched on or off, as desired. Having derived this complete model, we build a robust solver to solve our model, which can act as a base simulator on which we may add more complex geological features. Of course, we must verify that the solver behaves correctly, and we use existing numerical techniques to do so.

Deriving the model and its subsequent solver in this manner allows us to model multiple geological scenarios without changing the foundation of the model or solver. Such efficient manipulation of the model is of great importance in industry, since it allows one to avoid having to use entirely separate models for each situation.

1.4.2 Behaviour of a more complete model

After deriving the model and its solver, we study the behaviour of the pressures, velocities, porosity, and temperature within the basin. Recalling that our model now incorporates the rock properties and that we couple the temperature, we provide a comprehensive review of the basin evolution under different assumptions and varying parameters on geological timescales. This is also to check that our model and solver produce results that are physically intuitive and in line with those previously obtained by PDS and in the literature.

We first study the way in which sedimentation and manipulation of our domain with respect to compaction can be carried out in our simulations (in two and three dimensions). We are able to model the domain deformation due to sedimentation and compaction separately, so that the user again has the option to incorporate just one of the two processes in simulations, as needed.

1.4.2.1 Effect of permeability on compaction

In previous calculations and reviews of the compaction process, we often encounter the effects of different permeability on porosity reduction (Fowler and Yang, 1998). We provide simulations of compaction under multiple permeability values whilst also solving for the rock variables and temperature. We study the effects of various different permeability values as well as a varying permeability model. In industry simulations (as reported by PDS), permeability is often kept constant to maximise computational efficiency, and PDS are particularly interested to see the effects of different constant permeabilities and their comparison to a varying permeability model. Hence, we examine whether this is an appropriate simplification from our simulations.

1.4.2.2 A new model for porosity incorporating chemical compaction

As part of our model derivation, we derive the porosity model in such a way that the mechanical and chemical compaction components can be decoupled, as needed. In previous models and in that used by PDS, we have seen that these mechanisms are largely simplified and cannot be 'switched off' from the resulting equations in the models. By deriving the porosity model in this way, we can directly compare each of the processes in our model, and consider multiple geophysical situations by simply adding or removing terms in our model. Whilst in most of our simulations we incorporate both mechanisms into our model, we present the separate contributions of each individually in the compaction process. PDS still uses the simplest form of

Athy's law to model the porosity, and is greatly interested in a more complex porosity model, motivating the development of our new model. Further, PDS are unsure of whether chemical compaction is a significant factor in the burial process, and indeed, they report that this is a general question posed within industry. Hence, we address this issue, as well.

1.4.2.3 Viscosity effects on the complete model

As we model the rock pressure and velocity in addition to fluid behaviour by assuming that the rock behaves like a highly viscous fluid, we find that we must include the rock viscosity as a parameter in our model. In reality, the exact value of the rock viscosity is difficult to determine, but we expect the viscosity to vary in magnitude as the sediments slowly lithify into solid rock with time. Whilst we do not model the lithification process (where sediments solidify into rock), we examine the viscosity effect on the rock flow to present the importance of a varying rock viscosity. Recall that PDS consider the rock viscosity to be constant in their simulations, but are interested to see how it may affect the compaction behaviour, especially since this may be a method to mimic the lithification process.

1.4.3 Modelling of faults and other geological features

After we derive the model and discuss the findings of different internal geological phenomena, we outline the methods with which we incorporate external geological features into the basin and examine their effects. Modelling of geological phenomena is difficult but hugely important in determining the evolution of basins over geological timescales. PDS (and reportedly other companies in the BPSM industry) currently only have basic methods with which to model such phenomena, and they are seeking new and improved methods. The ideas outlined here give PDS new suggestions on incorporating such phenomena.

1.4.3.1 Lateral stresses in the basin

We present simulations in which compaction and flow behaviour are no longer completely vertical, an assumption often made in literature and also in industry. Having derived our model in two dimensions, we show that just a small change in the geological conditions of the basin can affect the compaction behaviour of the basin, as well as the pressure and velocity profiles of the fluid and the rock. The purpose of this is to show that it is crucial to allow for lateral variations when attempting to

simulate the compaction process, and to show that our model and solver can tackle such two- or three-dimensional behaviour (which the current PDS solver cannot). As previously discussed, PDS are interested in a solver which does not require the division of the basin domain into vertical strips, on which a one-dimensional model is solved. We show that the lateral variations in our solutions are significant enough that a two-dimensional solver is preferred in order to maintain computational efficiency when compared to using the vertical strip method.

1.4.3.2 Faults

Faults are modelled into our system via a changing permeability model rather than by brute force as used by PDS and also in the literature (where the fault lines are built directly into the geometry). In our case, we assume that the fault line acts to allow for easy fluid flow and examine the behaviour in the surrounding sediments under its presence. Since faults are very rarely vertical, we examine a case where the fault is diagonal, highlighting the need for a two-dimensional model. Fault lines can be seen in many real basins and therefore we believe that it is important to understand their effects on basin evolution. Our modelling approach provides a sensible way to incorporate realistic faults into simulations.

1.4.3.3 Sills

Our model also allows for a sill intrusion into a basin by employing a source term in our temperature equation, and we examine the effects of the resulting large heat flux. Sills, like faults, are ubiquitous in sedimentary basins, and therefore we believe this generalisation of the model is of practical interest.

1.5 Structure of thesis

Having discussed the aims and motivations behind the work in this thesis, we outline the structure of the remainder of the thesis.

In Chapter 2, we present our model. We derive each of our equations modelling the rock pressure and velocity, fluid pressure and velocity, porosity, and temperature from first principles with reasonable assumptions. We define the initial and boundary conditions that accompany each set of equations to complete the system. The constitutive relationships we use in our model are reviewed and defined. The system of equations with appropriate initial and boundary conditions is nondimensionalised, and the dimensionless parameters are identified. This chapter forms the foundation of the

derivation of our complete, multi-dimensional coupled model (which is an improvement to that currently used by PDS).

Chapter 3 is concerned with the development of the numerical solver for our base model. We outline the solution method, where we divide our full model into subsystems before solving. We derive the subsystem equations and define appropriate initial and boundary conditions. Any numerical tools we use are introduced and discussed. In order to determine the validity of the solver, we use the method of manufactured solutions on a simplified set of subsystems. Each subsystem is tested separately at this stage. We present the error analysis for the numerical solutions obtained for each variable. The methods with which we numerically incorporate the sedimentation and compaction processes are discussed. This chapter forms the foundation of the development of our base solver and will show that our solver is valid for use by our industrial collaborator.

In Chapter 4, we present simulation results for various internal properties and constitutive equations. We summarise the results to our base model in two or three dimensions (both with and without sedimentation), and discuss whether the solutions obtained for all our variables are as expected. The effects of varying and constant permeability models are tested, and the behaviour of the basin is discussed when different values of permeabilities are used. We present the results for our new porosity model, which is more complex than that used by PDS or in other literature, and compare the different mechanisms involved in the compaction process. Further, we compare the results for the basin properties when different viscosities are used.

In Chapter 5, we present simulations which include complex geological features. We show that altering the boundary conditions slightly to include a small lateral dependence can lead to drastically different simulations, namely the onset of lateral behaviour. The modelling of faults is discussed, and we produce simulations of the pressures, velocities, porosity, and temperature within a basin in the presence of a fault line. Finally, we simulate a sill intrusion into a basin, and examine the effects of the sill's induced heat flux on the basin evolution. We compare these results to those obtained when a sill is not introduced.

In Chapter 6, we summarise the findings in each chapter, discuss key findings of relevance to our industrial partner, and also discuss limitations of our model. We discuss further improvements that can be made to the solver, and present possible directions for future work.

Chapter 2

A mathematical model for a compacting basin

In this chapter, we derive a mathematical model to describe the multi-dimensional flow of the solid and fluid phases in a matrix comprising sediments and pore fluid, subject to both mechanical and chemical compaction. This model includes specific physical properties within the sedimentary layer, such as the pore pressure and temperature, throughout their development over geological timescales. We assume that loading (a mechanical process) and pressure solution (a chemical process) are the main driving components for compaction, and do not consider pore pressure development via more minor phenomena such as aquathermal pressuring (Luo and Vasseur, 1992; Wangen, 2001). Crustal thinning and mantle dynamics are ignored in this present model, and hence we will assume that the domain is fixed laterally throughout the thesis.

The current model used by Petrotechnical Data Systems (PDS), with whom we collaborate, does not take into account any lateral behaviour (especially regarding stresses) within the basin, and does not use a set of equations for the rock velocity or pressure that is derived by appealing to conservation of momentum. PDS believe that information is lost due to the simplification into a single dimension, and, as mentioned in Chapter 1, this is what is mostly done in industry and in the literature (for example, by Smith (1971), Yang (1997), Audet (1995)). Our model, which throughout the thesis is mostly presented in two spatial dimensions, can also easily be extended to support a third spatial dimension. Further, this support of multiple dimensions can also be easily incorporated in the numerical solver, as to be discussed in Chapter 3 with some three-dimensional results presented in Chapter 4. Most models do not couple all the major mechanisms together (such that the fluid and rock pressures are coupled with the temperature), and instead consider them separately (for example,

see those considered by Swarbrick et al. (2002), Wangen (2001)). We allow our system of equations to be coupled in all of our unknown variables.

We also propose a new compaction model to more realistically model a compacting basin. This new compaction model takes into account both the mechanical and chemical compaction in a single equation. The system of equations is written in a way to allow for the inclusion of source terms which can model further geological processes, like crystallisation and aquathermal pressuring, the precise modelling of which we currently neglect. It also allows for the input of different rock rheologies and properties without changing the structure of the equations. In summary, we derive a general model which takes into account all the major compacting mechanisms in a fully coupled system, and which is able to be extended to incorporate numerous geological features and support different rock properties without changing the structure of the system of equations.

This chapter is then structured as follows. We introduce our physical assumptions and domain setup. We then define our system of equations and discuss the boundary and initial conditions, before we derive them from first principles. The physical properties and their constitutive equations used in our model are defined. Lastly, we nondimensionalise our model and present the dimensionless parameters that appear in our model.

2.1 Assumptions and domain setup

For the domain setup, we refer the reader to Figure 2.1. The domain sides correspond to $x = -X, X$. We measure height in the z-direction from the bottom of the basement layer (where $z = 0$), with z pointing upwards. We refer to the region where $\{-X \leq x \leq X, h_0(x,t) \leq z \leq h_N(x,t)\}$ as the basin. Note that this domain can easily be extended to accommodate a three-dimensional model if necessary.

We assume that the basin initially consists of a layer of sediments, where the sides of the basin are impermeable to both solid and fluid phases. This layer is initially at rest at some known pressure. The basin sits on some incompressible, impermeable, fluid-like basement layer, which represents the lower lithosphere and other underlying layers. Recall that effects of tectonism and other basement dynamics are neglected. A known amount of water rests on the top of the basin, and we assume that the top of this water layer corresponds to $z = h_w$. This top boundary of the water layer and the bottom of the basement layer below the basin are assumed to be horizontal for all time. With these assumptions, the top of the sedimentary layer which rests

below the water layer is denoted by $z = h_N(x,t)$, and is dependent on v_{rz}, the vertical component of the velocity of the rock at the boundary, and the sedimentation rate, H. The interface between the bottom of the sedimentary layer and the basement layer is denoted by $z = h_0(x,t)$. For simplicity, we assume that the bottom of the sedimentary layer $z = h_0(x,t)$ is also fixed and horizontal for all time.

The pores in the deposited rock are assumed to be inter-connected and filled with fluid so that there is no empty space, and we assume that the sediments are deposited in such a way that they are fully saturated with fluid. Note that we consider the rock (bulk of sediments) to behave like a highly viscous fluid, made up of homogeneous isotropic material for each rock type. Furthermore, the temperature is assumed to be the same in each phase.

We assume that compaction is an irreversible process, and thus the basin cannot de-compact. The fluid pressure in the pores is assumed to always be larger than the hydrostatic pressure, so that overpressure is also a positive value. We also assume that the pore pressure cannot reach a value larger than the geostatic pressure (which is the pressure induced by overburden weight). Lastly, we assume that at the early stages of compaction, the rate of change of the difference between rock and fluid pressures is negligible. This comes into importance later in our numerical implementation.

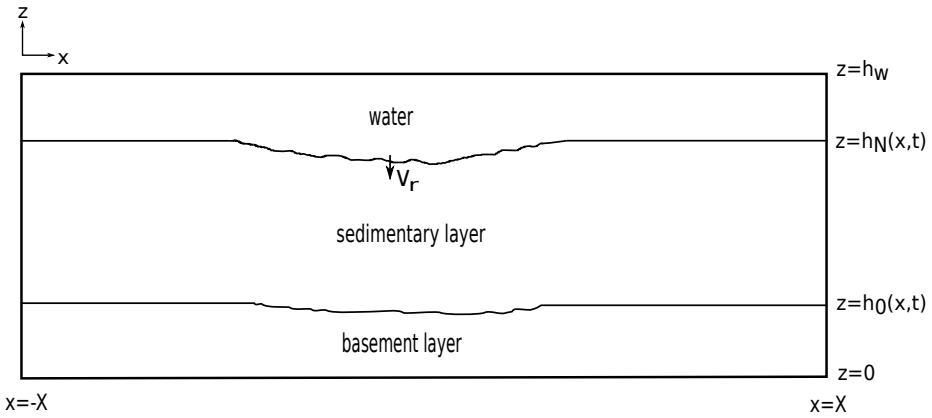


Figure 2.1: A cross-sectional schematic of our basin. The sedimentary layer comprises a single type of rock (lithology), and the rock properties depend on this rock type.

2.2 A model for a compacting basin

We introduce our dependent variables first. The porosity, ϕ, is defined to be the volume fraction of the fluid in the pores of the domain. Recalling that we are modelling the rock as a viscous fluid, we then denote the rock 'pressure' by p_r. Similarly, the

pore fluid pressure is denoted by p_f. The fluid and rock move with velocities $\boldsymbol{v_f}$ and $\boldsymbol{v_r}$, respectively. Finally, the temperature of the system is denoted by T. These unknowns are accompanied by physical parameters and constitutive relationships for the fluid and the rock, and these are described later in the section. This system then consists of six nonlinear equations which govern the pressures (p_f, p_r), velocities $(\boldsymbol{v_r}, \boldsymbol{v_f})$, temperature (T), and porosity (ϕ) in the basin, with appropriate boundary and initial conditions.

These six equations in our system describe the evolution of volume fraction, pressures, velocities, and temperature within the basin. We require conservation of mass of both the rock and fluid phases in our system. Additionally, momentum of both phases must be conserved. In this case, the fluid is governed by a Darcy-type law, and the rock is governed by a Stokes-type system for a highly viscous slow flow. Porosity variations within the basin are dependent on the pressure difference between the two phases. Finally, we state that the heat energy within the system is conserved. We derive these equations in the following subsections.

2.2.1 Model derivation

The individual governing equations are derived from first principles. We use the conservation of mass and momentum laws to describe fluid and rock motion, and conservation of energy arguments to define the temperature profile. The compaction equation is original, and is derived from two existing models that govern mechanical and chemical compaction, respectively.

2.2.1.1 Conservation of mass

The equations for conservation of mass for the rock and fluid can be derived following standard techniques from first principles (Gonzalez and Stuart, 2008). The rate of change of mass of rock and fluid in an arbitrary volume of the volume fraction in the basin must take into account the net mass of the phase in consideration that enters the volume. Additionally, we must include any rock formed from the pore fluid precipitating. The rate at which mass of rock is introduced into the system (which is represented by S_r) is related to the rate of mass of pore fluid lost in the reaction (denoted by S_f). Then, the equations for conservation of mass for the rock and fluid,

respectively, are given by

$$\frac{\partial}{\partial t}((1-\phi)\rho_r) = -\nabla \cdot ((1-\phi)\rho_r \boldsymbol{v}_r) + S_r, \tag{2.2.1}$$

$$\frac{\partial}{\partial t}(\phi\rho_f) = -\nabla \cdot (\phi\rho_f \boldsymbol{v}_f) + S_f, \tag{2.2.2}$$

where ρ_r and ρ_f are the rock and fluid densities, respectively.

2.2.1.2 Conservation of momentum

We derive the equations for the conversation of momentum in both phases for a general case, following ideas from McKenzie (1984). The Reynolds number for the system is small at around $\mathcal{O}(10^{-22})$ (calculated from data provided by Senior et al. (2016)), and this allows us to neglect inertial terms. Note that we neglect tectonic stresses in our current model and therefore there are no external shear stresses on our system.

In general, for a force balance and neglecting inertial terms, the total momentum conservation equation for the fluid phase (in index notation) can be written as (Drew and Segel, 1971)

$$-\phi\rho_f g\delta_{i2} - A_i + \frac{\partial}{\partial x_j}(\phi\sigma^f_{ij}) = 0. \tag{2.2.3}$$

Here, δ_{ij} is the usual Kronecker delta, where the second component of each vector denotes the vertical component (noting that in 3D, we use the third component for the vertical component). The vector $\boldsymbol{A}$ is the interphase force and σ^f_{ij} is the fluid's total stress tensor, where the superscript f once again denotes that it is a property for the fluid.

The first term on the left hand side is representative of the body forces acting on the system, and in this case is simply the gravitational force. The term A_i is the interphase force, or the force exerted by the fluid phase onto the rock. We define this interphase force to be (McKenzie, 1984)

$$\boldsymbol{A} = D(\boldsymbol{v}_f - \boldsymbol{v}_r) - p_f\nabla\phi, \tag{2.2.4}$$

where D is a drag coefficient due to viscosity. The second term on the right hand side of the equation (2.2.4) is the 'static drag force' or the interphasial pressure contribution to the drag force, which is the force exerted by the fluid onto the rock matrix (Drew and Segel, 1971). If the porosity is constant, the static drag force would simply be equal to p_f, but here, we must take into account the porosity gradient. Morency and Tromp (2008) provide a detailed derivation and discussion of this static drag force.

Now let us consider the last term on the left hand side of (2.2.3), which is the total stress tensor for the fluid. This stress tensor for the fluid takes the simple form of

$$\sigma_{ij}^f = -p_f \delta_{ij}, \tag{2.2.5}$$

where we have assumed that the pore fluid is inviscid at the microscopic scale.

Substituting these definitions into (2.2.3), we have that

$$-\phi\rho_f g\delta_{i2} - D(v_{f_i} - v_{ri}) + p_f \frac{\partial \phi}{\partial x_i} + \frac{\partial}{\partial x_j}(\phi\sigma_{ij}^f) = 0, \tag{2.2.6}$$

where g is the gravitational acceleration constant. Expanding the derivative in the last term on the left hand side, and choosing D in such a way that it recovers Darcy's law (similar to McKenzie (1984)), with $D = \frac{\mu_f \phi^2}{k}$ where μ_f is the fluid viscosity and k denotes the permeability, we find the fluid momentum conservation equation to be

$$\boldsymbol{v}_f - \boldsymbol{v}_r = -\frac{k}{\mu_f \phi}(\nabla p_f + \rho_f \boldsymbol{g}), \tag{2.2.7}$$

with

$$\boldsymbol{g} = \begin{pmatrix} 0 \\ g \end{pmatrix}, \tag{2.2.8}$$

where g is the acceleration due to gravity. Note that with this choice of D, if the rock matrix is stationary, we have that

$$\boldsymbol{v}_f = -\frac{k}{\phi\mu_f}(\nabla p_f + \rho_f \boldsymbol{g}), \tag{2.2.9}$$

indeed recovering Darcy's law.

We can write the momentum conservation equation for the solid or rock phase in a similar fashion. For the rock, the general momentum conservation is given by

$$-(1-\phi)\rho_r g\delta_{i2} + A_i + \frac{\partial}{\partial x_j}((1-\phi)\sigma_{ij}^r) = 0. \tag{2.2.10}$$

Note that the interphase force is equal and opposite, and therefore it differs only by a sign difference between the fluid and solid phases. The total stress tensor σ_{ij}^r here is for the rock.

Modelling the rock as a highly viscous fluid subject to infinitesimally small deformations, we assume that the stress tensor for the solid phase can be written in the general form for a viscous compressible fluid, so that

$$\sigma_{ij}^r = -p_r \delta_{ij} + \tau_{ij}, \tag{2.2.11}$$

with τ_{ij} modelled as appropriate according to the rock rheology in consideration.

Hence, using (2.2.10), we have that

$$-(1-\phi)\rho_r g\delta_{i2} + \frac{\mu_f \phi^2}{k}(v_{f_i} - v_{ri}) - p_f \frac{\partial \phi}{\partial x_i} + \frac{\partial}{\partial x_j}((1-\phi)(-p_r\delta_{ij} + \tau_{ij})) = 0. \quad (2.2.12)$$

Substituting in the results from (2.2.7) and manipulating, we have that

$$-((1-\phi)\rho_r + \phi\rho_f)\boldsymbol{g} - \nabla((1-\phi)p_r + \phi p_f) + \nabla \cdot ((1-\phi)\underline{\underline{\boldsymbol{\tau}}}(\boldsymbol{v}_r)) = \mathbf{0}. \quad (2.2.13)$$

In summary, our conservation of momentum equations for the rock and fluid, respectively, are given as

$$\phi(\boldsymbol{v}_r - \boldsymbol{v}_f) = \frac{k}{\mu_f}(\nabla p_f + \rho_f \boldsymbol{g}), \quad (2.2.14)$$

$$-((1-\phi)\rho_r + \phi\rho_f)\boldsymbol{g} - \nabla((1-\phi)p_r + \phi p_f) + \nabla \cdot ((1-\phi)\underline{\underline{\boldsymbol{\tau}}}) = \mathbf{0}. \quad (2.2.15)$$

2.2.1.3 Compaction equation

Our compaction or porosity equation is based on the mechanical and chemical compaction laws by Athy (1930) and Schneider et al. (1996), respectively, and is given by

$$\frac{D\phi}{Dt} = -\phi_0 \chi \frac{D}{Dt}(p_r - p_f)\exp(-\chi(p_r - p_f)) - \frac{C(\phi)}{\mu_r}(p_r - p_f) + F, \quad (2.2.16)$$

where $\frac{D}{Dt}$ is the material derivative with respect to the rock movement, such that

$$\frac{D}{Dt} = \frac{\partial}{\partial t} + \boldsymbol{v}_r \cdot \nabla. \quad (2.2.17)$$

This equation (2.2.16) governs the porosity changes due to mechanical and chemical compaction. Any additional contributions, such as porosity changes arising from external forces (e.g. tectonic forces) or due to the presence of geological features, are represented by the function F. In (2.2.16), ϕ_0 denotes the surface or depositional porosity, μ_r is the rock viscosity, and χ is the mechanical compaction coefficient which is found empirically (Senior et al., 2016).

The first term on the right hand side of (2.2.16) is an Athy-type law, which represents the mechanical compaction of the sediments. Athy's law is an empirical law which states that the porosity decreases exponentially with depth in its original form (Athy, 1930), so that

$$\phi = \phi_0 \exp(-\chi z). \quad (2.2.18)$$

It has since been modified and improved by more accurately predicting that the porosity decreases exponentially with the difference between the pore pressure and overburden pressure (for example, by Smith (1971)). This overburden or lithostatic pressure (which we denote by p_L) is only dependent on the densities of the two phases and the porosity, and is usually given by

$$p_L = \int_0^h (1-\phi)\rho_r + \phi\rho_f \, dz, \tag{2.2.19}$$

where h is the height of the basin whose bottom boundary corresponds to $z = 0$, ϕ is the porosity, and ρ_r an ρ_f are the densities of the rock and fluid phases, respectively. In our model, we modify this slightly, and we propose that the porosity with respect to mechanical contributions only is related to the difference between the pressure felt by the rock and the pressure in the fluid, so that in the case of pure mechanical compaction,

$$\phi \sim \phi_0 \exp(-\chi(p_r - p_f)). \tag{2.2.20}$$

This modification follows from the theory that the pore fluid is subject to the forces applied by the rock locally as well as the wider surrounding forces. Since we model gravitational forces directly into our equation governing rock flow (2.2.1), the rock pressure (which we model as a viscous fluid) incorporates both the overburden loading as well as any other forces from the interphase interaction and viscous forces. Hence, allowing the porosity evolution to depend on p_r rather than p_L allows us to include the local changes in pressure as well as the overlying weight within the basin considered in earlier model. Hence, using (2.2.20), we deduce that the rate of change of the porosity due to mechanical processes can be modelled as

$$\frac{D\phi}{Dt} = -\phi_0\chi\frac{D}{Dt}(p_r - p_f)\exp(-\chi(p_r - p_f)). \tag{2.2.21}$$

The second term on the right hand side of (2.2.16) represents the change in porosity due to chemical compaction. The original expression for chemical compaction used by Schneider et al. (1996) is given by

$$\frac{D\phi}{Dt} = -\frac{(1-\phi)}{\mu_r}(p_L - p_f), \tag{2.2.22}$$

where the authors again use p_L instead of p_r. We note that for $\phi = 0$, we have that $\frac{D\phi}{Dt} \neq 0$. This means that when the basin is made up purely of rock, chemical compaction is still taking place, which is inconsistent. It is therefore unable to fully describe a compaction law for all values of ϕ. The authors, however, do set a minimum

porosity for chemical compaction, so that for any points within the basins with a porosity smaller than the minimum porosity, $\frac{D\phi}{Dt}$ is forced to equal zero.

Though it has its downfalls, the idea behind the law (2.2.22) being valid only down to a minimum porosity is physically valid, as we would expect that at very low porosities, there would not be enough pore fluid for chemical reactions with the rock to take place. Additionally, (2.2.22) corresponds to the behaviour that chemical compaction is most significant at smaller values of porosity, usually at depths below 2km (Swarbrick et al., 2002). Note that, physically, if the porosity is high, we expect pressure solution to be a small contribution since grain-to-grain contact within the sediments is small. The contribution increases with decreasing porosity, until it reaches some range where there is only little fluid for the sediments to dissolve in. We therefore assume that for values below some minimum porosity, the contribution from chemical compaction decays rapidly to zero, whilst also maintaining the idea that the chemical compaction contribution at higher porosities is small.

Hence, let us modify (2.2.22) so that

$$\frac{D\phi}{Dt} = -\frac{\tilde{C}\phi^m(1-\phi)^n}{\mu_r}(p_r - p_f), \tag{2.2.23}$$

where $\tilde{C}$ is some compaction coefficient. By adding the extra factor ϕ^m and raising $(1-\phi)^n$, we extend the existing Schneider et al. (1996) model by making it valid for all $\phi \in [0,1]$ to additionally state that no compaction can happen if there is no fluid in the system (when $\phi = 0$). Note that the factors $\tilde{C}, m$, and n are expected to vary for different lithologies, which we can approximate by fitting to existing data.

Further, similar to our variation of the mechanical compaction part, we also alter the Schneider et al. (1996) model so that the porosity change is a function of the difference between the rock and fluid pressures, rather than the effective stress. Since chemical compaction describes a more microscopic process than one that is larger-scale (like overburden weight), using $p_r - p_f$ as the argument for the chemical compaction term is a reasonable variation to existing models.

Then, combining the term modelling mechanical compaction and our modified chemical compaction law (and letting F denote contributions to compaction via other phenomena), our total compaction or porosity equation becomes

$$\frac{D\phi}{Dt} = -\phi_0\chi\frac{D}{Dt}(p_r - p_f)\exp(-\chi(p_r - p_f)) - \frac{C(\phi)}{\mu_r}(p_r - p_f) + F, \tag{2.2.24}$$

as in (2.2.16), where $C(\phi) = \tilde{C}\phi^m(1-\phi)^n$ is a constitutive relationship for the chemical compaction.

2.2.1.4 Conservation of heat energy

The averaged conservation of heat energy in the system can be derived easily from first principles again (Gonzalez and Stuart, 2008), and is given by

$$\frac{\partial}{\partial t}((\phi\rho_f c_f + (1-\phi)\rho_r c_r)T) + \nabla\cdot((\phi\rho_f c_f \boldsymbol{v}_f + (1-\phi)\rho_r c_r \boldsymbol{v}_r)T) = \nabla\cdot(\kappa_T \nabla T) + S_T. \tag{2.2.25}$$

Here, c_r and c_f denote the specific heat capacities of the rock and fluid, respectively, and κ_T is the phase-averaged thermal conductivity. The heat source term is denoted by S_T and represents additional heat into the system due to radiation. Note that this term can also be used to introduce geological features, such as sills and dykes, into our model if necessary.

2.2.2 Discussion of boundary and initial conditions

We require suitable initial and boundary conditions for a well-posed system and these are discussed briefly here. For the initial conditions at $t = 0$, recall that our basin has impermeable side boundaries, whilst both the top and bottom of the basin are free boundaries, whose initial positions ($h_{00}(x)$ and $h_{N0}(x)$, respectively) are known. A layer of sediments at surface porosity (ϕ_0) exists initially. We also assume that the temperature varies linearly with depth and equals $T_0 + \theta(h_{N0}(x) - z)$ in the existing sedimentary layer, where θ is some initial known temperature gradient with respect to depth.

To model the evolution of porosity with time, the advective equation (2.2.24) for the porosity variable requires an initial condition everywhere (which we just defined) and boundary conditions only on the inflow portion of the boundary of the domain, where $\boldsymbol{v}_r \cdot \boldsymbol{n} < 0$, with $\boldsymbol{v}_r$ denoting the advecting velocity (which is the rock velocity for our system) and $\boldsymbol{n}$ the outward pointing unit normal to the boundary. Since clearly the sides of the basin are not inflow boundaries, we will not need to define boundary conditions for the porosity on these boundaries. Hence, we assume that the top of the basin is the only inflow boundary, where $\phi = \phi_0$ (note that no rock is flowing out of the basin through the bottom boundary). To determine the temperature within the basin, we require additional conditions for the temperature or its flux at all boundaries. At the bottom boundary, there is a heat flux (q) from the basement layer (representing the heat flux from the mantle below), with the top boundary held at the reference temperature, T_0. The sides of the basin are assumed to be insulated and subject to no heat flux.

Let us consider the motion of the fluid and rock phases. The top basin boundary h_N must move with the rock, taking into account the extra deposition that has occurred (via the sedimentation rate, given by H). These constitute the conditions for the free boundary. For the rock, we impose no shear stresses on the top free boundary, so that the tangential components of the total normal stress on the top boundary are zero. The normal component of the total stress acting in the normal direction on the boundary would be simply the weight of the water layer lying above it at the top of the basin (given by $-(p_a + \rho_w g(h_w - h_N))$). Here, p_a is the atmospheric pressure, g is the gravitational constant, and ρ_w is the density of the water lying above the sedimentary layer.

For the bottom boundary, we have that $\boldsymbol{v}_r \cdot \boldsymbol{n} = 0$, which constrains the normal component of the rock velocity, and there are no shear stresses tangentially. Note that if we do not take the bottom boundary to be fixed and horizontal, but rather a free boundary like the top of the basin, the boundary condition would be similar to that of the top, where the normal component of the total stress acting in the normal direction would be the geostatic pressure measured from the bottom of the basement layer for the bottom of the basin (given by $-(p_B - \rho_B g h_0)$). Here, p_B is the known pressure at the bottom of the basement layer, and ρ_B is the density of the basement layer.

On the sides of the basin, there is no flux of fluid or the rock, which constrains the normal component of the velocities. Tangentially, we again impose no shear stresses on the sides of the basin, which provides the information about the remaining components of the velocities. Finally, the overpressure is zero at the top surface of the basin, so that the fluid pressure is equal to the rock pressure. The no-flux conditions for the sides then automatically constrain the normal derivative of pressure there, which we can simply deduce from our governing equations.

2.2.3 Summary of model

We now present our model in full. For convenience, we work with two dimensions only. However, the system can easily by extended to three dimensions, where the boundary conditions of the extra coordinate, 'y', would be identical to the 'x' conditions. To summarise, in the basin region defined by $\Omega = \{-X \leq x \leq X, h_0(x,t) \leq z \leq h_N(x,t)\}$,

we have that for $t > 0$,

$$\frac{\partial}{\partial t}((1-\phi)\rho_r) = -\nabla \cdot ((1-\phi)\rho_r \boldsymbol{v}_r) + S_r, \tag{2.2.26}$$

$$\frac{\partial}{\partial t}(\phi\rho_f) = -\nabla \cdot (\phi\rho_f \boldsymbol{v}_f) + S_f, \tag{2.2.27}$$

$$\phi(\boldsymbol{v}_r - \boldsymbol{v}_f) = \frac{k}{\mu_f}(\nabla p_f + \rho_f \boldsymbol{g}), \tag{2.2.28}$$

$$-((1-\phi)\rho_r + \phi\rho_f)\boldsymbol{g} - \nabla((1-\phi)p_r + \phi p_f) + \nabla \cdot ((1-\phi)\underline{\underline{\boldsymbol{\tau}}}) = \mathbf{0}, \tag{2.2.29}$$

$$\frac{D\phi}{Dt} = -\phi_0 \chi \frac{D}{Dt}(p_r - p_f)\exp(-\chi(p_r - p_f)) - \frac{C(\phi)}{\mu_r}(p_r - p_f) + F, \tag{2.2.30}$$

$$\frac{\partial}{\partial t}((\phi\rho_f c_f + (1-\phi)\rho_r c_r)T) + \nabla \cdot ((\phi\rho_f c_f \boldsymbol{v}_f + (1-\phi)\rho_r c_r \boldsymbol{v}_r)T) = \nabla \cdot (\kappa_T \nabla T) + S_T, \tag{2.2.31}$$

where the advective derivative is with respect to the rock velocity, such that $\frac{D}{Dt} = \frac{\partial}{\partial t} + \boldsymbol{v}_r \cdot \nabla$, and $\boldsymbol{g}$ denotes the gravitational acceleration vector. The first two equations (2.2.26, 2.2.27) in the system represent the conservation of mass for the rock and fluid phases, respectively. The Darcy-type law for fluid momentum is given by (2.2.28) and the rock momentum equation by (2.2.29). The compaction or porosity equation is given in (2.2.30), with the temperature equation given in (2.2.31).

The basin initially is made of up sediments at surface porosity and at a temperature that increases linearly with depth. We also know the depth and thickness of the initial basin. Then, the initial conditions for the system are: at $t = 0$, for all $(x, z) \in \Omega$,

$$\begin{aligned} \phi = \phi_0, \qquad & T = T_0 + \theta(h_{N0}(x) - z), \\ h_0(x, t=0) = h_{00}(x), \qquad & h_N(x, t=0) = h_{N0}(x), \end{aligned} \tag{2.2.32}$$

where the initial (known) positions of the bottom and top of the pre-existing sedimentary layer are denoted by $h_{00}(x)$ and $h_{N0}(x)$, respectively. Additionally, θ represents the initial (known) temperature gradient with respect to depth.

For all $t > 0$, the top boundary of the basin moves with the rock velocity $\boldsymbol{v}_r$ at the boundary and takes into account the sedimentation rate, and the boundary conditions are given as follows. At $z = h_N(x, t)$ (at the interface between the fluid and sedimentary layer), we have that

$$\begin{aligned} \phi = \phi_0, \qquad T = T_0, \qquad \frac{Dh_N}{Dt} = v_{rz}|_{z=h_N} + H, \qquad p_r = p_f, \\ \boldsymbol{n} \cdot (-p_r \boldsymbol{I} + \underline{\underline{\boldsymbol{\tau}}})\boldsymbol{n} = -(p_a + \rho_w g(h_w - h_N)), \qquad \boldsymbol{n} \cdot (-p_r \boldsymbol{I} + \underline{\underline{\boldsymbol{\tau}}})\boldsymbol{t} = 0, \end{aligned} \tag{2.2.33}$$

where $\boldsymbol{n}$ is the outward pointing unit normal vector and $\boldsymbol{t}$ is any linear combination of two linearly independent tangential vectors that make up the tangent plane to

the interface given by $z = h_N(x,t)$. The term $-(p_a + \rho_w g(h_w - h_N))$ represents the pressure due to the overlying water weight, which acts in the inward normal direction to the surface.

For the bottom of the basin, where $z = h_0(x,t)$, assuming that the heat flux from the basement layer from the hotter mantle below, given by q, is known, we have

$$\kappa_T \nabla T \cdot \boldsymbol{n} = -q, \qquad \boldsymbol{v}_r \cdot \boldsymbol{n} = 0, \qquad \boldsymbol{n} \cdot (-p_r \boldsymbol{I} + \underline{\underline{\boldsymbol{\tau}}})\boldsymbol{t} = 0, \tag{2.2.34}$$

where $\boldsymbol{n}$ and $\boldsymbol{t}$ are now with respect to the bottom boundary of the basin.

Finally, on the sides where $x = -X$ or $x = X$, we have

$$\begin{aligned} \boldsymbol{v}_f \cdot \boldsymbol{n} &= 0, \qquad & \kappa_T \nabla T \cdot \boldsymbol{n} &= 0, \\ \boldsymbol{v}_r \cdot \boldsymbol{n} &= 0, \qquad & \boldsymbol{n} \cdot (-p_r \boldsymbol{I} + \underline{\underline{\boldsymbol{\tau}}})\boldsymbol{t} &= 0, \end{aligned} \tag{2.2.35}$$

where $\boldsymbol{n}$ and $\boldsymbol{t}$ are with respect to the sides of the basin. This completes our model.

2.3 Physical properties and constitutive equations

2.3.1 Summary of material properties

We now introduce and define the material properties that are relevant in our model. Each phase has a specific heat capacity, c, and density, ρ. Note that we use the subscript f to show that the parameter is representative of the fluid phase, whereas the subscript r is used for the rock phase. The fluid viscosity, μ_f, is assumed to be constant, whereas the rock viscosity, $\mu_r(T)$, is assumed to follow an Arrhenius-type law and thus to be dependent on the temperature. The permeability of the rock phase is given by $k(\phi)$ and the thermal conductivity, $\kappa_T(\phi)$, is a phase-averaged quantity so that the same value applies to both rock and fluid phases. The porosity with which sediments deposit is referred to as the surface or depositional porosity, and is denoted by ϕ_0. Mechanical and chemical compaction are controlled by the coefficient χ, and a constitutive relationship $C(\phi)$, respectively, which we obtain from empirical observations. All these parameters, except the permeability, rock viscosity, and thermal conductivity, are obtained by interpolating available data (Senior et al., 2016) and are not modelled separately here. For the permeability, rock viscosity, and thermal conductivity, we use appropriate constitutive models which we define shortly. Lastly, the deviatoric stress tensor for the rock is denoted by $\underline{\underline{\boldsymbol{\tau}}}(\boldsymbol{v_r})$ and is usually dependent on the gradients of the rock velocity, with its functional form varying for different rheologies.

In summary, constitutive relationships in our system are required for the rock viscosity, $\mu_r(T)$, rock permeability, $k(\phi)$, thermal conductivity, $\kappa_T(\phi)$, chemical compaction function, $C(\phi)$, and the deviatoric rock tensor, $\underline{\underline{\boldsymbol{\tau}}}(\boldsymbol{v_r})$, and these are defined in the next subsection. The specific heat capacities, $c_f(T), c_r(T)$, and densities, $\rho_f(T), \rho_r(T)$, are found from data. The constant parameters in our system are the fluid viscosity, μ_f, surface porosity, ϕ_0, and mechanical coefficient, χ.

Source terms via phenomena such as diagenesis (which was discussed in Chapter 1) are represented by a term S. The subscript r denotes a source term for rock mass, f for the fluid mass, and T for an additional heat source, due to radiation, for example. We write any contributions to porosity reduction via means other than mechanical and chemical actions through a term F.

2.3.2 Constitutive equations

2.3.2.1 Permeability model

We discuss some suitable permeability models which we may choose to employ in our compaction model. Existing permeability models are found empirically, and we assume that the models we present are good approximations to sediments at the basin scale.

The most widely used model is an empirical relationship based on the famous Kozeny-Carman permeability model (Costa, 2006), where the permeability, k, is given by

$$k(\phi) = C_{kc}\frac{\phi^a}{(1-\phi)^b}, \tag{2.3.1}$$

where C_{kc}, a and b are found empirically, and in general vary for different lithologies within the basin (Angevine and Turcotte, 1983). The constant C_{kc} is usually representative of the sediment properties (for example, hydraulic conductivity is used by Sharp (1976)).

Sharp and Domenico (1976) take $C_{kc} = \mathcal{O}(10^{-14})\text{m}^2$, $a = 3$ or 4 and $b = 2$ for some non-specific mudstones, whereas Smith (1971) uses $C_{kc} = \mathcal{O}(10^{-18})\text{m}^2$, $a = 8$ and $b = 0$, and Angevine and Turcotte (1983) use $C_{kc} = \mathcal{O}(10^{-13})\text{m}^2$, $a = 8$ and $b = 2$ to model shales. It is in fact suggested by Pape et al. (2000) that a takes a value between 1 and 10 for sediments occurring in geological reservoirs and basins. The choice of a again depends on the lithology of the sediments, with a lower value more appropriate for sandstones and a higher value suggested for shales (Pape et al., 2000).

Inverse solid fraction models are also commonly seen in literature, and are based on the above Kozeny-Carman models. For example, Yang (2000) modified the formula

to

$$k = \left(\frac{\phi}{\phi_0}\right)^8 \frac{1}{(1-\phi)^2}, \tag{2.3.2}$$

for basins with small porosities. Further, Bernaud et al. (2006) use

$$k = C_{kc}\left(\frac{\phi}{\phi_0}\right)^3 \left(\frac{1-\phi_0}{1-\phi}\right)^3 \tag{2.3.3}$$

for a Cam-Clay model, and Wangen (2000) suggests the form

$$k = C_{kc}\hat{k}\left(\frac{\phi - 0.05}{\phi_0 - 0.05}\right)^m, \qquad \hat{k} = \frac{(1+e)(1-\phi_0)}{(1+e_0)(1-\phi)}, \tag{2.3.4}$$

where e is the void ratio defined by $e = \frac{\phi}{1-\phi}$ and e_0 is a reference void ratio, with $m = 3$ for sandstones (and for extremely low porosities) and $m = 5$ for shales, following Ungerer et al. (1990). Note that in Wangen's model, $\hat{k} \approx 1$, but is still included in the definition of k 'to simplify the analytical treatment of the overpressure considerably'.

We finally present some other models which are observed in some of the more prominent basin modelling literature. Though Kozeny-Carman type permeability models are most frequently encountered, the exponential model is also used relatively often. This is given by Olsen (1960) as

$$k = \exp\left(\alpha(\phi^2 - \phi_0^2)\right), \tag{2.3.5}$$

where the parameter α indicates how quickly the permeability of clays decrease as the porosity is reduced. Audet and McConnell (1992) use this model stating that permeability for clays cannot be described sufficiently well via simple algebraic functions similar to the Kozeny-Carman model. They also mention that this exponential model, also proposed by Wangen (1992), allows the permeability to be non-zero even as the porosity tends to zero, which is more physically realistic in basins.

Finally, other models derived empirically include that used by Shi and Wang (1986), who related the permeability with the effective stress, σ (as used in other porosity models), rather than porosity, given by

$$k = k_0\left(\frac{\sigma}{p_{atm}}\right)^{-m}, \tag{2.3.6}$$

and a simple model used by Luo and Vasseur (1992), defined

$$k = 10^{-5}\phi^5, \tag{2.3.7}$$

which is then scaled further by $10^n, n = 1, 2, 3, 4$, to represent effects of increasing sealing by chemical diagenesis.

Note that it is easy to vary the permeability model in our system of equations depending on the rock type in consideration. In this thesis, we either consider k to be constant or for a varying permeability model for shale, we use

$$k(\phi) = k_0 \left(\frac{\phi}{\phi_0} \right)^8 . \tag{2.3.8}$$

This permeability model is discussed more in Chapter 4.

2.3.2.2 Rock viscosity model

Throughout this thesis, each rock viscosity is assumed to follow an Arrhenius-type model (Laidler, 1984), given by

$$\mu_r(T) = \mu_{r0} \exp\left(\frac{E}{R} \left(\frac{1}{T} - \frac{1}{T_0} \right) \right), \tag{2.3.9}$$

where μ_{r0} is some reference viscosity corresponding to a reference temperature, T_0, R is the universal gas constant, and E is the activation energy of the material, which is assumed to be constant and known for different lithologies.

2.3.2.3 Rock rheology models for deviatoric stress

Our model allows for a number of different rheologies and throughout this section we adapt the work by Gerya (2010). The deviatoric component of the stress tensor can be modelled appropriately to account for viscous, elastic, or plastic behaviour by using the deviatoric strain rate tensor for the rock, $\dot{\varepsilon}'_{ij}(\boldsymbol{v}_r)$, to define $\underline{\underline{\boldsymbol{\tau}}} = \underline{\underline{\boldsymbol{\tau}}}(\dot{\varepsilon}'_{ij})$. Let us define the components of the strain rate tensor, $\dot{\varepsilon}_{ij}$, as

$$\dot{\varepsilon}_{ij} = \frac{1}{2} \left(\frac{\partial v_{ri}}{\partial x_j} + \frac{\partial v_{rj}}{\partial x_i} \right). \tag{2.3.10}$$

Then the deviatoric strain rate tensor can be defined as

$$\dot{\varepsilon}'_{ij} = \dot{\varepsilon}_{ij} - \frac{1}{3} \dot{\varepsilon}_{kk} \delta_{ij}. \tag{2.3.11}$$

Using this definition, we may define the relationship between the deviatoric strain rate tensor and shear stress tensor for a number of cases.

For example, for viscoelastic behaviour, the deviatoric stress tensor may be defined to satisfy

$$\dot{\varepsilon}'_{ij_{(\text{viscoelastic})}} = \frac{1}{2\mu_r} \tau_{ij} + \frac{1}{2G} \frac{D\tau_{ij}}{Dt}, \tag{2.3.12}$$

where G is the shear modulus, and assuming no stress rotation. For rock that behaves only as a viscous fluid, we can define the shear stress tensor components as simply

$$\tau_{ij} = 2\mu_r \dot{\varepsilon}_{ij}. \tag{2.3.13}$$

For visco-elastic-plastic rheology, we may have

$$\dot{\varepsilon}'_{ij} = \dot{\varepsilon}'_{ij_{(\text{viscoelastic})}} + \dot{\varepsilon}'_{ij_{(\text{plastic})}}, \tag{2.3.14}$$

in a way that

$$\dot{\varepsilon}'_{ij_{(\text{plastic})}} = \begin{cases} 0, & \text{if } \tau_{II} < \tau_{\text{yield}}, \\ \varsigma \frac{\tau_{ij}}{\tau_{II}}, & \text{if } \tau_{II} = \tau_{\text{yield}}, \end{cases} \tag{2.3.15}$$

for example, where $\tau_{II} = \sqrt{\frac{1}{2}\tau_{ij}^2}$, is called the plastic flow potential reflecting the amount of mechanical energy per unit volume that supports plastic deformation, and τ_{yield} is the plastic yield strength for a given rock. The parameter ς is called a plastic multiplier, which is some scaling coefficient.

Like the different permeability models, it is easy to modify the rock rheology into our system of equations. However, throughout this thesis, we assume that the rock behaves as a viscous fluid only, and define our shear stress tensor components as

$$\tau_{ij} = 2\mu_r \dot{\varepsilon}_{ij} \tag{2.3.16}$$

as in (2.3.13).

2.3.2.4 Thermal conductivity

We use a geometrically weighted thermal conductivity, $\kappa_T(\phi)$, defined by

$$\kappa_T(\phi) = \kappa_{T\text{fluid}}^{\phi} \kappa_{T\text{rock}}^{(1-\phi)}, \tag{2.3.17}$$

where $\kappa_{T\text{fluid}}$ and $\kappa_{T\text{rock}}$ denote the thermal conductivities of the fluid and rock phases, respectively. This model was suggested by Horai (1971) and it is an empirically derived law. We choose this model in particular as it has been calibrated against data from materials found in the Earth's crust, and is therefore suitable for basin modelling. This weighted function is valid in both the fluid and rock phases.

2.3.2.5 Modelling parameters in the compaction equation

We assume that the (dimensionless) chemical compaction term, $C(\phi)$, takes the form

$$C(\phi) = \tilde{C}\phi^m(1-\phi)^n, \tag{2.3.18}$$

which is based on the chemical compaction model by Schneider et al. (1996), who originally defined this term to be modelled as

$$C(\phi) \sim \begin{cases} 1-\phi, & \phi > \phi_{\min}, \\ 0, & \phi \leq \phi_{\min}, \end{cases} \tag{2.3.19}$$

where $\phi_{\min}$ is some minimum porosity.

Our chemical compaction term is an improvement to the model in (2.3.19) by Schneider et al. (1996) that is valid for all $\phi \in [0,1]$ to additionally state that no compaction can happen if there is no fluid in the system (when $\phi = 0$) in a single continuous equation. Further, the improved model given in (2.3.18) is easily adjustable to accommodate different rock types, by modifying the parameters $\tilde{C}, m$, and n. We expect these values to be determined by available data.

For example, for shale, data provided by Senior et al. (2016) gives $\tilde{C} = 0.013, m = 0.3, n = 1.1$, hence (2.3.18) becomes

$$C(\phi) \sim 0.013\phi^{0.3}(1-\phi)^{1.1}. \tag{2.3.20}$$

We found this by using numerous sets of data for the porosity profiles of a basin made up of shale sediments provided by Senior et al. (2016) and used our compaction equation to fit the parameters. The data provided are obtained from using a numerical model which inversely models the compaction process given current data via a process called backstripping. The purely numerical model uses a trial and error-type approach to obtain an approximation of the variables during the basin's evolution. Using current data, they simulate the basin's evolution in an iterative manner until the final results match the current data.

From the porosity data and knowing or estimating the remaining values, we plotted the values of the estimated $C(\phi)$ values at various time points in the simulation. Note that for ϕ smaller than around 0.05, Senior et al. (2016) assume that $D\phi/Dt \approx 0$, and hence we assume and take $C = 0$ for $\phi = 0$. The term $C(\phi)$ was calculated by assuming that our compaction equation holds and rearranging the compaction equation (2.2.30) for C to obtain the value. Note that the values for ϕ_0, χ, p_f, and μ_r were provided, p_r was estimated based on the lithostatic pressure, and $\boldsymbol{v}_r$ which is

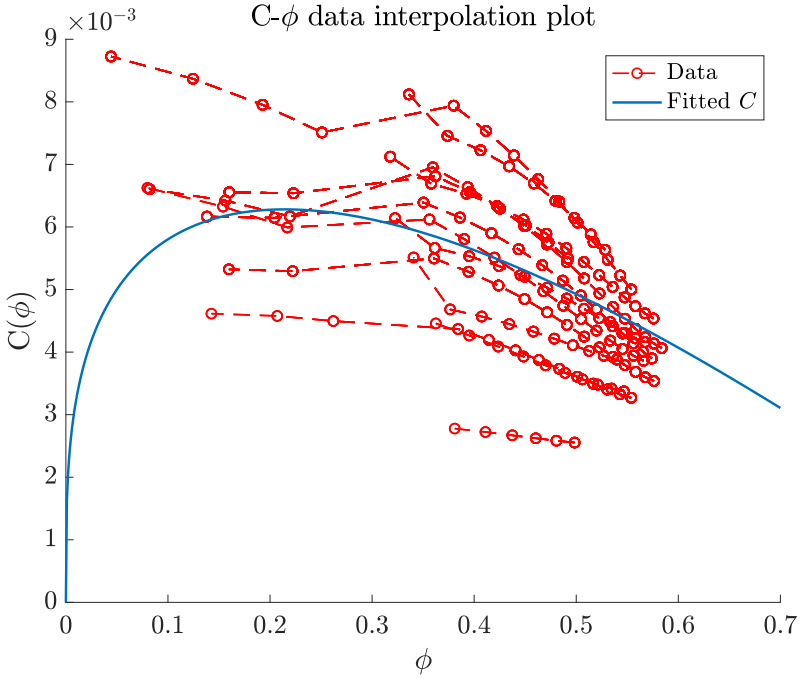


Figure 2.2: Plot for the fit of $C(\phi)$ to data.

used within the material derivative was calculated by taking the difference between the distance compacted over the timestep used and the sedimentation rate at the respective timestep. Then, further assuming that the chemical compaction coefficient C takes the form as given in (2.3.18), we find suitable values for $\tilde{C}, m$, and n by using the `fit` function in MATLAB. Figure 2.2 shows the plots for the different C values obtained from the data, with our final analytical equation for the approximation of C. After discussions with Senior et al. (2016), we believe that our model for C is sufficient to approximate the chemical compaction coefficient correctly. Further, we are now able to mathematically model this term based on the data provided by Senior et al. (2016), which was not available before.

2.4 Nondimensionalisation and scaling

2.4.1 Nondimensionalisation

Now that we have derived our complete model, we can nondimensionalise and identify any dimensionless parameters that govern the system. To begin, we scale the spatial dimensions with a suitably chosen length scale, d, to be defined shortly. Our velocities are scaled by a typical sedimentation rate, H_0 (which has the same units as velocity), so that our time scale is d/H_0. Choosing the pressure scale to be $p_0 = \rho_0 g d$, where ρ_0

is an appropriate scale for the densities ($\rho_0 = \rho_r - \rho_f$, for example), and choosing the temperature scale to be T_0, a reference temperature, we can write the variables as

$$x = dx^*, \quad z = dz^*, \quad t = \frac{d}{H_0}t^*, \quad T = T_0 T^*, \quad H = H_0 H^*,$$
$$\boldsymbol{v}_r = H_0 \boldsymbol{v}_r^*, \quad \boldsymbol{v}_f = H_0 \boldsymbol{v}_f^*, \quad p_f = \rho_0 g d p_f^*, \quad p_r = \rho_0 g d p_r^*,$$

with the asterisks denoting dimensionless variables. Note that the porosity is already a dimensionless variable, and we choose not to scale it bearing in mind that it is almost always $\mathcal{O}(10^{-1})$.

We also nondimensionalise our parameters and constitutive relationships with appropriate average values such that each asterisked parameter is $\mathcal{O}(1)$, and write

$$c_r = c_0 c_r^*, \quad c_f = c_0 c_f^*, \quad \mu_r = \mu_{r0}\mu_r^*, \quad \kappa_T = \kappa_{T0}\kappa_T^*,$$
$$k = k_0 k^*, \quad \rho_r = \rho_0 \rho_r^*, \quad \rho_f = \rho_0 \rho_f^*,$$

where c_0 is a typical value of the rock heat capacity, μ_{r0} is a typical velocity of the rock when modelled as a fluid (similar to that of slow-flowing lava), k_0 is a typical value of the permeability of the rock, and κ_{T0} is a typical value of the averaged thermal conductivity of the two phases. With these scalings, note that we now also write

$$h_0 = dh_0^*, \quad h_N = dh_N^*, \quad X = dX^*, \quad q = \frac{\kappa_{T0}T_0}{d}q^*, \quad \theta = \frac{T_0}{d}\theta^*.$$

Note here that from now on, we will choose to assume that the rock behaves viscously only. The scaling for the rock strain rate tensor $\underline{\underline{\boldsymbol{\tau}}}$ then comes from the form for viscous rheology, given by

$$\tau_{ij} = 2\mu_r \dot{\varepsilon}_{ij}, \tag{2.4.1}$$

where

$$\dot{\varepsilon}_{ij} = \frac{1}{2}\left(\frac{\partial v_{ri}}{\partial x_j} + \frac{\partial v_{rj}}{\partial x_i}\right), \tag{2.4.2}$$

so that we write

$$\underline{\underline{\boldsymbol{\tau}}} = \frac{\mu_{r0}H_0}{d}\underline{\underline{\boldsymbol{\tau}}}^*. \tag{2.4.3}$$

Then, neglecting source terms in the conservation of mass and energy equations for the moment, we obtain the following system of dimensionless equations (dropping

asterisks):

$$\frac{\partial}{\partial t}((1-\phi)\rho_r) = -\nabla\cdot((1-\phi)\rho_r\boldsymbol{v}_r), \tag{2.4.4}$$

$$\frac{\partial}{\partial t}(\phi\rho_f) = -\nabla\cdot(\phi\rho_f\boldsymbol{v}_f), \tag{2.4.5}$$

$$\phi(\boldsymbol{v}_r - \boldsymbol{v}_f) = \lambda k(\nabla p_f + \rho_f\hat{\boldsymbol{z}}), \tag{2.4.6}$$

$$-((1-\phi)\rho_r + \phi\rho_f)\hat{\boldsymbol{z}} - \nabla((1-\phi)p_r + \phi p_f) + \alpha\nabla\cdot((1-\phi)\underline{\underline{\boldsymbol{\tau}}}) = \mathbf{0}, \tag{2.4.7}$$

$$\frac{D\phi}{Dt} = -\phi_0\Gamma\exp\left(-\Gamma(p_r - p_f)\right)\frac{D}{Dt}(p_r - p_f) - \Upsilon\,\frac{C(\phi)}{\mu_r}(p_r - p_f), \tag{2.4.8}$$

$$\frac{\partial}{\partial t}((\phi\rho_f c_f + (1-\phi)\rho_r c_r)T) + \nabla\cdot((\phi\rho_f c_f\boldsymbol{v}_f + (1-\phi)\rho_r c_r\boldsymbol{v}_r)T) = \frac{1}{\mathrm{Nu}}\nabla\cdot(\kappa_T\nabla T), \tag{2.4.9}$$

where our dimensionless numbers are $\lambda, \alpha, \Gamma, \Upsilon$, and Nu, all of which we define in the next subsection. These equations have corresponding initial and boundary conditions as summarised in Figure 2.3, where $\boldsymbol{n}$ and $\boldsymbol{t}$ are the outward normal and tangential vectors with respect to their corresponding boundaries, respectively. Note that $\hat{\boldsymbol{z}}$ is the unit vector in the positive z-direction.

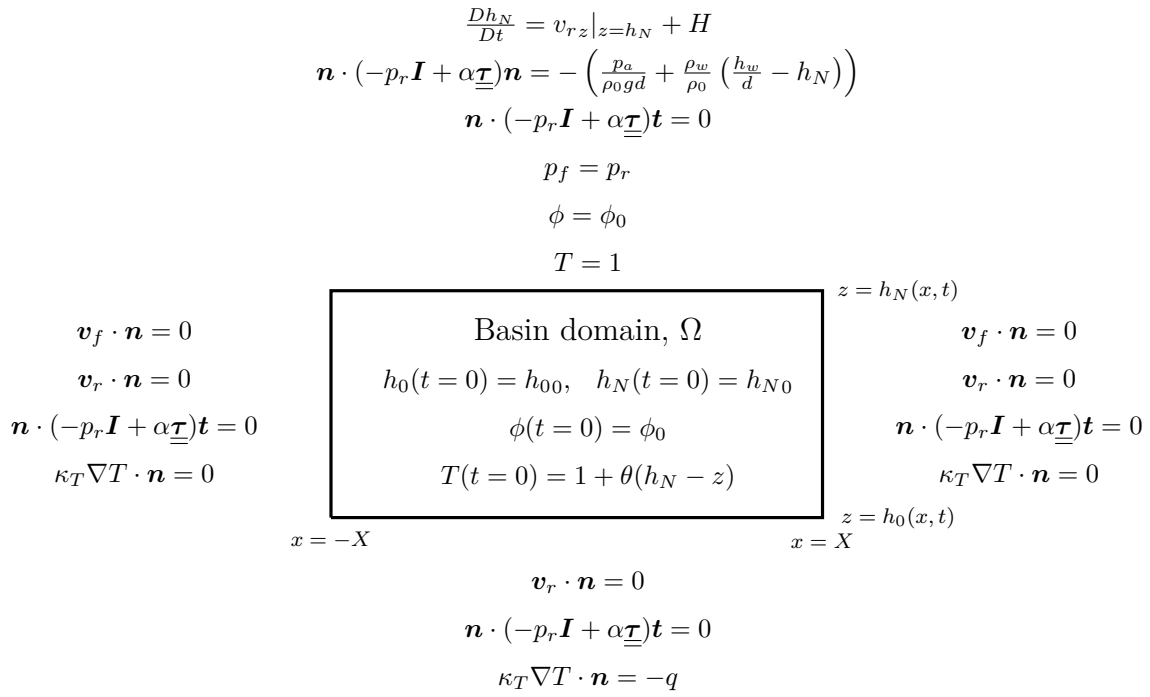


Figure 2.3: Summary of our dimensionless initial and boundary conditions on the basin domain, Ω.

2.4.2 Summary of dimensionless parameters and groups

We can estimate the values of our parameters using typical values from observations. The typical orders of magnitudes for the scaling of relevant parameters are shown in Table 2.1, where the values in permeability and viscosity depend largely on the rock type. These values are sourced from Gerya (2010) and Senior et al. (2016). Then for the given dimensionless governing equations (2.4.4–2.4.9), the dimensionless group of the resultant dimensionless numbers are defined and their typical orders shown in Table 2.2. Note that the range of dimensionless values we have defined have been calculated using the extreme values of dimensionless scales for all rock lithologies.

Parameter	Typical value	Units	Source
d	$\mathcal{O}(10^{3})$	m	Senior et al. (2016)
H_0	$\mathcal{O}(10^{-11}) - \mathcal{O}(10^{-10})$	m s^{-1}	Senior et al. (2016)
g	$\mathcal{O}(10^{1})$	m s^{-2}	-
ρ_0	$\mathcal{O}(10^{3})$	kg m^{-3}	Senior et al. (2016)
k_0	$\mathcal{O}(10^{-21}) - \mathcal{O}(10^{-13})$	m^2	Senior et al. (2016)
μ_f	$\mathcal{O}(10^{-3}) - \mathcal{O}(10^{-1})$	kg m^{-1} s^{-1}	Senior et al. (2016)
μ_{r0}	$\mathcal{O}(10^{17}) - \mathcal{O}(10^{21})$	kg m^{-1} s^{-1}	Gerya (2010)
ϕ_0	$\mathcal{O}(10^{-1})$	-	-
χ	$\mathcal{O}(10^{-8})$	m s^2 kg^{-1}	Senior et al. (2016)
c_0	$\mathcal{O}(10^{3})$	m^2 s^{-2} °C^{-1}	Senior et al. (2016)
κ_{T0}	$\mathcal{O}(10^{0})$	kg m s^{-3} °C^{-1}	Senior et al. (2016)
T_0	$\mathcal{O}(10^{1})$	°C	-

Table 2.1: Table of parameters and their typical values.

Name	Symbol	Typical value	Definition
Sedimentation number	λ	$\mathcal{O}(10^{-6}) - \mathcal{O}(10^{5})$	$\frac{k_0\rho_0 g}{\mu_f H_0}$
Strain rate number	α	$\mathcal{O}(10^{-4}) - \mathcal{O}(10^{1})$	$\frac{\mu_{r0} H_0}{\rho_0 g d^2}$
Mechanical compaction number	Γ	$\mathcal{O}(10^{-1})$	$\chi\rho_0 g d$
Reynolds number	Re	$\mathcal{O}(10^{-26}) - \mathcal{O}(10^{-21})$	$\frac{\rho_0 H_0 d}{\mu_{r0}}$
Richardson number	Ri	$\mathcal{O}(10^{24}) - \mathcal{O}(10^{26})$	$\frac{gd}{H_0^2}$
Chemical compaction number	Υ	$\mathcal{O}(10^{-2}) - \mathcal{O}(10^{5})$	Re Ri
Prandtl number	Pr	$\mathcal{O}(10^{20}) - \mathcal{O}(10^{24})$	$\frac{c_0\mu_{r0}}{\kappa_{T0}}$
Nusselt number	Nu	$\mathcal{O}(10^{-6}) - \mathcal{O}(10^{3})$	Pr Re

Table 2.2: Table of the dimensionless group of numbers and their typical values.

Note that the parameter λ can be either large or small depending on the lithology,

assuming that the sedimentation rate does not vary greatly amongst different rock types. This parameter is similar to that found by Audet and Fowler (1992), who present an asymptotic analysis of the porosity profile within a basin for $\lambda \ll 1, \lambda = \mathcal{O}(1)$, and $\lambda \gg 1$. Though Fowler and Yang (1998) claim that large values of λ are more likely, discussions with our industrial partner, PDS, suggest that any value of λ in the range shown in Table 2.2 can be seen in real basins, since the permeability can vary so greatly.

We also assumed that the rock only behaves viscously. Hence, choosing our scaling for the rock strain rate tensor appropriately, we then have

$$\alpha = \frac{\mu_{r0} H_0}{\rho_0 g d^2}. \tag{2.4.10}$$

The Reynolds and Richardson numbers for the problem are very small and very large, respectively, but only appear as a product with each other in the chemical compaction number, Υ, in (2.4.8). Similarly, the Prandtl number is large, but only appears as a product with the Reynolds number (in the form of the Nusselt number), and therefore will not cause overflow issues when we solve the system numerically, nor analytic issues, such as with boundary conditions. No other terms that appear are very large or very small. An overview of all the symbols, typical values and orders of magnitudes used in the system are presented collectively in Table 2.3 at the end of this chapter. Note that the typical values of some quantities, such as the velocities and depth of layers, vary greatly depending on the geometry. Hence we omit defining such values at this stage.

2.5 Summary of Chapter 2

2.5.1 The developed model

In this chapter, we have presented our multi-dimensional model for the evolution of pressures, velocities, porosity, and temperature within a basin. The model also describes the effects of both mechanical and chemical compaction for rocks that are subject to shear stresses. The compaction components are dependent on the rock and fluid pressures rather than the usual effective stress based on the lithostatic and pore pressures, and the chemical compaction model is an improvement to a previous model.

The model as written can accommodate a number of rock rheologies, as well as the physical properties of multiple sedimentary layers. The constitutive relationships can be used to model a number of different rock types in appropriate settings. Further, it

provides the base framework for a model which can be easily modified to take into account structural deformities and other geological phenomena, such as sedimentation, diagenesis, and sills.

We have defined appropriate initial and boundary conditions for a two-dimensional model, where the third dimension can be easily added by using analogous boundary conditions to those in the x-direction for the third dimension. The model was finally nondimensionalised, and the resulting dimensionless numbers and their typical values were identified.

2.5.2 Relevance to existing models

We briefly discuss the significance of the new model and its improvements on existing ones. The porosity equation described by (2.2.30) is one we have newly developed. We derived this by considering two different models, one of which expresses compaction behaviour with respect to loading (Athy, 1930), and the other which concentrates on chemical compaction due to viscous properties of the rock (Schneider et al., 1996). By combining a variation of the two into a new compaction model, we are able to incorporate the effects of both mechanical and chemical compaction in the basin into our system. Thus far, we have not encountered a model which incorporates these effects into a single compaction model within a unified coupled system in available literature. Hence, we are able to provide our industrial partner, PDS, with a more complex compaction model that is easy to modify.

Further, we have not encountered (in available literature) the use of the rock pressure to define the effective stress in the compaction equation instead of using the lithostatic pressure. By using the rock pressure, we are able to incorporate additional forces that may further affect compaction, like viscous forces or forces arising from the interfacial interaction between the two phases. Further, since lithostatic pressure is a purely vertical process whereas the rock pressure can also be laterally varying, we are able to incorporate two-dimensional spatial effects into the compaction process.

Another feature of our model is that it can incorporate multiple geological phenomena into a single model. This is important in industry and to PDS, due to resulting efficiency and ease of implementation. Existing models tend to focus on a certain geological process, such as thermal analysis (Luo and Vasseur, 1992) or the fluid and rock motion (Yang, 2002), but fail to unify these and rather consider them as separate systems. Wangen (1992) explains how the pressure and temperature may be coupled, but then makes them independent when solution methods are discussed, and analyses the two profiles separately. For example, from our governing equations (2.4.4–2.4.9),

we can see that the porosity affects the fluid and rock motion as well as the temperature, and many of the constitutive relationships require the knowledge of the porosity and temperature. Whilst many models simplify this inter-variable dependence by considering each process separately, we have developed a unified model to describe the co-dependent behaviour of the most significant processes within a basin which we now aim to solve.

Finally, we have defined the complete model in multiple dimensions, taking into account the existence of lateral stresses experienced by the rock and the possibility of lateral fluid flow. These are known to affect the pressure, porosity, and temperature profiles significantly as previously discussed (Yardley and Swarbrick, 2000). Whilst most of the literature concentrates on compaction (e.g. Fowler and Yang (1998)), and therefore simplifies the models into a single dimension, we have not restricted our attention to compaction alone, so that our model remains in the most general form. Additionally, many existing models are simplified into a unidirectional decoupled system (for example, in Wangen (1992) and also for solvers used by PDS), so that it is easier to solve numerically, whereas we develop a scheme to solve the system as it is with higher dimensions. Recall that the ability to model in multiple dimensions is a desirable feature to PDS and also in industry.

In summary, having our model in a general form then sets up the framework on which we can add geological features, such as sills and fault lines, via source terms. The inclusion of these features into a mathematical model describing basin evolution is rarely seen in literature (Wangen (2002) discusses how to model the pressure within a seal, but not on a basin scale), and are usually directly incorporated numerically into simulations (e.g., Coates and Schoenberg (1995)). Note that since these can also significantly affect the properties within the basin in the lateral direction, we believe that using a mathematical model in higher dimensions is crucial to properly describing the many phenomena within a basin. This modelling approach is also of particular interest to our collaborators, PDS, who wished to have a general multi-dimensional model in space which is easy to use and modify where necessary.

Symbol	Description	Typical value/order of magnitude	Units
C	Chemical compaction function	-	-
c_f	Heat capacity of fluid	$\mathcal{O}(10^3)$	$\mathrm{m^2\,{}^\circ C^{-1} s^{-2}}$
c_r	Heat capacity of rock	$\mathcal{O}(10^3)$	$\mathrm{m^2\,{}^\circ C^{-1} s^{-2}}$
$\boldsymbol{g}$	Gravitational acceleration vector	$(0, 0, \mathcal{O}(10^1))^T$	$\mathrm{m\,s^{-2}}$
H	Sedimentation rate	$\mathcal{O}(10^{-11}) - \mathcal{O}(10^{-10})$	$\mathrm{m\,s^{-1}}$
h_b	Distance to bottom of basement layer	-	m
h_i	Distance to boundary of ith layer	-	m
h_n	Distance to top boundary of basin	-	m
h_w	Distance to top of seawater layer	-	m
k	Permeability	$\mathcal{O}(10^{-21}) - \mathcal{O}(10^{-13})$	$\mathrm{m^2}$
Nu	Nusselt number	$\mathcal{O}(10^{-6}) - \mathcal{O}(10^3)$	-
p_a	Atmospheric pressure	$\mathcal{O}(10^{-2})$	$\mathrm{kg\,m^{-1}\,s^{-2}}$
p_B	Ref. pressure at bottom of basement layer	-	$\mathrm{kg\,m^{-1}\,s^{-2}}$
p_f	Pore fluid pressure	-	$\mathrm{kg\,m^{-1}\,s^{-2}}$
p_L	Geostatic pressure	-	$\mathrm{kg\,m^{-1}\,s^{-2}}$
p_r	Rock pressure	-	$\mathrm{kg\,m^{-1}\,s^{-2}}$
Pr	Prandtl number	$\mathcal{O}(10^{20}) - \mathcal{O}(10^{24})$	-
Re	Reynolds number	$\mathcal{O}(10^{-26}) - \mathcal{O}(10^{-21})$	-
Ri	Richardson number	$\mathcal{O}(10^{24}) - \mathcal{O}(10^{26})$	-
T_0	Reference/'atmospheric' temperature	$\mathcal{O}(10^1)$	$^\circ$C
T	Temperature	-	$^\circ$C
$\boldsymbol{v_f}$	Fluid velocity	-	$\mathrm{m\,s^{-1}}$
$\boldsymbol{v_r}$	Rock velocity	-	$\mathrm{m\,s^{-1}}$
α	Dimensionless strain rate number	$\mathcal{O}(10^{-4}) - \mathcal{O}(10^1)$	-
Γ	Dimensionless mechanical compaction number	$\mathcal{O}(10^{-1})$	-
Υ	Dimensionless chemical compaction number	$\mathcal{O}(10^{-2}) - \mathcal{O}(10^5)$	-
κ_T	Bulk Thermal conductivity	$\mathcal{O}(10^0)$	$\mathrm{kg\,m\,s^{-3}\,{}^\circ C^{-1}}$
λ	Dimensionless sedimentation number	$\mathcal{O}(10^{-6}) - \mathcal{O}(10^5)$	-
μ_f	Viscosity of fluid	$\mathcal{O}(10^{-3}) - \mathcal{O}(10^{-1})$	$\mathrm{kg\,m^{-1}\,s^{-1}}$
μ_r	Viscosity of rock	$\mathcal{O}(10^{17}) - \mathcal{O}(10^{21})$	$\mathrm{kg\,m^{-1}\,s^{-1}}$
ρ_f	Density of fluid	$\mathcal{O}(10^3)$	$\mathrm{kg\,m^{-3}}$
ρ_r	Density of rock	$\mathcal{O}(10^3)$	$\mathrm{kg\,m^{-3}}$
$\underline{\underline{\boldsymbol{\tau}}}$	Shear stress tensor	-	$\mathrm{kg\,m^{-1}\,s^{-2}}$
ϕ	Porosity	$\mathcal{O}(10^{-1})$	-
χ	Mechanical compaction coefficient	$\mathcal{O}(10^{-8})$	$\mathrm{m\,s^2\,kg^{-1}}$

Table 2.3: List of symbols and their typical values.

Chapter 3

Numerical modelling of a basin and solver development

In Chapter 2, we developed a general model that describes the evolution of fluid and rock motion, porosity, and temperature within a sedimentary basin. In this chapter, we develop our initial method for calculating a numerical solution of the governing equations, thereby forming the foundation of the computational work in this thesis. We first decompose the system of six equations into four subsystems with known solution techniques. Then, after describing any tools and techniques we use, we provide an overview of the methods with which we solve each subsystem. Having built the numerical solver of a simplified model, its validity is then tested using the method of manufactured solutions, and we implement a convergence study. Finally, we discuss the methods with which we numerically incorporate the sedimentation and compaction processes into our simulations.

3.1 Model decomposition

In order to solve our system of equations with boundary and initial conditions as defined in Chapter 2, we use the method of splitting combined with the finite element method. Splitting is a process where a complicated system of equations is broken down into smaller parts which are easier to solve. The smaller systems are then solved in some sequence where the solutions of one can be used to solve the remaining smaller systems. The sequential solutions of the smaller problems then make up the solution to the original problem.

For our system of equations, we split our dimensionless system into four subsystems, one each for the rock motion (concerning rock velocity and pressure), fluid motion (concerning fluid velocity and pressure), porosity, and temperature, such that it allows

the application of numerical methods outlined in subsequent sections. The rock and fluid motion subsystems then consist of two equations each and are derived from the two sets of momentum and mass conservation equations (2.4.4–2.4.7). The porosity and temperature subsystems consist of the equations as they were originally derived ((2.4.8) and (2.4.9), respectively). The decomposition and manipulations of equations are presented in this section.

3.1.1 Derivation of rock and fluid subsystems

Before we discuss the subsystem solution sequence and define the subsystems in full, we present the derivation of the rock and fluid subsystems. This is necessary since the original equations for the rock and fluid motion must be manipulated and rewritten in such a way that is suitable for our solution sequence.

3.1.1.1 Rock subsystem equations

In Chapter 2, we derived a model for a general model which can accommodate a multitude of constitutive equations. However, from now on, we will assume that the densities of both rock and solution phases are constant. The rock and fluid densities in general only vary significantly at very high temperatures of above 600°C (Senior et al., 2016). However, given the depths of most basins (around 5km in general and a few up to 10km in depth (Senior et al., 2016)), and also given the temperature gradients in a geostatic basin (the temperature usually increases between around 25°C and up to 50°C per km (Speece et al., 1985; Halim, 1994)), it is unlikely that we would experience significant density variations in general. We assume that our basin is not subject to any extreme conditions and therefore this assumption is physically realistic for general basins.

With the assumption that the densities are constant, we combine (2.4.4) and (2.4.5) to obtain the first equation for the rock subsystem:

$$\nabla \cdot ((1-\phi)\boldsymbol{v}_r) = -\nabla \cdot (\phi \boldsymbol{v}_f). \tag{3.1.1}$$

The second equation in the rock subsystem is simply (2.4.7) rearranged, so that

$$\alpha \nabla \cdot ((1-\phi)\underline{\underline{\boldsymbol{\tau}}}(\boldsymbol{v}_r)) - \nabla((1-\phi)p_r) = \nabla(\phi p_f) + ((1-\phi)\rho_r + \phi\rho_f)\hat{\boldsymbol{z}}. \tag{3.1.2}$$

Hence, we arrive at a pair of equations similar to Stokes equations for the rock. Given that the fluid pressure and fluid velocity are known or can be approximated (and therefore the right hand sides are known), these two equations allow us to solve for the rock velocity and pressure. The boundary conditions remain the same.

3.1.1.2 Fluid subsystem equations

For the first fluid subsystem equation, we take the divergence of the fluid momentum conservation equation (2.4.6) and substitute for $-\nabla \cdot (\phi \boldsymbol{v}_f)$ using (3.1.1) to obtain

$$-\nabla \cdot (\lambda k \nabla p_f) = -\nabla \cdot \boldsymbol{v}_r + \nabla \cdot (\lambda k \rho_f \hat{\boldsymbol{z}}). \tag{3.1.3}$$

Note that the fluid velocity variable $\boldsymbol{v}_f$ has been eliminated in (3.1.3) and thus we can solve for p_f by knowing $\boldsymbol{v}_r$ alone (with appropriate boundary conditions). The second equation in the subsystem is obtained simply by rearranging (2.4.6), such that

$$\boldsymbol{v}_f = \boldsymbol{v}_r - \frac{\lambda k}{\phi}(\nabla p_f + \rho_f \hat{\boldsymbol{z}}), \tag{3.1.4}$$

which can be solved easily if $\boldsymbol{v}_r$ and p_f (or ∇p_f) are known.

Note that in arriving at equation (3.1.3), we have taken the divergence of the momentum equation. Taking the equations without knowledge of the pre-manipulated equation, we require an additional boundary condition for the problem to be well-posed. Since we assume that the bottom boundary where the basin and the basement layer meet is impermeable to both fluid and rock, we can impose that $\boldsymbol{v}_r \cdot \boldsymbol{n} = 0$ and $\boldsymbol{v}_f \cdot \boldsymbol{n} = 0$ at the bottom boundary. Then, from (3.1.4), we have that

$$\nabla p_f \cdot \boldsymbol{n} = -\rho_f \tag{3.1.5}$$

on the bottom boundary. The conditions on all other boundaries for the fluid remain the same.

Hence, we obtain a system of 'stationary' algebraic equations for the rock and fluid subsystems, with the explicit time dependence appearing in the porosity and temperature subsystems only.

3.1.2 Definition of each subsystem

We summarise each split subsystem here with the boundary conditions with which we solve the separate parts. While we discuss our numerical work and verify that the solver is correct, let us reduce our domain of interest to the basin only without the underlying basement layer or the overlying water layer, and let us also assume that the domain is fixed and constant.

For the rock subsystem, the equations are written as

$$\alpha \nabla \cdot ((1-\phi)\underline{\underline{\boldsymbol{\tau}}}(\boldsymbol{v}_r)) - \nabla((1-\phi)p_r) = \nabla(\phi p_f) + ((1-\phi)\rho_r + \phi\rho_f)\hat{\boldsymbol{z}}, \tag{3.1.6}$$

$$\nabla \cdot ((1-\phi)\boldsymbol{v}_r) = -\nabla \cdot (\phi \boldsymbol{v}_f), \tag{3.1.7}$$

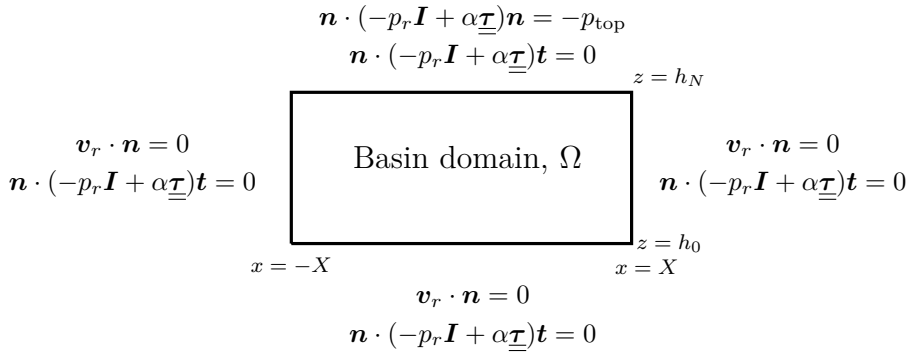


Figure 3.1: Summary of the boundary conditions for the rock subsystem.

which are accompanied by simplified boundary conditions as in Figure 3.1, where p_{top} is known.

The fluid subsystem consists of equations in the following rewritten form,

$$-\nabla\cdot(\lambda k\nabla p_f)=-\nabla\cdot\boldsymbol{v}_r+\nabla\cdot(\lambda k\rho_f\hat{\boldsymbol{z}}), \tag{3.1.8}$$

$$\boldsymbol{v}_f=\boldsymbol{v}_r-\frac{\lambda k}{\phi}(\nabla p_f+\rho_f\hat{\boldsymbol{z}}). \tag{3.1.9}$$

This subsystem of the two fluid equations is accompanied by boundary conditions as in Figure 3.2. The boundary conditions on the side and bottom boundaries have

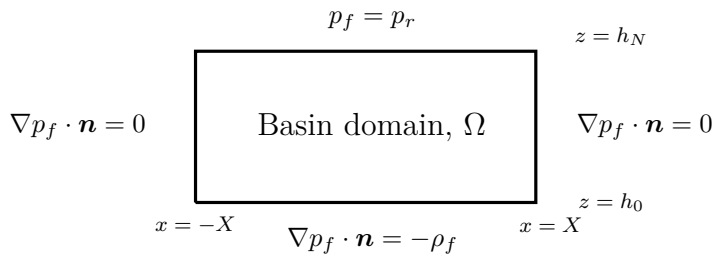


Figure 3.2: Summary of the boundary conditions for our Darcy-type subsystem.

been obtained by noting that the side boundaries are vertical for all time and that the bottom boundary is horizontal for all time, and by using (3.1.9).

The porosity equation is as originally written, given by

$$\frac{D\phi}{Dt}=-\phi_0\Gamma\exp\left(-\Gamma(p_r-p_f)\right)\frac{D}{Dt}(p_r-p_f)-\Upsilon\frac{C(\phi)}{\mu_r}(p_r-p_f), \tag{3.1.10}$$

with initial and boundary conditions as shown in Figure 3.3 below. Recall from Section 2.2.2 that the only inflow boundary is the top boundary of the basin, and therefore, the boundary condition is only required there, as shown in Figure 3.3. This equation (3.1.10) alone makes up the porosity subsystem.

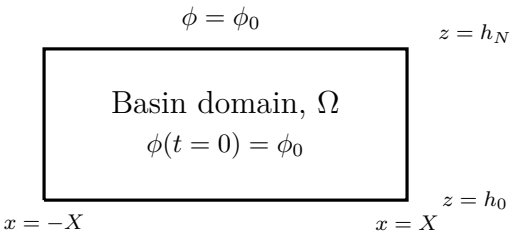


Figure 3.3: Summary of the boundary and initial conditions for ϕ in the porosity subsystem.

Finally, our temperature equation, again its own subsystem, is written

$$\frac{\partial}{\partial t}((\phi\rho_f c_f + (1-\phi)\rho_r c_r)T) + \nabla\cdot((\phi\rho_f c_f \boldsymbol{v}_f + (1-\phi)\rho_r c_r \boldsymbol{v}_r)T) = \frac{1}{\mathrm{Nu}}\nabla\cdot(\kappa_T \nabla T), \tag{3.1.11}$$

with initial and boundary conditions as shown in Figure 3.4.

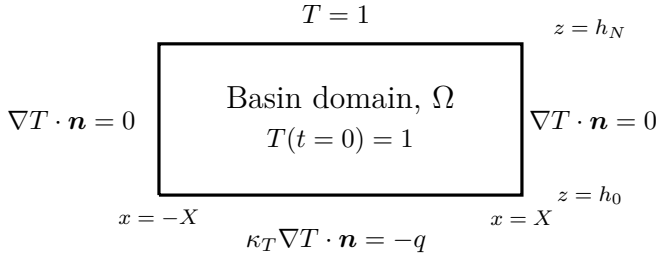


Figure 3.4: Summary of the boundary and initial conditions for the temperature subsystem.

3.1.3 Solution sequence

Let t_n denote the n-th timestep, with the 0th timestep corresponding to the initial time, and suppose that for our variables, we write, for example, $f^n = f(\boldsymbol{x}, t_n)$. Recall then that initially at $t = t_0$, the basin rests at some known reference temperature with known surface porosity. Hence, from the initial conditions as pictured above in Figures 3.3 and 3.4, we have that $\phi^0 = \phi_0$ and $T^0 = 1$.

Also approximating the fluid pressure and velocity initially with physically realistic functions (obtained from Senior et al. (2016)) so that p_f^0 and $\boldsymbol{v}_f^0$ are known, we obtain the solutions for the rock velocity $\boldsymbol{v}_r$ and rock pressure p_r at $t = t_0$ by solving (3.1.1) and (3.1.2), written as

$$\alpha\nabla\cdot((1-\phi^0)\underline{\underline{\boldsymbol{\tau}}}(\boldsymbol{v}_r^0)) - \nabla((1-\phi^0)p_r^0) = \nabla(\phi^0 p_f^0) + ((1-\phi^0)\rho_r + \phi^0\rho_f)\hat{\boldsymbol{z}}, \tag{3.1.12}$$

$$\nabla\cdot((1-\phi^0)\boldsymbol{v}_r^0) = -\nabla\cdot(\phi^0\boldsymbol{v}_f^0), \tag{3.1.13}$$

with appropriate boundary conditions as given in Figure 3.1. We then solve the fluid subsystem for the updated values of the fluid velocity and pressure, via our fluid subsystem equations given by

$$-\nabla \cdot (\lambda k \nabla p_f^0) = -\nabla \cdot \boldsymbol{v}_r^0 + \nabla \cdot (\lambda k \rho_f \hat{\boldsymbol{z}}), \tag{3.1.14}$$

$$\boldsymbol{v}_f^0 = \boldsymbol{v}_r^0 - \frac{\lambda k}{\phi^0}(\nabla p_f^0 + \rho_f \hat{\boldsymbol{z}}), \tag{3.1.15}$$

using the newly found values for the rock velocity and pressure (p_r^0 and $\boldsymbol{v}_r^0$ at the initial timestep), whilst still using the initial values for the porosity (ϕ^0) and temperature (T^0). This gives us the solutions for the fluid velocity $\boldsymbol{v}_f$ and fluid pressure p_f at $t = t_0$. We repeat this process until the approximate initial solutions correct to four decimal places for the rock and fluid velocities and pressure between each iterative step all converge to zero. We now have the approximate solutions to all our variables at $t = t_0$.

Having solved the 'stationary' system, we can now apply compaction and sedimentation and then solve the time-dependent equations for the solutions at the next timestep $t = t_1$. First, we use the calculated rock velocity at $t = t_0$ and the given sedimentation rate to modify our domain to the one that will be used at $t = t_1$, so that $\Omega^0 \to \Omega^1$. The details and exact method with which we move our mesh is discussed later in this chapter. Having adjusted our mesh, the porosity equation is solved for ϕ at time $t = t_1$ using the calculated solutions at the previous timestep, such that

$$\frac{D\phi^1}{Dt} = -\phi_0 \Gamma \exp\left(-\Gamma(p_r^0 - p_f^0)\right) \frac{D}{Dt}(p_r^0 - p_f^0) - \Upsilon \frac{C(\phi^0)}{\mu_r}(p_r^0 - p_f^0). \tag{3.1.16}$$

The exact timestepping scheme for the time derivative in this equation (3.1.16) is discussed in details later in this chapter as we present the discretisation of our system. Similarly, the temperature equation can then be solved again at $t = t_1$, using the porosity found at $t = t_1$ and using the remaining variables at $t = t_0$, such that

$$\frac{\partial}{\partial t}((\phi^1 \rho_f c_f + (1-\phi^1)\rho_r c_r)T^1) + \nabla \cdot ((\phi^1 \rho_f c_f \boldsymbol{v}_f^0 + (1-\phi^1)\rho_r c_r \boldsymbol{v}_r^0)T^1) = \frac{1}{\mathrm{Nu}} \nabla \cdot (\kappa_T \nabla T^1). \tag{3.1.17}$$

Having found the solutions for porosity and temperature at $t = t_1$, we return to the rock subsystem to solve for the rock pressure and velocity, and further the fluid velocity and pressure at $t = t_1$. Using the updated values of the rock and fluid velocities and pressures, we modify the domain again and solve for the porosity and temperature at the next timestep $t = t_2$ on the new domain. This process continues to repeat in the same way, where the porosity and temperature are solved for first at

each timestep for $t = t_n > t_0$ using the rock and fluid solutions found at $t = t_{n-1}$, then the rock and fluid subsystems sequentially at $t = t_n$ which are then used to modify the domain and solve for the porosity and temperature at $t = t_{n+1}$, and so on. Hence, in general, at $t = t_n$ for $n > 0$, we solve (in this order of equations)

$$\frac{D\phi^n}{Dt} = -\phi_0 \Gamma \exp\left(-\Gamma(p_r^{n-1} - p_f^{n-1})\right) \frac{D}{Dt}(p_r^{n-1} - p_f^{n-1}) - \Upsilon \frac{C(\phi^{n-1})}{\mu_r}(p_r^{n-1} - p_f^{n-1}), \tag{3.1.18}$$

$$\begin{aligned} \frac{\partial}{\partial t}((\phi^n \rho_f c_f + (1-\phi^n)\rho_r c_r)T^n) + \nabla \cdot ((\phi^n \rho_f c_f \boldsymbol{v}_f^{n-1} + (1-\phi^n)\rho_r c_r \boldsymbol{v}_r^{n-1})T^n) \\ = \frac{1}{\mathrm{Nu}} \nabla \cdot (\kappa_T \nabla T^n), \end{aligned} \tag{3.1.19}$$

$$\alpha \nabla \cdot ((1-\phi^n)\underline{\underline{\boldsymbol{\tau}}}(\boldsymbol{v}_r^n)) - \nabla((1-\phi^n)p_r^n) = \nabla(\phi^n p_f^{n-1}) + ((1-\phi^n)\rho_r + \phi^n \rho_f)\hat{\boldsymbol{z}}, \tag{3.1.20}$$

$$\nabla \cdot ((1-\phi^n)\boldsymbol{v}_r^n) = -\nabla \cdot (\phi^n \boldsymbol{v}_f^{n-1}), \tag{3.1.21}$$

$$-\nabla \cdot (\lambda k \nabla p_f^n) = -\nabla \cdot \boldsymbol{v}_r^n + \nabla \cdot (\lambda k \rho_f \hat{\boldsymbol{z}}), \tag{3.1.22}$$

$$\boldsymbol{v}_f^n = \boldsymbol{v}_r^n - \frac{\lambda k}{\phi^n}(\nabla p_f^n + \rho_f \hat{\boldsymbol{z}}), \tag{3.1.23}$$

with appropriate boundary conditions. As previously mentioned, we discuss and define the timestepping scheme of our time derivatives later in this chapter. We are now able to obtain the evolutionary profiles of our domain and the six unknown variables until some final time.

3.2 Numerical method and tools

In order to solve the subsystems, we use the finite element method to discretise the continuum model with tools from the open source C++ package, `deal.ii`. We briefly discuss the finite element method and the `deal.ii` library before we present the discretisation and weak forms for each subsystem.

3.2.1 A brief introduction to `deal.ii`

The open-source package `deal.ii` (Bangerth et al., 2016) derives from its predecessor, `deal`, which stands for 'differential equations analysis library', and uses the C++ language with some functionality provided by the PETSc library (Balay et al., 2019). It was originally developed at the University of Heidelberg, though it is now maintained concurrently by developers around the world. It has been developed to solve partial differential equations using the finite element method. It is a 'black box' type tool,

and provides incredible practical in-built functionality. Due to these pre-developed components and with the package being open-source, `deal.ii` is desirable for use on systems of equations similar to our model. Hence, after discussions with our industrial partner, employing `deal.ii` was recommended.

The practical automatic functions within `deal.ii` include mesh generation, quadrature formulae, mapping functions from reference to real elements, evaluation of the values and gradients of shape functions on cells (the relevance of these techniques to the finite element method are discussed in the next subsection), multiple linear solvers using various methods (e.g., conjugate gradient: an iterative method to solve systems of positive definite linear equations; minimal residual: a variant of the conjugate gradient method supporting symmetric indefinite systems, etc.), in-built preconditioners, and so forth (see (Arbenz, 2017) for further details on the techniques). It supports a large variety of finite element spaces, such as higher-order Lagrange spaces, Nedelec spaces, or discontinuous Galerkin spaces, as well as having good support for parallel computing, and a variety of useful output formats.

Further, a strong feature of and motivation behind the development of `deal.ii` is the ability to write a solver in such a way that it is (spatially) dimensionally independent. We use this to our advantage such that our code is able to run in three dimensions simply by changing the input from '2' to '3' under one namespace in the code. For the sake of simplicity and saving substantial computational time, we mostly demonstrate our solvers in two dimensions, but keep in mind that producing 3D results does not require much more than the adjustment and declaration of appropriate parameters, as we will see via some exemplar 3D simulation results in Chapter 4.

The features and tools within the `deal.ii` library extend far beyond those mentioned here, and we refer the reader to Bangerth et al. (2016) for more information. The practicality and ease of use of the library make it an appropriate tool for us to use in solving our system.

3.2.2 The finite element method

We now briefly outline the finite element method and present an overview of how the approximations to our solutions are calculated. We first divide the solution region into finite elements such that we partition the continuum. Note here that a particular feature of `deal.ii` is that it only accommodates rectangular or hexahedral elements in the triangulation. The data structures used within the package historically have been implemented using such elements, and therefore triangular or tetrahedral elements are unavailable within the library. Using rectangular or hexahedral elements is not a

problem in solving our system, but if necessary, a user can convert a pre-existing grid made up of triangular or tetrahedral elements into a grid of rectangular or hexahedral ones using a package called `tethex` (Artemyev, 2016), which was developed originally for `deal.ii`.

We use the finite element method for our entire system which evaluates an approximation to the solution by (usually) using low order polynomials on each element. By choosing some appropriate interpolation functions, defining appropriate element properties, and applying the method of variation of parameters to a function space (converting into a weak formulation), we can define and assemble our system over each element used in the discretisation. Solving for the nodal values of the sought function, by mapping to reference cells, and using appropriate quadrature formulae for the integrals, then gives us the solution for the global system on the real domain.

In solving our system, we use elements from various function spaces and appropriate basis functions for our variables. We then approximate each variable as $u(\boldsymbol{x}) \approx u_h(\boldsymbol{x}) = \sum_{i=1}^{N} U_i \psi_i(\boldsymbol{x})$, where N is the number of nodal points in our domain, Ω. The terms ψ_i are our respective appropriate trial functions, or finite element basis functions in their respective function spaces, for each variable. For example, we can use nodal basis functions where $\psi_i(\boldsymbol{x}_j) = \delta_{ij}$ with δ_{ij} denoting the Kronecker delta and with $\boldsymbol{x}_j$ denoting the node points in the mesh. Then the terms U_i are the degrees of freedom in our problem, such that $u_h(\boldsymbol{x}_j) = U_j$, meaning that U_j is the finite element solution at the nodal point $\boldsymbol{x}_j$.

After putting the system of equations into a weak formulation, where we integrate the differential equations and use the divergence theorem to lower the degree of the highest derivative, we map each element to a reference element for ease of quadrature calculations. The mapping, quadrature weights, and calculation of shape functions, etc., are all facilitated by the functionality within `deal.ii`. For all our calculations of the integrals over the cells and on their boundaries, we use a Gauss-type quadrature, of degree two more than the highest finite element degree in use. This results in a linear system for U where we assemble each problem appropriately over the elements, add the cell contributions into a global matrix, and finally solve the global system. We use the sparse direct solver UMFPACK (Bangerth et al., 2019) which is provided within the `deal.ii` library for all our linear systems in the verification.

3.3 Weak forms and system discretisation

We now present the weak forms of the subsystem equations and the function spaces used for each subsystem. We further discuss the discretisation and how we implement the boundary conditions in each of the subsystems.

3.3.1 Discretised rock equations

Recall our rock subsystem from equations (3.1.6), (3.1.7) and Figure 3.1, which solve for $\boldsymbol{v}_r$, the rock velocity, and p_r, the rock pressure, as

$$\alpha\nabla\cdot((1-\phi)\underline{\underline{\boldsymbol{\tau}}}(\boldsymbol{v}_r)) - \nabla((1-\phi)p_r) = \nabla(\phi p_f) + ((1-\phi)\rho_r + \phi\rho_f)\hat{\boldsymbol{z}}, \tag{3.3.1}$$

$$\nabla\cdot((1-\phi)\boldsymbol{v}_r) = -\nabla\cdot(\phi\boldsymbol{v}_f), \tag{3.3.2}$$

with zero tangential stresses on all boundaries, known normal components of the normal stress on the top boundary, and no normal flow on the side and bottom boundaries as shown in Figure 3.1.

Consider the Hilbert-Sobolev space $H^1(\Omega)$ defined by

$$H^1(\Omega) = \left\{ \varphi : \Omega \to \mathbb{R} \;\middle|\; ||\varphi||_{H^1} := \left(\int_\Omega \varphi^2 + |\nabla\varphi|^2 \, d\Omega \right)^{1/2} < \infty \right\}. \tag{3.3.3}$$

For the weak formulation, we multiply (3.3.1) and (3.3.2), respectively, by test functions $\boldsymbol{w} \in H^1(\Omega)^d$, where d is the dimension of the problem, and $\psi \in L^2(\Omega) = \{\varphi : \Omega \to \mathbb{R} \,\big|\, \int_\Omega |\varphi|^2 \, d\Omega < \infty\}$.

Then we want to find $\{\boldsymbol{v}_r, p_r\} \in H^1(\Omega)^d \times L^2(\Omega)$ such that

$$\begin{aligned} -(\nabla\boldsymbol{w}, \alpha(1-\phi)\underline{\underline{\boldsymbol{\tau}}})_\Omega + (\nabla\cdot\boldsymbol{w}, (1-\phi)p_r)_\Omega \\ + (\boldsymbol{w}\otimes\boldsymbol{n}, \alpha(1-\phi)\underline{\underline{\boldsymbol{\tau}}})_{\delta\Omega} - (\boldsymbol{w}\cdot\boldsymbol{n}, (1-\phi)p_r)_{\delta\Omega} \\ + (\psi, \nabla\cdot((1-\phi)\boldsymbol{v}_r))_\Omega = (\boldsymbol{w}, \boldsymbol{F}_1)_\Omega + (\psi, F_2)_\Omega, \end{aligned} \tag{3.3.4}$$

where $\otimes$ denotes the tensor product and $(\cdot,\cdot)_\Omega$ denotes the inner product in $L^2(\Omega)$. Further, $\delta\Omega$ is the domain boundary, $\boldsymbol{n}$ is the outward normal to the domain boundary, $\boldsymbol{F}_1$ is the right hand side of (3.3.1), and F_2 is the right hand side of (3.3.2).

Now, consider the boundary terms in the second line of (3.3.4). These can be written as

$$\begin{aligned} (\boldsymbol{w}\otimes\boldsymbol{n}, \alpha(1-\phi)\underline{\underline{\boldsymbol{\tau}}})_{\delta\Omega} - (\boldsymbol{w}\cdot\boldsymbol{n}, (1-\phi)p_r)_{\delta\Omega} \\ = \sum_{i,j=1}^{d} (n_i w_j, (1-\phi)(\alpha\tau_{ij} - p_r\delta_{ij}))_{\delta\Omega} \\ = (\boldsymbol{w}, \boldsymbol{n}\cdot((1-\phi)(\alpha\underline{\underline{\boldsymbol{\tau}}} - p_r\boldsymbol{I})))_{\delta\Omega}. \end{aligned} \tag{3.3.5}$$

The second component in the resulting inner product in (3.3.5) can be written as a combination of the normal and tangential components, such that

$$\boldsymbol{n}\cdot((1-\phi)(\alpha\underline{\underline{\boldsymbol{\tau}}}-p_r\boldsymbol{I}))=\underbrace{(\boldsymbol{n}\cdot(1-\phi)(\alpha\underline{\underline{\boldsymbol{\tau}}}-p_r\boldsymbol{I})\boldsymbol{n})}_{=-(1-\phi_0)p_{\text{top}}\text{ on }z=h_N}\boldsymbol{n}+\underbrace{(\boldsymbol{n}\cdot(1-\phi)(\alpha\underline{\underline{\boldsymbol{\tau}}}-p_r\boldsymbol{I})\boldsymbol{t})}_{=0\text{ on }\delta\Omega}\boldsymbol{t}, \tag{3.3.6}$$

recalling that ϕ_0 is the porosity at the top boundary, and $p_{\text{top}}=-\left(\frac{p_a}{\rho_0 gd}+\frac{\rho_w}{\rho_0}\left(\frac{h_w}{d}-h_N\right)\right)$ is the normal component of the normal stress on the top boundary. Now, the second term on the right hand side of (3.3.6) is zero on all boundaries and so disappears. The first term on the right hand side which represents the normal component of the normal stress therefore remains in the weak form for the top boundary. We choose our test function to satisfy $\boldsymbol{w}\cdot\boldsymbol{n}=0$ on the side and bottom boundaries, so that the only contribution to the right hand side of (3.3.5) comes from the top boundary. The no normal flux conditions on the sides and bottom do not appear in the weak form and will need to be imposed strongly. In summary, we have in weak form,

$$\begin{aligned}-(\nabla\boldsymbol{w},\alpha(1-\phi)\underline{\underline{\boldsymbol{\tau}}})_\Omega+(\nabla\cdot\boldsymbol{w},(1-\phi)p_r)_\Omega+(\psi,\nabla\cdot((1-\phi)\boldsymbol{v}_r))_\Omega\\ =(\boldsymbol{w},\boldsymbol{F}_1)_\Omega+(\psi,F_2)_\Omega+(\boldsymbol{w},(1-\phi_0)p_{\text{top}}\boldsymbol{n})_{\delta\Omega_t},\end{aligned} \tag{3.3.7}$$

where $\boldsymbol{v}_r,\boldsymbol{w}\in V=\{\boldsymbol{\varphi}\in H^1(\Omega)^d\,\big|\,\boldsymbol{\varphi}\cdot\boldsymbol{n}=0\text{ on }x=\pm X\text{ and on }z=h_0\}$, and $p_r,\psi\in L^2(\Omega)$, where our finite element spaces are defined on the previous page, and where $\delta\Omega_t$ denotes the top boundary of the basin.

Now suppose that $Q_{h,\varrho}$ denotes the finite dimensional space where $Q_{h,\varrho}\subset Q=L^2(\Omega)$. Then the discretised problem reads: find $\boldsymbol{v}_{rh}\in\tilde{Q}^d_{h,\varrho+1}$, where $\tilde{Q}^d_{h,\varrho+1}\subset Q^d_{h,\varrho+1}$ satisfying the boundary conditions in V, $p_{rh}\in Q_{h,\varrho}$, and where ϱ is the order of the finite element, such that

$$\begin{aligned}-(\nabla\boldsymbol{w}_h,\alpha(1-\phi_h)\underline{\underline{\boldsymbol{\tau}}}(\boldsymbol{v}_{rh}))_\Omega+(\nabla\cdot\boldsymbol{w}_h,(1-\phi_h)p_{rh})_\Omega\\ +(\psi_h,\nabla\cdot((1-\phi_h)\boldsymbol{v}_{rh}))_\Omega=(\boldsymbol{w}_h,\boldsymbol{F}_1)_\Omega+(\psi_h,F_2)_\Omega\\ +(\boldsymbol{w}_h,(1-\phi_0)p_{\text{top}}\boldsymbol{n})_{\delta\Omega_t},\end{aligned} \tag{3.3.8}$$

for all test functions $\boldsymbol{w}_h\in\tilde{Q}^d_{h,\varrho+1},\psi_{rh}\in Q_{h,\varrho}$.

Note that in general for Stokes-type systems, there are a number of finite element spaces that can be used but the spaces and corresponding basis functions cannot be arbitrarily chosen. For existence and uniqueness of solutions to the Stokes equation, the Ladyzhenskaya-Babuška-Brezzi (LBB) condition needs to be satisfied (Boffi et al., 2008). Consider a discretisation of the variational problem:

$$a(u,v)=\langle f,v\rangle, \tag{3.3.9}$$

for $u \in U, v \in V$, which reads: 'find $u_h \in U_h$ such that

$$a(u_h, v_h) = \langle f, v_h \rangle \tag{3.3.10}$$

for all $v_h \in V_h$ in the finite dimensional subspaces $U_h \subset U, V_h \subset V$'. For the discretised variational problem above to be well-posed, we require the following LBB condition (sometimes called the discrete inf-sup condition) to be satisfied: there is some $\alpha_h > 0$ such that

$$\inf_{u_h \in U_h} \sup_{v_h \in V_h} \frac{a(u_h, v_h)}{||u_h||\,||v_h||} = \inf_{v_h \in V_h} \sup_{u_h \in U_h} \frac{a(u_h, v_h)}{||u_h||\,||v_h||} = \alpha_h > 0. \tag{3.3.11}$$

Now, the continuous spaces before our discretisation satisfy this condition, and our choice of finite dimensional spaces in the discretisation also satisfy the condition (see Verfürth (1984) or Brezzi and Falk (1991) for the proof). In a more practical sense and in application to the Stokes equations, this means that we require the pressure variable to be a polynomial degree of 1 less than the velocity for stability if the velocity has a polynomial degree of $\varrho \geq 2$.

3.3.2 Discretised fluid problem

For the fluid subsystem, we solve using a mixed formulation. Note that although we can solve (3.1.8) as originally written, a mixed formulation is often used for similar equations, since it is said to provide more accurate approximations to the solutions (Masud and Hughes, 2002) and we are often interested in the pressure gradient rather than the pressure itself (in groundwater flow, for example). Hence, we use this for our Darcy-type equation. For further reading on this method, Masud and Hughes (2002) present a comprehensive review on the use of mixed finite elements for Darcy flow, and Brezzi and Fortin (1991) apply the idea to a few classical examples in their book.

For the mixed formulation, we introduce a dummy variable, $\boldsymbol{u}$, which represents a vector in the negative direction of the pressure gradient, so that

$$\boldsymbol{u} = -\nabla p_f. \tag{3.3.12}$$

Then, rewriting the two fluid equations in the fluid subsystem (3.1.8) and (3.1.9) into three equations to solve as a mixed formulation, we have

$$\boldsymbol{u} + \nabla p_f = \boldsymbol{0}, \tag{3.3.13}$$

$$-\nabla \cdot (\lambda k \boldsymbol{u}) = \nabla \cdot \boldsymbol{v}_r - \nabla \cdot (\lambda k \rho_f \hat{\boldsymbol{z}}), \tag{3.3.14}$$

$$\boldsymbol{v}_f = \boldsymbol{v}_r - \frac{\lambda k}{\phi}(\nabla p_f + \rho_f \hat{\boldsymbol{z}}), \tag{3.3.15}$$

where the resulting subsystem gives us two partial differential equations to find p_f and $\boldsymbol{u}$, the fluid pressure and its negative gradient, and an algebraic equation for $\boldsymbol{v}_f$, the fluid velocity. Note that our boundary conditions in terms of $\boldsymbol{u}$ now become $p_f = p_r$ on the top boundary, $\boldsymbol{u} \cdot \boldsymbol{n} = 0$ on the sides, and $\boldsymbol{u} \cdot \boldsymbol{n} = \rho_f$ on the bottom boundary.

We look for solutions in the space $H^{(div)} = \{\boldsymbol{x} \in L^2(\Omega) \,\big|\, \nabla \cdot \boldsymbol{x} \in L^2(\Omega)\}$ for $\boldsymbol{u}$ and $\boldsymbol{v}_f$, with corresponding test functions $\boldsymbol{w}^p$ and $\boldsymbol{w}^v$, respectively, also in $H^{(div)}$, and the space $L^2(\Omega)$ for p_f with corresponding test function $\psi \in L^2(\Omega)$. Multiplying the equations with these test functions and integrating the second term on the left hand side of (3.3.13) by parts, the weak formulation for the fluid system is given by

$$\begin{aligned}(\boldsymbol{u}, \boldsymbol{w}^p)_\Omega - (p_f, \nabla \cdot \boldsymbol{w}^p)_\Omega - (\nabla \cdot (\lambda k \boldsymbol{u}), \psi)_\Omega &= (F_3, \psi)_\Omega - (p_f, \boldsymbol{w}^p \cdot \boldsymbol{n})_{\delta\Omega}, \\ (\boldsymbol{v}_f, \boldsymbol{w}^v)_\Omega = (\boldsymbol{v}_r, \boldsymbol{w}^v)_\Omega &- \left(\frac{\lambda k}{\phi}(\nabla p_f + \rho_f \hat{\boldsymbol{z}}), \boldsymbol{w}^v\right)_\Omega,\end{aligned} \tag{3.3.16}$$

where F_3 is the right hand side of (3.3.14), $\delta\Omega$ is the domain boundary, and $\boldsymbol{n}$ is its outward pointing normal.

Note that for the fluid pressure, the Dirichlet condition on the top boundary of the domain is applied into the weak form via the last term on the right hand side of the first equation of (3.3.16). The remaining boundary conditions will need to be strongly imposed, so that $\boldsymbol{u} \cdot \boldsymbol{n} = 0, \boldsymbol{w}^p \cdot \boldsymbol{n} = 0$ on the side boundaries and $\boldsymbol{u} \cdot \boldsymbol{n} = \rho_f, \boldsymbol{w}^p \cdot \boldsymbol{n} = 0$ on the bottom boundary. No conditions are needed for the fluid velocity in (3.3.15) as it is just an algebraic equation.

For the discretisation, following Brezzi and Fortin (1991), we choose to use Raviart-Thomas spaces of order ϱ for the pressure gradient $\boldsymbol{u}$ and discontinuous Galerkin elements of order ϱ for the fluid pressure, denoted by $RT(\varrho)$ and $DG(\varrho)$, respectively. We choose these spaces since they are said to be a stable finite element pair for this kind of problem. For a more detailed explanation on these function spaces and how they are appropriate for the Darcy-type problem, see Brezzi and Fortin (1991). For the fluid velocity problem, we use the usual Lagrangian space $Q^d_{h,\varrho+1}$.

Our discretised problem then reads: find $\{\boldsymbol{u}_h, p_{f_h}\} \in RT(\varrho) \times DG(\varrho)$ and $\boldsymbol{v}_{f_h} \in Q^d_{h,\varrho+1}$ such that

$$\begin{aligned}(\boldsymbol{u}_h, \boldsymbol{w}^p_h)_\Omega - (p_{f_h}, \nabla \cdot \boldsymbol{w}^p_h)_\Omega - (\nabla \cdot (\lambda k \boldsymbol{u}_h), \psi_h)_\Omega &= (F_3, \psi_h)_\Omega - (p_a, \boldsymbol{w}^p_h \cdot \boldsymbol{n})_{\delta\Omega_t}, \\ (\boldsymbol{v}_{f_h}, \boldsymbol{w}^v_h)_\Omega = (\boldsymbol{v}_{rh}, \boldsymbol{w}^v_h)_\Omega &- \left(\frac{\lambda k}{\phi_h}(\nabla p_{f_h} + \rho_f \hat{\boldsymbol{z}}), \boldsymbol{w}^v_h\right)_\Omega,\end{aligned} \tag{3.3.17}$$

for all $\{\boldsymbol{w}^p_h, \psi_h\} \in V_p = \{\{\boldsymbol{\varphi}, \psi\} \in RT(\varrho) \times DG(\varrho) : \boldsymbol{\varphi} \cdot \boldsymbol{n} \in L^2(\Omega)\}$ and $\boldsymbol{w}^v_h \in Q^d_{h,\varrho+1}$, where $\delta\Omega_t$ denotes the top boundary of the basin.

3.3.3 Discretisation of the porosity subsystem

For the porosity equation, we use a finite difference scheme for the time discretisation, and we discretise the spatial variables in the same way as we did for the rock and fluid subsystems. The porosity equation originally reads

$$\frac{\partial \phi}{\partial t} + \boldsymbol{v}_r \cdot \nabla \phi = -\phi_0 \Gamma \exp\left(-\Gamma(p_r - p_f)\right) \frac{D}{Dt}(p_r - p_f) - \Upsilon \frac{C(\phi)}{\mu_r}(p_r - p_f). \quad (3.3.18)$$

Suppose that a superscript n on a variable denotes the timestep number, such that, for example, $f^n = f(\boldsymbol{x}, t_n)$. Then we discretise the left hand side of (3.3.18) in the following way:

$$\frac{\partial \phi}{\partial t} + \boldsymbol{v}_r \cdot \nabla \phi \approx \frac{\phi^n - \phi^{n-1}}{t^n - t^{n-1}} + \boldsymbol{v}_r^{n-1} \cdot \nabla \phi^n. \quad (3.3.19)$$

For the right hand side of (3.3.18), we assume that for $t < t_2$ (as discussed in Section 2.1),

$$\frac{D}{Dt}(p_r - p_f) \approx 0. \quad (3.3.20)$$

Then we can discretise the time variable for (3.3.18) as

$$\begin{aligned} &\frac{\phi^n - \phi^{n-1}}{t^n - t^{n-1}} + \boldsymbol{v}_r^{n-1} \cdot \nabla \phi^n \\ &\approx \begin{cases} -\Upsilon \frac{C(\phi^{n-1})}{\mu_r(T^{n-1})}(p_r^{n-1} - p_f^{n-1}), & \text{for } n < 2, \\ -\phi_0 \Gamma \exp(-\Gamma(p_r^{n-1} - p_f^{n-1}))\left(\frac{p_r^{n-1} - p_r^{n-2}}{t^{n-1} - t^{n-2}} - \frac{p_f^{n-1} - p_f^{n-2}}{t^{n-1} - t^{n-2}}\right. & \\ \qquad \left. + \boldsymbol{v}_r^{n-1} \cdot \nabla(p_r^{n-1} - p_f^{n-1})\right) - \Upsilon \frac{C(\phi^{n-1})}{\mu_r(T^{n-1})}(p_r^{n-1} - p_f^{n-1}), & \text{for } n \geq 2. \end{cases} \end{aligned} \quad (3.3.21)$$

Note that the porosity equation is a hyperbolic PDE, which can be difficult to solve numerically and lead to numerical instabilities (Izadi, 2007). One method to avoid such instabilities is to use the streamline diffusion stabilisation method as we do here (see Tobiska and Verfürth (1996) for the analysis and further literature review of the streamline diffusion finite element method). For this, instead of the test function $\psi \in H_0^1(\Omega)$, we multiply by $\psi + \gamma \boldsymbol{v}_r \cdot \nabla \psi$, where we also have $\phi \in V = \{\varphi \in H^1(\Omega) \,\big|\, \varphi = \phi_0 \text{ on } z = h_0\}$. The stabilisation parameter, γ, is usually chosen to be of an order similar to that of the local mesh size h, and throughout our numerical verification, we take $\gamma = 0.1h$, as suggested in Bangerth et al. (2016), which is appropriate following the discussion on the choice of such stabilisation parameter in Section 2.4.3 by Donea and Huerta (2005).

With this, putting the equation into weak form and discretising, using the simplest function space of Lagrangian elements, we obtain the problem: find $\phi_h^n(\boldsymbol{x}) = \phi_h(\boldsymbol{x}, t^n) \in Q_{h,\varrho}$, such that

$$\begin{aligned}(\phi_h^n, \psi_h^n + \gamma \boldsymbol{v}_r^{n-1} \cdot \nabla \psi_h^n)_\Omega + \Delta t(\boldsymbol{v}_r^{n-1} \cdot \nabla \phi_h^n, \psi_h^n + \gamma \boldsymbol{v}_r^{n-1} \cdot \nabla \psi_h^n)_\Omega \\ = (\phi_h^{n-1}, \psi_h^n + \gamma \boldsymbol{v}_r^{n-1} \cdot \nabla \psi_h^n)_\Omega + \Delta t(G^{n-1}, \psi_h^n + \gamma \boldsymbol{v}_r^{n-1} \cdot \nabla \psi_h^n)_\Omega,\end{aligned} \tag{3.3.22}$$

for all $\psi_h^n \in Q_{h,\varrho}$, where G^{n-1} is the right hand side of (3.3.21) and where $\Delta t = t_n - t_{n-1}$. For the porosity equation, the value of ϕ is strongly imposed on the top boundary (our only inflow boundary where $\boldsymbol{v}_r \cdot \boldsymbol{n} < 0$).

3.3.4 Discretisation of the temperature subsystem

Recall the temperature equation, which can be written

$$\frac{\partial}{\partial t}((\phi \rho_f c_f + (1-\phi)\rho_r c_r)T) + \nabla \cdot ((\phi \rho_f c_f \boldsymbol{v}_f + (1-\phi)\rho_r c_r \boldsymbol{v}_r)T) - \frac{1}{\mathrm{Nu}} \nabla \cdot (\kappa_T \nabla T) = 0. \tag{3.3.23}$$

We discretise the temperature in time using a first-order implicit Euler scheme, and approximate T by $T^n(\boldsymbol{x})$ at time $t = t_n$. Then, discretising in time gives

$$\begin{aligned}(\phi^n \rho_f c_f + (1-\phi^n)\rho_r c_r)T^n - (\phi^{n-1}\rho_f c_f + (1-\phi^{n-1})\rho_r c_r)T^{n-1} \\ + \Delta t \, \nabla \cdot ((\phi^n \rho_f c_f \boldsymbol{v}_f^{n-1} + (1-\phi^n)\rho_r c_r \boldsymbol{v}_r^{n-1})T^n) - \frac{\Delta t}{\mathrm{Nu}} \nabla \cdot (\kappa_T \nabla T^n) = 0.\end{aligned} \tag{3.3.24}$$

Note that for the velocity, we approximate the value with the velocity found at time t_{n-1} rather than t_n. Similarly, the specific heat capacities take the temperature at $t = t_{n-1}$ as their inputs. The thermal conductivity, $\kappa_T(\phi)$, uses the current value of porosity.

We again discretise spatially with the same methodology as before. Multiplying (3.3.24) with a test function, $\psi \in H^1(\Omega)$, and integrating the last term on the left hand side by parts, the weak problem becomes: find $T \in H_t^1(\Omega) = \{\nu \in H^1(\Omega) \,\big|\, \nu|_{\delta\Omega_t} = 1\}$ such that

$$(\tilde{T}^n + \Delta t \hat{T}^n, \psi)_\Omega + \frac{\Delta t}{\mathrm{Nu}}(\kappa \nabla T^n, \nabla \psi)_\Omega = (\tilde{T}^{n-1}, \psi)_\Omega + \frac{\Delta t}{\mathrm{Nu}}(\kappa_T \nabla T^n \cdot \boldsymbol{n}, \psi)_{\delta\Omega_b}, \tag{3.3.25}$$

where

$$\tilde{T}^n = (\phi^n \rho_f c_f + (1-\phi^n)\rho_r c_r)T^n \tag{3.3.26}$$

and

$$\hat{T}^n = \nabla \cdot ((\phi^n \rho_f c_f \boldsymbol{v}_f^{n-1} + (1-\phi^n)\rho_r c_r \boldsymbol{v}_r^{n-1})T^n), \tag{3.3.27}$$

with $\psi \in H_0^1(\Omega) = \{\nu \in H^1(\Omega) \,\big|\, \nu|_{\delta\Omega_t} = 0\}$. Here, $\delta\Omega_t$ denotes the top boundary $z = h_N$ of the domain Ω where the Dirichlet condition need to be imposed strongly, and $\delta\Omega_b$ denotes the bottom boundary where the bottom boundary condition appears in the weak form. Note that the side boundary conditions are automatically satisfied as $\nabla T \cdot \boldsymbol{n} = 0$ on the sides.

Then, using simple Lagrangian finite elements for the temperature problem, we have the discretised problem: find $T_h^n(\boldsymbol{x}) = T_h(\boldsymbol{x}, t_n) \in Q_{h,\varrho}$, such that

$$(\tilde{T}_h^n + \Delta t \hat{T}_h^n, \psi_h)_\Omega + \frac{\Delta t}{\mathrm{Nu}}(\kappa_T \nabla T_h^n, \nabla \psi_h)_\Omega = (\tilde{T}_h^{n-1}, \psi_h) + \frac{\Delta t}{\mathrm{Nu}}(-q, \psi_h)_{\delta\Omega_b}, \quad (3.3.28)$$

where

$$\tilde{T}_h^n = (\phi_h^n \rho_f c_f + (1 - \phi_h^n)\rho_r c_r) T_h^n \quad (3.3.29)$$

and

$$\hat{T}_h^n = \nabla \cdot ((\phi_h^n \rho_f c_f \boldsymbol{v}_{fh}^{n-1} + (1 - \phi_h^n)\rho_r c_r \boldsymbol{v}_{rh}^{n-1}) T_h^n), \quad (3.3.30)$$

for all test functions $\psi_h \in H_0^1(\Omega) = \{\nu \in H^1(\Omega) \,\big|\, \nu|_{\delta\Omega_t} = 0\}$.

3.4 Solver construction and method of manufactured solutions

For the initial stages of verification, we use the method of manufactured solutions (MMS) to check that the solver for each separate subsystem is valid. We first need to choose such manufactured 'solutions'. We then substitute these analytical test solutions into our original problems and generate additional source terms to each PDE (if any). The boundary conditions are further modified if necessary so that the proposed solutions satisfy the whole problem including these conditions. We can then test our resulting numerical solutions against the initially proposed manufactured solutions for their validity. We do this by checking that the numerical solution converges to the true solution as the mesh size tends to zero. MMS is therefore a general procedure which is useful and widely employed in validating computational calculations. A lengthy discussion of the method and its applications can be found in (Roache, 1998).

3.5 Verification of solver

We proceed to the verification of each subsystem using MMS. During this process, let us assume that we have a fixed rectangular domain $\Omega = \{0 \leq x \leq \pi, 0 \leq z \leq 1\}$, and neglect sedimentation and any reconstruction of the domain. We verify each set of

equations as we proceed to solve them according to the sequence. Note that we test the whole system by using the solutions obtained from the previous subsystem MMS test as the input data for the next subsystem MMS test, where appropriate. We run the solver for each subsystem over four levels of grid refinement, where the first level of refinement corresponds to dividing the domain into 10 cells horizontally and 8 cells vertically, thereby having 80 cells in total. The grid is refined globally once between each refinement level, so that, when working in two dimensions, the total number of cells quadruples with each increasing refinement level.

We solve for our variables on these grids for two degrees of finite elements used, where degree 1 corresponds to the lowest degree for each respective finite dimensional spaces. Note that in general, for the velocities, we will use a polynomial degree of one more than our scalar variables. The polynomial degree for the pressure gradient remains the same as the fluid pressure since it is solved as a coupled system with each other. We carry out a convergence analysis by calculating the convergence rate of the numerical method which we define now.

3.5.1 Error analysis and convergence

To check that the numerical method is valid, we check that the error between an exact solution, u, and its numerical approximation, u_h, converges to zero, as the maximal mesh size h of the finite element grid is decreased. Let l denote the order of convergence for the numerical method, then if the method converges, we have that there exists a positive constant C (independent of the mesh size) such that

$$||u - u_h||_\Omega \leq Ch^l, \tag{3.5.1}$$

where h is sufficiently small.

Rearranging (3.5.1), we can calculate the order of convergence for our problem as $h \to 0$ since

$$\frac{||u - u_h||_\Omega}{||u - u_{\frac{h}{2}}||_\Omega} \approx \frac{Ch^l + \mathcal{O}(h^{l+1})}{C\left(\frac{h}{2}\right)^l + \mathcal{O}\left(\left(\frac{h}{2}\right)^{l+1}\right)} \approx 2^l + \mathcal{O}(h), \tag{3.5.2}$$

and therefore,

$$\log_2 \frac{||u - u_h||_\Omega}{||u - u_{\frac{h}{2}}||_\Omega} \approx l. \tag{3.5.3}$$

Here, we use $u_{\frac{h}{2}}$ to denote the numerical approximation to u with maximal mesh size $h/2$.

In general, we can check the convergence rate for our numerical method for each of our variables using (3.5.3). Note that throughout the error analysis we calculate

the global L_2 error between the exact and numerical solutions over the entire domain to obtain the norm $||u - u_h||_\Omega$, and in this case we expect that the convergence rate will be one more than the polynomial degree used for our finite elements.

3.5.2 Rock subsystem

To test the rock subsystem solver, assume $\alpha = 1$ and let us choose our manufactured 'solutions' to be

$$\boldsymbol{v}_r = \begin{pmatrix} 0 \\ -z^3 \end{pmatrix}, \qquad p_r = x^3(1-z), \tag{3.5.4}$$

with

$$\phi = \phi_0 + A\phi_0 tz, \qquad p_f = -x(z - \tfrac{1}{3}z^3), \qquad \boldsymbol{v}_f = \begin{pmatrix} x \\ z \end{pmatrix}, \qquad \tau_{ij} = 2\mu_r \dot{\varepsilon}_{ij}. \tag{3.5.5}$$

We also let μ_r, ρ_r, and ρ_f equal 1 for convenience, and $\phi_0 = 0.7, t = 0.5$, and $A = 0.1$.

We then solve for a modified set of rock equations (3.3.1) and (3.3.2), given by

$$\nabla \cdot ((1-\phi)\underline{\underline{\boldsymbol{\tau}}}(\boldsymbol{v}_r)) - \nabla((1-\phi)p_r) = \nabla(\phi p_f) + ((1-\phi)\rho_r + \phi\rho_f)\hat{\boldsymbol{z}} + \boldsymbol{F}_1, \tag{3.5.6}$$

$$\nabla \cdot ((1-\phi)\boldsymbol{v}_r) = -\nabla \cdot (\phi \boldsymbol{v}_f) + F_2, \tag{3.5.7}$$

where

$$\boldsymbol{F}_{1x} = -3x^2(1-\phi)(1-z) + \phi\left(z - \tfrac{1}{3}z^3\right), \tag{3.5.8}$$

$$\boldsymbol{F}_{1z} = -12z(1-\phi) + 6z^2\frac{\partial\phi}{\partial z} + x^3\left(1 - \phi + (1-z)\frac{\partial\phi}{\partial z}\right) + x(z - \tfrac{1}{3}z^3)\frac{\partial\phi}{\partial z} + x\phi(1-z^2) - (1-\phi)\rho_r - \phi\rho_f, \tag{3.5.9}$$

$$F_2 = -3z^2(1-\phi) + z^3\frac{\partial\phi}{\partial z} + 2\phi + z\frac{\partial\phi}{\partial z}, \tag{3.5.10}$$

with $\boldsymbol{F}_{1x}$ and $\boldsymbol{F}_{1z}$ denoting the $x-$ and $z-$components of the source vector $\boldsymbol{F}_1$, respectively. The variable definitions as chosen in (3.5.4) and (3.5.5) then satisfy (3.5.6) and (3.5.7), where the source terms have been calculated using the manufactured solutions. Note that the known solutions to (3.5.6) and (3.5.7) also satisfy the boundary conditions for the sides and the bottom of the basin, where with our manufactured solution, we have zero normal flux on the velocity at the three boundaries. The top boundary condition is satisfied if

$$\begin{aligned} -p_{\text{top}} &= \boldsymbol{n} \cdot (-p_r \boldsymbol{I} + \underline{\underline{\boldsymbol{\tau}}})\boldsymbol{n} \quad \text{on } z = z_{\text{top}} \\ &= -6z_{\text{top}}^2 - x^3(1 - z_{\text{top}}), \end{aligned} \tag{3.5.11}$$

where z_{top} is the $z-$coordinate along the top boundary.

After solving the modified equations (3.5.6) and (3.5.7) with the appropriate boundary conditions, we then obtain the numerical solution to the modified equations. We calculate the L_2 error between the numerical and manufactured solution on four successive refinement levels and for two different polynomial degrees in our problem. If the solver behaves correctly, we should see that the error between the numerical and manufactured solutions reduces appropriately with the mesh size. We show the global L_2 errors at each refinement level for the two degrees of finite elements for the rock pressure and rock velocity in Tables 3.1 and 3.2, respectively.

	FE degree=1		FE degree=2	
Refinement level	Error in p_r	Rate	Error in p_r	Rate
1	4.4092×10^{-2}	-	3.9535×10^{-4}	-
2	1.0977×10^{-2}	2.01	4.9315×10^{-5}	3.00
3	2.7415×10^{-3}	2.00	6.1620×10^{-6}	3.00
4	6.8518×10^{-4}	2.00	7.7022×10^{-7}	3.00

Table 3.1: Global L_2 errors and error convergence rates for the rock pressure, p_r, at different refinement levels and degrees of finite elements.

	FE degree=2		FE degree=3	
Refinement level	Error in $\boldsymbol{v}_r$	Rate	Error in $\boldsymbol{v}_r$	Rate
1	3.9164×10^{-2}	-	4.4709×10^{-6}	-
2	4.8956×10^{-3}	3.00	2.7770×10^{-7}	4.01
3	6.1196×10^{-4}	3.00	1.7290×10^{-8}	4.01
4	7.6496×10^{-5}	3.00	1.0791×10^{-9}	4.00

Table 3.2: Global L_2 errors and error convergence rates for the rock velocity, $\boldsymbol{v}_r$, at different refinement levels and degrees of finite elements.

We see that for the rock pressure, the convergence rate for the numerical method using finite elements with polynomial degree 1 is approximately equal to 2, as expected. For the rock pressure at a finite element degree of 2, a convergence rate of 3 is expected and this is what we observe. Similarly, the convergence rate for the rock velocity when finite elements of degree 2 are used is equal to the expected value of 3. Recall that for the rock velocity, we use finite element degrees that are one more than those used for the pressure, so 2 is the lowest degree we use for the rock velocity. When the degree of the rock velocity finite element is increased to 3, we find that the convergence rate is also around the expected value of 4. From the observed values of convergence rates

calculated from the L_2 errors between the numerical and manufactured solutions, we can conclude that the solver for the rock subequations works as expected.

3.5.3 Fluid subsystem

Suppose that

$$p_f = -x(z - \tfrac{1}{3}z^3), \tag{3.5.12}$$

$$\boldsymbol{u} = \begin{pmatrix} z - \frac{1}{3}z^3 \\ x(1 - z^2) \end{pmatrix}, \tag{3.5.13}$$

$$\boldsymbol{v}_f = \begin{pmatrix} \frac{\lambda k}{\phi}(z - \frac{1}{3}z^3) \\ -z^3 + \frac{\lambda k}{\phi}(x(1 - z^2) - \rho_f) \end{pmatrix}, \tag{3.5.14}$$

where we also let the rock velocity and porosity be as in (3.5.4) and (3.5.5) again. Then, the given choice for the fluid variables satisfy the system:

$$\boldsymbol{u} + \nabla p_f = \boldsymbol{0}, \tag{3.5.15}$$

$$-\nabla \cdot (\lambda k \boldsymbol{u}) = \nabla \cdot \boldsymbol{v}_r - \nabla \cdot (\lambda k \rho_f \hat{\boldsymbol{z}}) + 2\lambda k x z + 3z^2, \tag{3.5.16}$$

$$\boldsymbol{v}_f = \boldsymbol{v}_r - \frac{\lambda k}{\phi}(\nabla p_f + \rho_f \hat{\boldsymbol{z}}). \tag{3.5.17}$$

The value for p_f at the top boundary for the weakly imposed Dirichlet condition is calculated from (3.5.12), and the strongly imposed conditions for $-\boldsymbol{u} \cdot \boldsymbol{n}$ for the sides and bottom are calculated directly from (3.5.13). For convenience, we let λ, ρ_f, and k equal 1 in our numerical calculations. Recall that in this subsystem test, we input the numerical solutions for $\boldsymbol{v}_r$ we obtained in Section 3.5.2 in the right hand side of the above equations (3.5.15), (3.5.16), and (3.5.17), so that we are testing the validity of the whole system.

Tables 3.3, 3.4, and 3.5 below show the global errors in the L_2 norm between the exact and numerical solution for the fluid pressure, its negative gradient vector, and the fluid velocity. We use (3.5.3) to find the convergence rate.

	FE degree=1		FE degree=2	
Refinement level	Error in p_f	Rate	Error in p_f	Rate
1	1.2258×10^{-2}	-	4.9227×10^{-4}	-
2	3.0800×10^{-3}	1.99	6.1532×10^{-5}	3.00
3	7.7098×10^{-4}	2.00	7.6914×10^{-6}	3.00
4	1.9281×10^{-4}	2.00	9.6142×10^{-7}	3.00

Table 3.3: Global L_2 errors and error convergence rates for the fluid pressure, p_f, at different refinement levels and degrees of finite elements.

	FE degree=1		FE degree=2	
Refinement level	Error in $\boldsymbol{u}$	Rate	Error in $\boldsymbol{u}$	Rate
1	6.7575×10^{-3}	-	2.7139×10^{-4}	-
2	1.6981×10^{-3}	1.99	3.3924×10^{-5}	3.00
3	4.2506×10^{-4}	2.00	4.2405×10^{-6}	3.00
4	1.0630×10^{-4}	2.00	5.3006×10^{-7}	3.00

Table 3.4: Global L_2 errors and error convergence rates for the negative pressure gradient, $\boldsymbol{u}$, at different refinement levels and degrees of finite elements.

	FE degree=2		FE degree=3	
Refinement level	Error in $\boldsymbol{v}_f$	Rate	Error in $\boldsymbol{v}_f$	Rate
1	9.4100×10^{-3}	-	1.9659×10^{-4}	-
2	2.4053×10^{-3}	1.97	2.0896×10^{-5}	3.23
3	6.0578×10^{-4}	1.99	2.3475×10^{-6}	3.15
4	1.5176×10^{-4}	2.00	2.7541×10^{-7}	3.09

Table 3.5: Global L_2 errors and error convergence rates for the fluid velocity, $\boldsymbol{v}_f$, at different refinement levels and degrees of finite elements.

For the fluid pressure and the auxiliary function for its negative gradient, $\boldsymbol{u}$, recall that we use discontinuous Galerkin and Raviart-Thomas elements, respectively, with polynomial degrees of 1 and 2 for both variables. Therefore, we expect the convergence rate to be approximately equal to one more than the order of finite elements used for p_f and $\boldsymbol{u}$. Since we use Lagrangian elements of degree 2 and 3 for the fluid velocity (like the rock velocity), $\boldsymbol{v}_f$, we expect the convergence rate for the fluid velocity to be approximately 3 and 4, respectively.

We observe the expected convergence rate for the fluid pressure and its negative gradient, with convergence rates of 2 and 3 when finite elements or orders 1 and 2, respectively, are used. However, we see a lower convergence than expected for the fluid velocity. To understand this behaviour, let us recall the equation for fluid velocity, given by

$$\boldsymbol{v}_f = \boldsymbol{v}_r + \frac{\lambda k}{\phi}(\boldsymbol{u} - \rho_f \hat{\boldsymbol{z}}). \tag{3.5.18}$$

To solve this equation, we input the numerical solution of $\boldsymbol{u}$ we have found in the coupled equation for the fluid pressure and $\boldsymbol{u}$. Hence, we expect the order of the error between the exact and numerical solution of $\boldsymbol{u}$ to carry over into the calculation of $\boldsymbol{v}_f$. Hence, the convergence rate would be approximately equal to that of $\boldsymbol{u}$, which is

what we observe. Indeed, when the exact solution for the right hand side of the fluid velocity equation is used, we observe errors of orders much lower than those observed here. Hence, we can conclude that the numerical method with which we solve the fluid subsystem is valid.

3.5.4 Porosity subsystem

For the porosity subsystem, for convenience, let us consider a simplified version given by

$$\frac{\partial \phi}{\partial t} + \boldsymbol{v}_r \cdot \nabla \phi = 0, \tag{3.5.19}$$

and where we define

$$\boldsymbol{v}_r = \begin{pmatrix} x \\ z \end{pmatrix}. \tag{3.5.20}$$

Suppose we have a dummy solution given by

$$\phi = \phi_0 x^2 z^3 \sin(t), \tag{3.5.21}$$

which satisfies

$$\frac{\partial \phi}{\partial t} + \boldsymbol{v}_r \cdot \nabla \phi = F, \tag{3.5.22}$$

where

$$F = \phi_0 x^2 z^3 \cos(t) + 5\phi_0 x^2 z^3 \sin(t), \tag{3.5.23}$$

and the boundary and initial conditions calculated accordingly similar to the previous subsystems. We solve with the numerical method described previously, with $\phi_0 = 0.7$ as before. Since we discretise in both time and space, we present the convergence study in both time and space for the porosity subsystem.

3.5.4.1 Spatial convergence

If the solver behaves correctly, we expect the error between the numerical and exact solution to be of order $\mathcal{O}(\Delta t) + \mathcal{O}(h^{p+1})$, where Δt is the timestep size, h is the mesh size, and p is the order of finite element used. In order to show convergence of our numerical solution in space, we choose $\Delta t = 0.001$ so that $\mathcal{O}(\Delta t) < \mathcal{O}(h^{p+1})$ and the error arising from spatial discretisation dominates for most refinement levels tested (note that $h \approx 0.03$ at the highest refinement level we test).

Table 3.6 below shows the global errors in the L_2 norm between the exact and numerical solution at the tenth timestep for the porosity where we again use (3.5.3) to find the convergence rate.

	FE degree=1		FE degree=2	
Refinement level	Error in ϕ	Rate	Error in ϕ	Rate
1	5.6425×10^{-4}	-	2.5768×10^{-5}	-
2	1.4056×10^{-4}	2.01	3.2203×10^{-6}	3.00
3	3.5163×10^{-5}	2.00	3.9626×10^{-7}	3.02
4	8.8175×10^{-6}	2.00	5.8445×10^{-8}	2.76

Table 3.6: Global L_2 errors and error convergence rates for the porosity, ϕ, at different refinement levels and degrees of finite elements.

Like the other subsystems tested so far, we see a good convergence rate at both first and second finite element degrees, except between the third and fourth refinement levels when $p = 2$. This is likely due to the fact that $\mathcal{O}(\Delta t) > \mathcal{O}(h^{p+1})$ and therefore, the error arising from the discretisation in time affects the error convergence in space. Using $\Delta t = 0.0001$ and $p = 2$ to verify this claim, we have that the error is 5.8445×10^{-8} at the third refinement level and 5.38143×10^{-9} at the fourth refinement level, giving a convergence rate of 3.02. Hence, we can conclude that the slight drop in the convergence rate where the finite element degree equals 2 in Table 3.6 is due to the timestep size chosen, and not due to any potential problems with the solver.

3.5.4.2 Temporal convergence

We now test the temporal convergence of the porosity subsystem solver. For the correct solver behaviour, if we have $\mathcal{O}(\Delta t) > \mathcal{O}(h^{p+1})$ so that the total error is dominated by the error arising from the time discretisation, we expect the error between the numerical and exact solution to halve as Δt is halved.

We test the solver at the fifth refinement level and at the first finite element degree. The errors presented in Table 3.7 are calculated for the solutions at $t = 1$ for the solver using a timestep size of 0.5 which is continuously halved. We also display the convergence factor, which we define to be the calculated error with some timestep size divided by the error observed when half the timestep size is used. Hence, we expect the factor to be equal to approximately two as the timestep size is halved.

Δt	Error in ϕ	Factor
0.5	5.4575×10^{-2}	-
0.25	2.9769×10^{-2}	1.83
0.125	1.5584×10^{-2}	1.91
0.0625	7.9881×10^{-3}	1.95
0.03125	4.0577×10^{-3}	1.97

Table 3.7: Global L_2 errors and convergence factor for the porosity, ϕ at the fifth refinement level with finite element degree of one at $t = 1$.

We observe in Table 3.7 that as we reduce the timestep size by a factor of two, the error between the numerical solution and exact solution for ϕ also reduces by a factor of approximately two. Hence, we can conclude that the solver presents the expected convergent behaviour in both time and space.

3.5.5 Temperature subsystem

For the temperature subsystem, for convenience, we solve the following modified version for the verification:

$$\frac{\partial}{\partial t}((1-\phi)\rho_r c_r T) + \nabla\cdot((1-\phi)\rho_r c_r \boldsymbol{v}_r T) - \frac{1}{\mathrm{Nu}}\nabla\cdot(\kappa_T\nabla T) = F, \tag{3.5.24}$$

with F and boundary and initial conditions modified in such a way that

$$T = x^2 z^3 \sin t \tag{3.5.25}$$

with initial time $t = t_0 = 0$ solves the modified system. For convenience, we take Nu, κ_T, ρ_r, c_r, equal to 1.

In order to verify the solver using the method of manufactured solutions, we also assume that

$$\phi = z \tag{3.5.26}$$

and

$$\boldsymbol{v}_r = \begin{pmatrix} xz \\ xz \end{pmatrix}. \tag{3.5.27}$$

We also allow $T(t = 0) = 0$, and enforce Dirichlet boundary conditions on the top so that $T = x^2 \sin t$ on the top boundary, and flux conditions on the remaining boundaries, where $\nabla T \cdot \boldsymbol{n}$ is calculated using the dummy solution given in (3.5.25). Then taking

$$F = x^2z^3(1-z)\cos t - x^3z^4\sin t + (1-z)x^2z^3(3z+4x)\sin t - (6x^2z+2z^3)\sin t, \tag{3.5.28}$$

we have that (3.5.25) solves (3.5.24) with the modified initial and boundary conditions.

Like the porosity subsystem, we discretise in both time and space for the temperature equation. Hence, we present the convergence study in both time and space for the temperature subsystem.

3.5.5.1 Spatial convergence

For similar reasons as stated for the porosity subsystem solver verification, we let the timestep size $\Delta t = 0.001$, which is smaller than the mesh size for all our refinement levels. This is so that the errors due to the mesh size is the main contribution to the total numerical error. Table 3.8 shows the global errors in the L_2 norm between the manufactured exact solution and the numerical solution resulting from our solver at the tenth timestep for the temperature. We use (3.5.3) to calculate the convergence rate once again.

	FE degree=1		FE degree=2	
Refinement level	Error in T	Rate	Error in T	Rate
1	1.0604×10^{-3}	-	3.5549×10^{-5}	-
2	2.6258×10^{-4}	2.01	4.4939×10^{-6}	2.98
3	6.5516×10^{-5}	2.00	5.6406×10^{-7}	2.99
4	1.6366×10^{-5}	2.00	7.4865×10^{-8}	2.91

Table 3.8: Global L_2 errors and error convergence rates for the temperature, T, at different refinement levels and degrees of finite elements.

For both finite element degrees, we see the expected convergence rate with each successive refinement level. For problems using degree 1, we see a convergence rate of around 2, and for problems using degree 2, we see a convergence rate of around 3. Hence, we can conclude that our solver for the temperature subsystem behaves as expected with respect to the spatial convergence.

3.5.5.2 Temporal convergence

We now complete the verification of the solver by testing the temporal convergence. In order to examine the errors due to the discretisation with respect to time, we increase the timestep sizes to those that are larger than the mesh size, so that the temporal contribution to the error is more dominant. Similar to the porosity subsystem tests, we take four timesteps that successively halve, and calculate the errors at $t = 1$. The fifth refinement level is used throughout the temporal convergence test for the temperature.

Δt	Error in T	Factor
0.5	5.4855×10^{-3}	-
0.25	2.9164×10^{-3}	1.88
0.125	1.4647×10^{-3}	1.99
0.0625	7.3381×10^{-4}	2.00

Table 3.9: Global L_2 errors and convergence factor for the porosity, T at the highest refinement level with finite element degree of one at $t = 1$.

We find that as the timestep size halves, the error between the manufactured analytical solution and the numerical solution also halves. This is the expected behaviour if the solver was to behave correctly. Hence, based on the convergence study both spatially and temporally, we can conclude that our solver for the temperature equation behaves as expected and produces a good approximation to the solution.

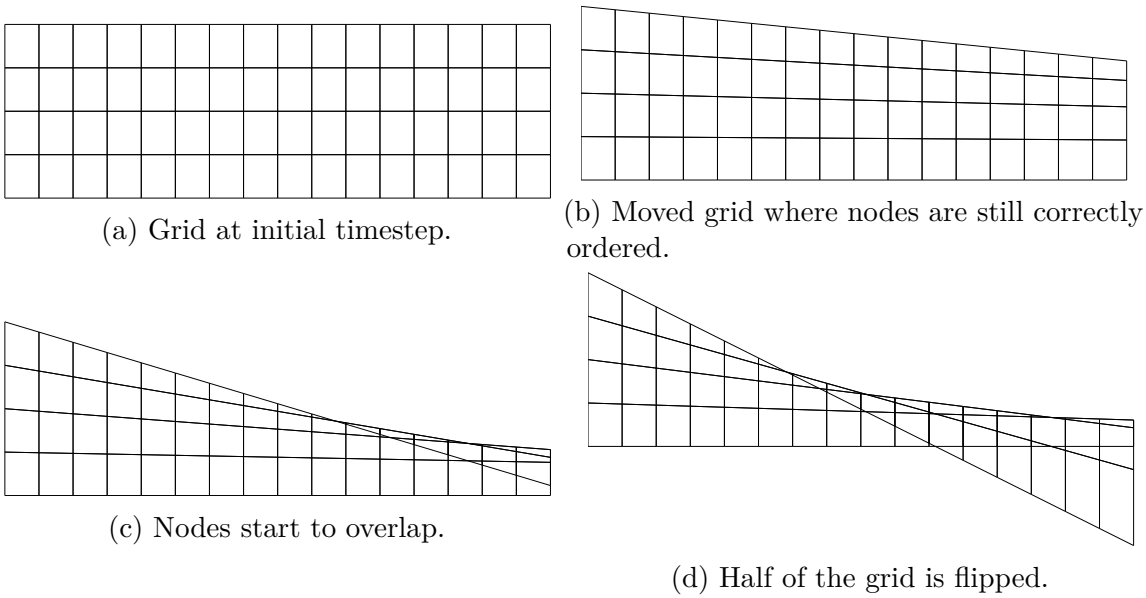
3.6 Compacting domain

Now that we have verified the solver for each subsystem, we discuss the implementation of the moving boundary to complete the overview of our initial solver development. Still assuming that the bottom boundary is fixed so that the only moving boundary is the top boundary of the basin, recall that the top boundary moves with the rock velocity (plus the sedimentation rate if there is deposition, which we ignore for now and discuss in Section 3.7).

The domain is moved after solving the subsystems at each timestep according to the velocity of the rock. To apply this feature, we move each vertex point in our finite element mesh according to the displacement, by using the discretisation of the definition of velocity ($\frac{d\boldsymbol{x}}{dt} = \boldsymbol{v}_r$). Hence, this is calculated by multiplying the rock velocity with the timestep at each point, such that

$$\boldsymbol{x}_h \to \boldsymbol{x}_h + \Delta t \boldsymbol{v}_r(\boldsymbol{x}_h). \tag{3.6.1}$$

The nodal points in the mesh are moved in this way after all six variables are solved for at each timestep. This method is similar to that used by Lee et al. (2015) in which they apply this method to a range of well-known one-dimensional free boundary problems. Note that after we move the mesh after each timestep, we interpolate the old solution onto the new nodes via an automatic function in `deal.ii` in order to solve the porosity and temperature at the next timestep (refer to the discretised time-stepping scheme as shown in (3.3.21) and (3.3.24)). For a more detailed review on



(a) Grid at initial timestep.

(b) Moved grid where nodes are still correctly ordered.

(c) Nodes start to overlap.

(d) Half of the grid is flipped.

Figure 3.5: We show a succession of grids where the timestep taken is too large and the displacement of some nodes moves it in a non-physical way.

this particular method we use, see Lee et al. (2015), and for alternative velocity-based methods with which to move the mesh, see Baines et al. (2011).

Note that although the method gives us the correct grid movement we want, we must take care when shifting the nodes within the domain as it is possible to obtain a mesh which is topologically incorrect. For example, suppose that our timestep is so large such that the magnitude of the second term on the right hand side of (3.6.1) (the displacement) is greater than the difference between one node and the displaced neighbouring node. Then, once the mesh is moved, the ordering of the nodes is not conserved if some elements in the finite element mesh results with a negative volume. This would occur if the displacement of one node moves it to below the coordinate of the node which it was originally above. Figure 3.5 shows a grid where half the grid has been 'flipped' because of such a situation.

In order to make sure that our solver prevents this, we must devise a further technique. Whilst `deal.ii` throws an exception in the running of the program and terminates if such grid distortion occurs, we want to be able to automatically resolve the problem by using adaptive mesh adjustments. To do this, we find the location of the element with the negative volume (this is automatically done as `deal.ii` throws the exception) and find the size of the displacement which distorted the mesh. We allow the solver to then move the mesh using a coarser grid then refining again before solving the subsystems at the next step. We can now resolve the situation if mesh

distortion was to occur.

3.7 Sedimentation

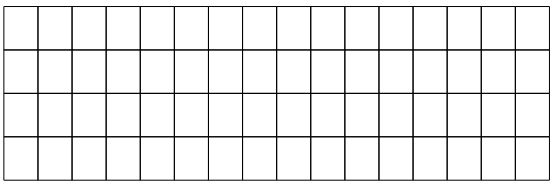
We now discuss how we may incorporate sedimentation into our solver. Suppose that at some time after the compaction of some rock type has occurred, a layer of new sediments is deposited on the top boundary. We numerically model it such that we create a new layer in our grid after solving for each variable and moving the mesh. We do this after we have compacted the domain with respect to the rock velocity as discussed in the previous section.

For the new layer, we simply create a new triangulation where the vertices of its bottom boundary are identical to the vertices of the top boundary of the compacted domain. This is so that the boundaries of each triangulation line up perfectly at the point of contact. Then, onto each vertex of the new grid, we add the depositional height and join the vertices up appropriately.

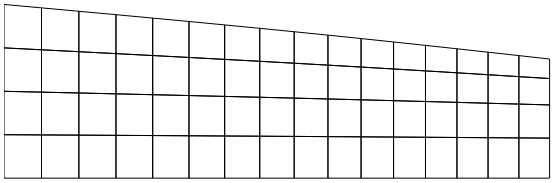
Note that in `deal.ii`, we are able to merge triangulations together easily. However, the triangulations must be at the coarsest refinement level, and therefore we must strip all refinements on both grids. Once the two coarse grids are merged, we can then refine globally before we continue to solve our problem. We present the steps to incorporate the new depositional layer visually in Figure 3.6.

Note that there are a few more aspects of the problem we need to take into account as we create the grid with the extra sedimentary layer. First, as we create the deposited layer, we interpolate the rock and fluid velocities and pressures with the values of the corresponding profiles at the top boundary of the existing mesh on the entire new depositing grid (Figure 3.6b). The surface porosity and surface temperature (as per our boundary conditions) are also interpolated over the entire depositional grid so that both profiles are constant in the newly depositing layer before we solve the problem. This makes up our 'old' solution for the new merged domain.

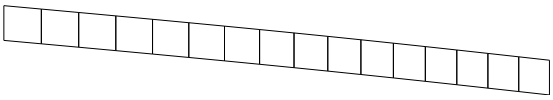
Further, we need to interpolate the old solution of the old discretisation we obtained on the grid in Figure 3.6b onto the new grid with sedimentation, since even the nodes within the old boundaries of the domain will have moved. For this, we interpolate the old solution onto the new merged mesh along with the interpolating solution in the depositional layer as described above, rather than the coarsened mesh. This is for the sake of accuracy. We also need to redefine our degrees of freedom associated with the new vertices of the refined merged mesh before we attempt to solve the system on the new triangulation.



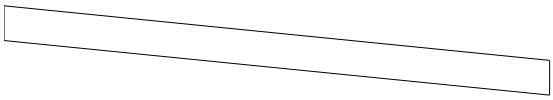
(a) Initial grid after refining.



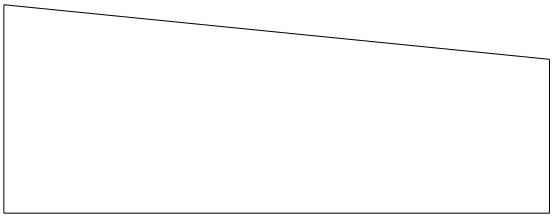
(b) Moved mesh after solving on initial grid after a few timesteps.



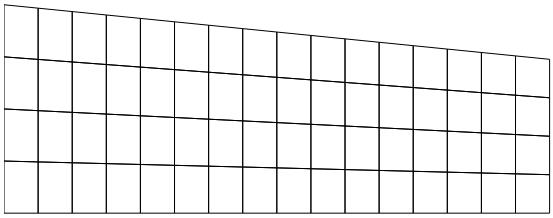
(c) Deposited layer is created taking the top coordinates of the grid in Figure 3.6b and adding the depositional height.



(d) Deposited layer is coarsened.



(e) Deposited layer added to coarsened version of the solved grid in Figure 3.6b.



(f) Refined grid with sedimentation after compaction.

Figure 3.6: A step-by-step presentation of the method we use to incorporate sedimentation.

We must also be mindful that the boundary conditions of our problem are now applied at the newly formed boundaries of the merged grid. This is taken care of automatically in the solver by reassigning boundary identifiers on the merged triangulation.

3.8 Summary of Chapter 3

In this chapter, we presented the numerical solution method which one may use to solve the model (2.4.4–2.4.9). To do this, we initially split our system of equations and boundary and initial conditions derived in Chapter 2 into smaller subsystems which are easier to solve separately. By solving and coupling the subsystems together, we can solve for the six dependent variables in an iterative manner. We discussed the `deal.ii` library with which we solve each subsystem, and also the finite element method.

We used the method of manufactured solutions to test the validity of our solvers. Modifying the system of equations and conditions in an appropriate way, we proceeded to measure the numerical error between the test solutions and their numerical approximations obtained by the solvers. Having carried out the error analysis by calculating the convergence rates for each subsystem, we can conclude that the numerical method is valid since the errors for each subsystem converge at the expected rates.

Finally, we outlined the method with which we include compaction and sedimentation. Compaction is simulated by moving the nodal points in the mesh with the rock velocity found. In order to include sedimentation, we manipulate the basin domain and numerically model the process. We do this by stripping the existing grid of its triangulation and adding a layer exactly above it, and re-triangulating before solving again.

Now that we have faith that our solvers provide a good approximation to our derived system, our industrial partners can use them as base solvers onto which they may easily incorporate more complex geological phenomena and features. We next move on to using our solvers to study the behaviour of the solutions to our model (2.4.4–2.4.9).

Chapter 4

Simulation results using the full solver

Recall that in Chapter 2, we derived a dimensionless model for the rock and fluid velocities and pressures, the porosity, and the temperature (2.4.4–2.4.9). In Chapter 3, the model was divided into four subsystems which we solve in succession in order to couple the inter-dependent variables. In this chapter, we present the results of the full solver in the simplest geological cases and compare them for different parameters and scenarios. The simulation results will provide PDS with a good insight into the effects of varying parameters on a basic complete model.

4.1 Solver parameters

For our simulation results, we solve the dimensionless discretised system of equations as outlined in Chapter 3. The base solver is applied to an initial dimensionless domain which we define to be $\Omega = \{0 \leq x \leq 20, 0 \leq z \leq 10\}$. Note that this is equivalent to 20 kilometres and 10 kilometres for the x- and z-axes, respectively, in the dimensional form.

4.1.1 Definition of parameters

For all simulations throughout the base solver simulations, we use the data for the rock and fluid as given in Tables 4.1 and 4.2. These have been obtained from Senior et al. (2016) and are based on empirical properties of shale. Note that all parameters are dimensionless unless otherwise stated.

Parameter	Value
ρ_r	2.71
c_r	1.0
$\kappa_{T\text{rock}}$	3
ϕ_0	0.7
θ	0.5

Table 4.1: Table of shale parameter values (dimensionless) used for our simulations. All values in this table are sourced from Senior et al. (2016).

Parameter	Value
ρ_f	1.0
c_f	4.0
$\kappa_{T\text{fluid}}$	0.6
q	10
E	400
R	4.6
p_a	1.0

Table 4.2: Table of fluid and other parameter values used for our simulations. All values in this table are sourced from Senior et al. (2016).

Parameter	Value	Units
d	10^3	m
g	10^1	$\mathrm{m\,s^{-2}}$
k_0	$\frac{1}{3} \times 10^{-17}$	$\mathrm{m^2}$
μ_f	10^{-3}	$\mathrm{kg\,m^{-1}\,s^{-1}}$
c_0	10^3	$\mathrm{m^2\,s^{-2}\,{}^\circ C^{-1}}$
χ	7.27×10^{-8}	$\mathrm{m\,s^2\,kg^{-1}}$
H_0	$\frac{1}{3} \times 10^{-10}$	$\mathrm{m\,s^{-1}}$
ρ_0	10^3	$\mathrm{kg\,m^{-3}}$
κ_{T0}	10^0	$\mathrm{kg\,m\,s^{-3}\,{}^\circ C^{-1}}$
μ_{r0}	10^{20}	$\mathrm{kg\,m^{-1}\,s^{-1}}$
T_0	10^0	$^\circ\mathrm{C}$

Table 4.3: Table of parameters used in nondimensionalisation. The value for the rock viscosity parameter was chosen after discussions with Senior et al. (2016) based on the range taken from Gerya (2010), and all other values are sourced from Senior et al. (2016).

Note that with our choice of d and H_0 as in Table 4.3, our time scales like

$\frac{d}{H_0} = 3 \times 10^{13}$ seconds, which corresponds to approximately one million years (m.a.), which is a reasonable geological timescale for our model.

With the nondimensionalisation values as given in Table 4.3 and the definition of our dimensionless numbers given in Table 2.2, we then obtain the values of dimensionless numbers which are defined in Table 4.4. These values are used for our equations as described in Section 3.1.2 throughout this chapter unless otherwise stated.

Dimensionless parameter	Value
λ	1
α	$\frac{1}{3}$
Γ	0.727×10^{-1}
Re	$\frac{1}{3} \times 10^{-24}$
Ri	9×10^{24}
Υ	3
Pr	10^{23}
Nu	$\frac{1}{3} \times 10^{-1}$

Table 4.4: Table of values of the dimensionless parameters used.

Note that using our rock and fluid parameters, we find that the Reynolds and Richardson numbers are very small and very large, respectively. The Prandtl number is also very large. However, this does not present any issues in our system as they only appear in combinations with each other. In our compaction equation, we have the Reynolds and Richardson numbers appearing together as a product in the form of the chemical compaction number, $\Upsilon = \mathrm{ReRi}$, which is $\mathcal{O}(1)$, and in our temperature equation, the numbers appear via the Nusselt number $\mathrm{Nu} = \mathrm{PrRe}$, which is $\mathcal{O}(10^{-1})$.

For each simulation, we use an initial grid where the domain Ω is divided into 5120 cells, unless otherwise stated. The timestep is set at 0.1, which means that 10 timesteps are required to produce results over approximately one million years. Note that initially, we ran the simulations with this timestep on grids from two times coarser than what we use here, as well as three consecutive levels finer. We found that this level of refinement was sufficient to present suitable results, without compromising computational time (at the highest levels tested, our simulation took weeks to process). We did not find any instabilities in our results, and any seeming occurrences were small and at values of almost zero. Hence, we chose a domain of 5120 cells as our appropriate refinement level for the presentation of our results.

We now assume that there is a kilometre of water present at the top of the basin, giving $p_{\mathrm{top}} \approx 1$, for all time. The fluid pressure is assumed to be slightly larger than

hydrostatic initially where the pressure increases linearly with depth such that,

$$p_f|_{t=0} = p_a + \beta(h_{N0} - z), \tag{4.1.1}$$

where $\beta = 1.3$ is a suitable value for this parameter (Senior et al., 2016). The fluid is also assumed to be instantaneously expelled from the domain at values estimated empirically (Senior et al., 2016). These conditions for the fluid correspond to the instantaneous behaviour as the rock matrix, which is at surface porosity, begins to compact.

4.2 Base results

For the simulation results, we use the material parameters as in Section 4.1, with a constant permeability where $\lambda, k = 1$. Since sedimentation is a relatively immediate process compared to compaction, we deposit a layer 1km in height at every million years (rather than at every timestep) for $t > 0$, where our timestep is 0.1 million years. Recall that we move the mesh with respect to the rock velocity, and this is done immediately after solving for all profiles at each timestep, and before sedimentation at every million years. The results for the rock and fluid velocities and pressures, the porosity, and temperature at $t = 5$ (equivalently after five million years) are given in Figure 4.1.

The first observation is that our solutions mostly display vertical behaviour (in the z-direction only). The horizontal velocities for both fluid and rock are almost zero (or at least small enough that any seeming x-dependence is not important), and the remaining solutions vary significantly in the vertical direction but depend weakly on x. This agrees with the results found in most literature, which state that compaction is in general a vertical process. Further, this is expected from our boundary conditions, where we imposed zero-flux of rock and fluid across the side boundaries, and all other boundary conditions were independent of the horizontal direction.

We observe that the fluid pressure is less than that of the rock pressure, which is to be expected. Further, the rock has a negative vertical velocity which would move the domain downwards, as expected when compaction takes place. The fluid, on the other hand, is found to move upwards, which is also to be expected since the fluid will be expelled from the basin with compaction. The porosity is lower at the bottom of the basin than the top which is at surface porosity, and this is consistent with our results for the rock and fluid pressures. Lastly, the temperature has a fairly steady gradient, with the top of the basin resting at surface temperature.

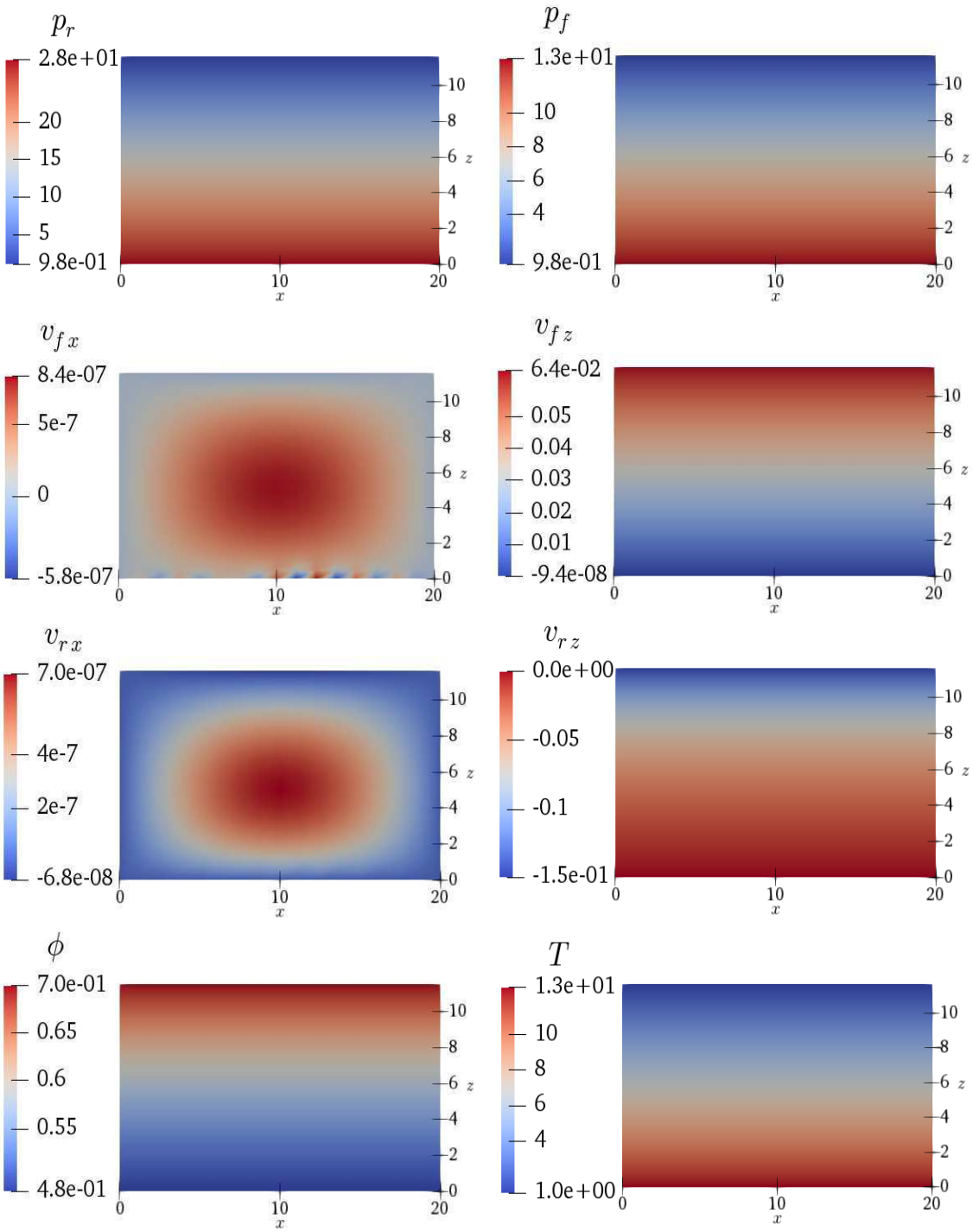


Figure 4.1: 2D solutions for all variables after approximately 5 million years (i.e., at $t = 5$). Note that the subscripts x, z denote the x-, z-components of the velocities, respectively.

4.3 Three-dimensional results

We stated in Chapters 2 and 3 that our model and respective solver are built in a way that allows the user to extend the model and solver to a three-dimensional problem. For the model, the system of equations remains the same in three dimensions (adjusting each vector to contain a second lateral dimension and altering the gravitational constant vector appropriately), and the boundary conditions in the new y-direction are the same as that in the x-direction. For the solver, changing the dimension of the problem is as easy as setting the input of the dimension of the problem from two to three, since we have written it to allow for this extension as efficiently as possible. We briefly present the results for a three-dimensional extension of the results found in Section 4.2.

The results for the pressures, velocities, porosity, and temperature are presented in Figure 4.2. Note that height is still in the z-direction, and the x-y axes make up the horizontal plane in the basin. For these simulation results, we used a much coarser mesh than the one used in the simulation in Section 4.2, since extending the model to three dimensions greatly increased the number of degrees of freedom in the numerical problem. For the three-dimensional problem, we used half the number of nodes in both the x- and z-directions that were used in Section 4.2, and the number of finite element nodes used in the y-direction is equal to the number used in the x-direction.

From Figure 4.2, we find that our three-dimensional solver works well and presents the same behaviour in the vertical direction for all variables when compared to those seen in the previous section. In fact, the cross-sections of our results in three dimensions appear to be identical to the two-dimensional results, which is to be expected since the model has no dependence in the y-direction. We have shown that our model and solver are easily able to model three-dimensional behaviour for sedimentary basins, as required by the user. However, for the remainder of the thesis, we choose to use the model in two dimensions only.

4.4 Results neglecting sedimentation

We now consider a compacting domain in the absence of any sedimentation. Recall from Chapter 1 that deposition is sometimes neglected in industrial simulations. In this case, note that the domain moves with the rock velocity only. Hence, on $\frac{d\boldsymbol{x}}{dt} = \boldsymbol{v}_r$, we can use

$$\frac{\partial \phi}{\partial t} = -\phi_0 \Gamma \exp\left(-\Gamma(p_r - p_f)\right) \frac{\partial}{\partial t}(p_r - p_f) - \Upsilon \frac{C(\phi)}{\mu_r}(p_r - p_f) \tag{4.4.1}$$

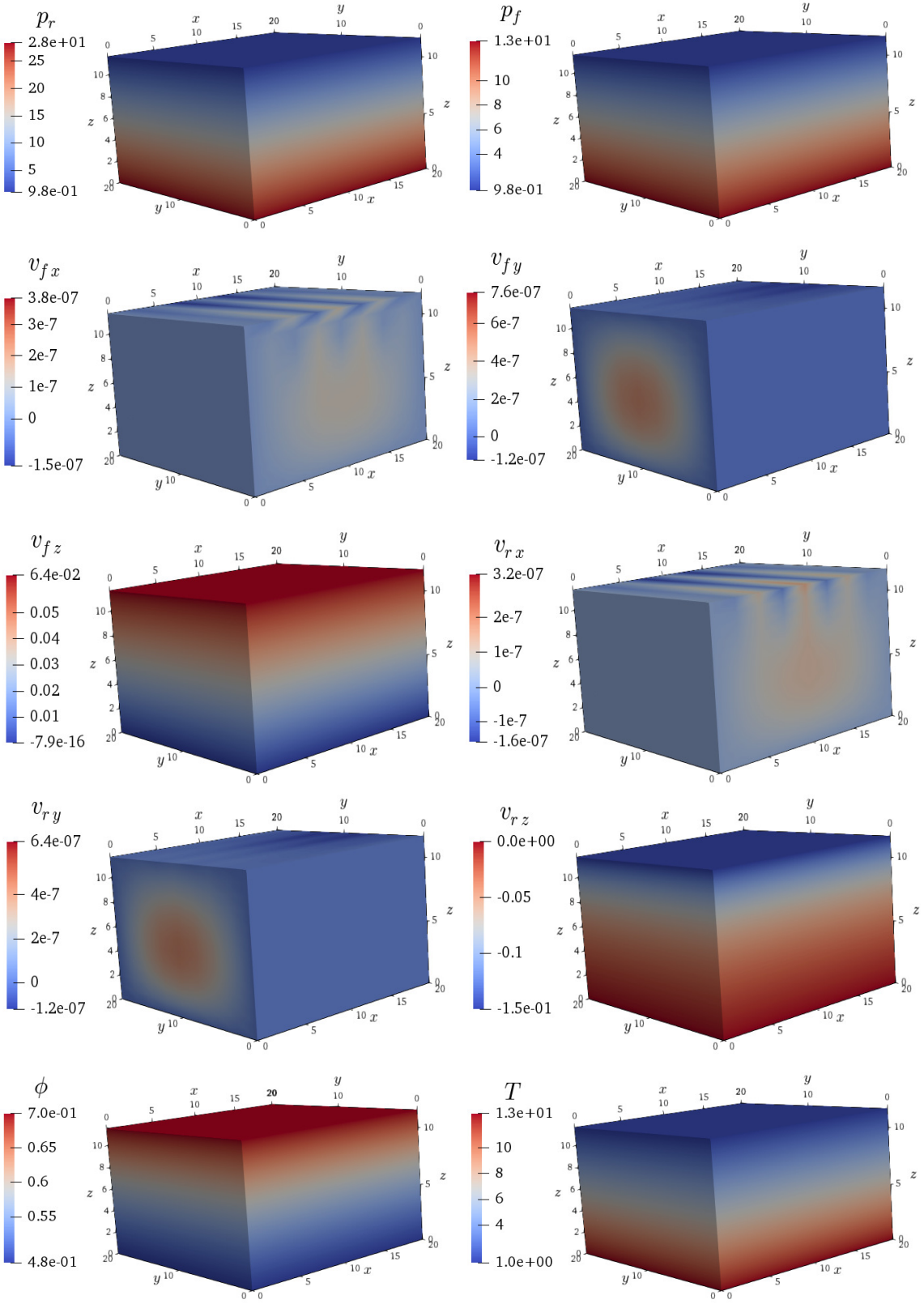


Figure 4.2: 3D solutions for the pressures, porosity, and temperature after approximately 5 million years.

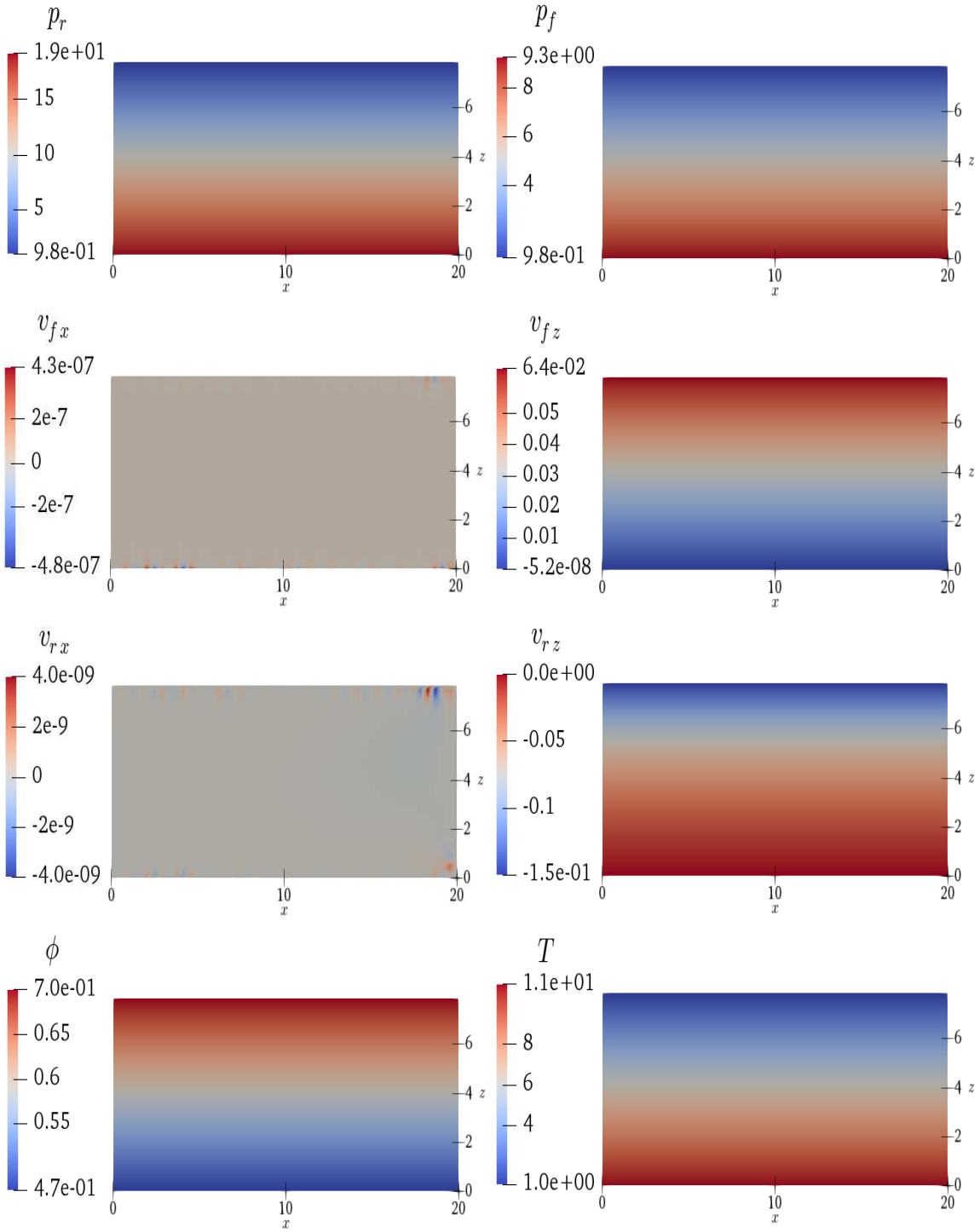


Figure 4.3: 2D solutions for all variables after approximately 10 million years (i.e., at $t = 10$) with sedimentation neglected. $\lambda = 1$. Note that the subscripts x, z denote the x-, z-components of the velocities, respectively. The height z of the basin is measured up from the bottom of each rectangular region, and x is in the lateral direction.

as our porosity equation.

The results for the rock and fluid velocities and pressures, the porosity, and temperature after ten million years are given in Figure 4.3. Note that we again use a constant permeability model, with $\lambda, k = 1$.

4.4.1 Comparison to results with sedimentation

We find that in general, the qualitative behaviours of the resulting profiles for the pressures, velocities, porosity, and temperature when sedimentation takes place are similar to when it is neglected. The profiles in both cases show mostly vertical behaviours, and there is no particular quality in any of the profiles that differs largely between the two cases. We find that in the case where sedimentation is neglected, it takes ten million years rather than five million years with sedimentation for the porosity profile to become similar. We comment on more specific differences between the case where there is sedimentation and where there is no sedimentation by comparing the respective porosity profiles directly.

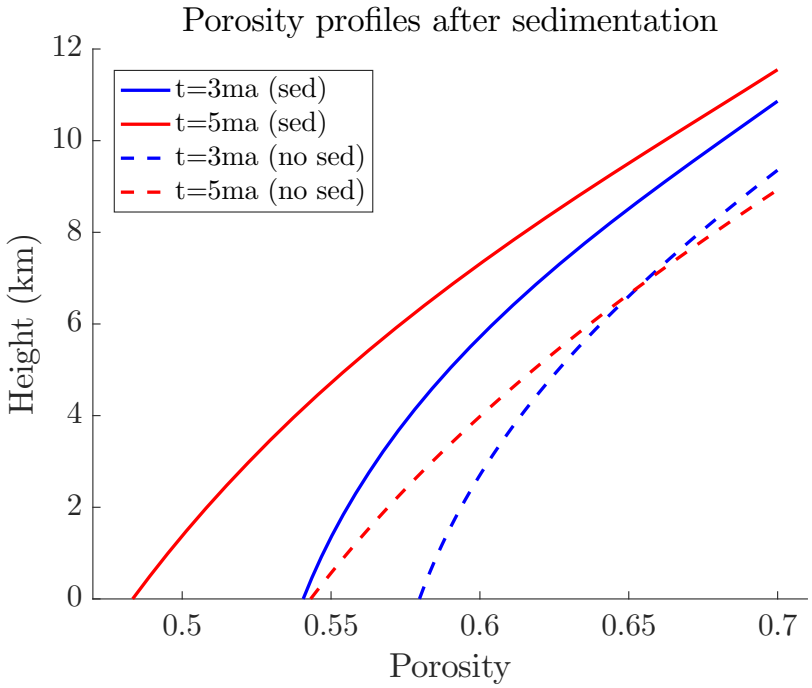


Figure 4.4: The porosity profiles (when $x = 10$) after three and five million years when the basin is subject to both compaction and sedimentation, and just compaction.

In Figure 4.4, we present the porosity profiles at $t = 3$ and $t = 5$, which correspond to after three and five million years in time, respectively, for the case incorporating sedimentation with solid lines, and the case using just compaction and no sedimentation

in the dashed lines. Since the behaviour of our variables are mostly in the z-direction, we have taken the values for our variables in the middle of our basin where $x = 10$ for our results. This is for convenience and for a clearer analysis and comparison.

The first obvious observation is that with 1km of sediments being deposited every millionth year, the basin grows in height. This is to be expected since without sedimentation using the same parameters, the basin compacted less than 1km each year. The main difference we see between the profiles with and without sedimentation as seen in Figure 4.4 is the relatively large difference in porosity at the bottom of the basin towards $z = 0$ at these times (recall that it takes ten million years without sedimentation for the porosity profile to be similar to that with sedimentation after five million years). We find that when there is sedimentation, the basin compacts more within the same amount of time, as seen by the lower values of porosity for the solid lines (with sedimentation) than the dashed lines (without sedimentation). This is to be expected since with sedimentation, there is more weight on top of the basin every million years. Therefore, we expect the pressures at the bottom of the basin to be larger than previously, and the bottom of the basin undergoes a more significant decrease in porosity with time. We also find that with sedimentation, the profiles are slightly less linear than without sedimentation, especially towards the bottom of the basin. In our case, this means that the bottom of the basin compacts slightly more than previously with sedimentation. These qualitative observations are to be expected given the extra overlying weight caused by extra rock on the top of the basin.

The simulations with sedimentation have resulted in greater compaction with higher pressures at the bottom of the basin. However, the qualitative behaviours for all profiles are similar to before. The sedimentation process alone therefore does not change the general evolution of the basin compared to not having any deposition. Hence, for the remainder of this thesis, we neglect sedimentation. However, we have presented the method with which one can incorporate sedimentation into our solver if necessary for completeness.

4.5 Constant permeability models

We noted in Chapter 2 that permeability values can range over eight orders of magnitude depending on the rock type. For shale, the values of k_0 ranges from (in order of magnitude) 10^{-16} to 10^{-20} (Neuzil, 1994). Therefore, we then examine the effects of different values of λ (for a constant k model) on our solution profiles by comparing the results seen from the simulations.

Thus far, we used $\lambda = 1$ in our base simulation results. This is equivalent to using $k_0 = \frac{1}{3} \times 10^{-17}$ in our Darcy equations for the subsystem which read

$$\boldsymbol{u} + \nabla p_f = \mathbf{0}, \tag{4.5.1}$$

$$-\nabla \cdot (\lambda k \boldsymbol{u}) = \nabla \cdot \boldsymbol{v}_r - \nabla \cdot (\lambda k \rho_f \hat{\boldsymbol{z}}), \tag{4.5.2}$$

$$\boldsymbol{v}_f = \boldsymbol{v}_r - \frac{\lambda k}{\phi}(\nabla p_f + \rho_f \hat{\boldsymbol{z}}). \tag{4.5.3}$$

4.5.1 Comparison between results for different values of λ

Letting our permeability scale k_0 range from $\frac{1}{3} \times 10^{-16}$ to $\frac{1}{3} \times 10^{-20}$, the values for λ for shale in our model range from 0.001 to 10. Note also that since

$$\lambda = \frac{k_0 \rho_0 g}{\mu_f H_0}, \tag{4.5.4}$$

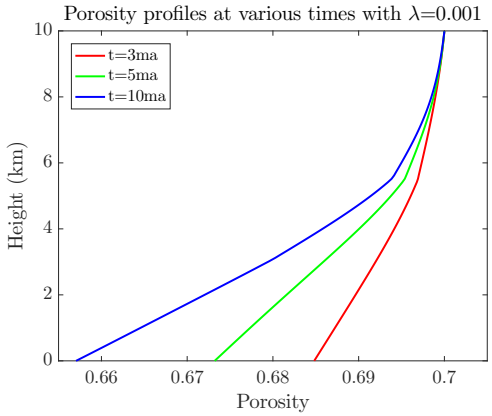
where H_0 is the sedimentation rate, large λ may correspond to low sedimentation rate or high permeability, and small λ may correspond to high sedimentation rate or low permeability.

Keeping our permeability model constant with respect to porosity so that $k = 1$, we briefly outline the expected behaviour of the pore pressure and porosity within the basin for different values of k_0 and therefore λ. For very permeable rock (with large permeability), we expect the fluid to be able to escape the porous domain with relative ease. If a rock has a very small permeability, the pore fluid may not be expelled as easily and therefore would result in a larger pressure build up. This, in turn, would cause the rock to be compacted with much more difficulty than if it were more permeable.

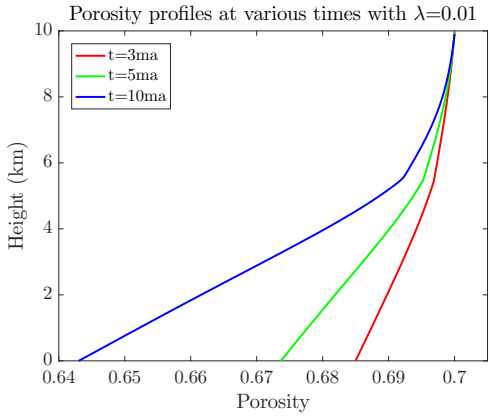
For these simulations, all parameter values other than λ are the same as the case for $\lambda = 1$ in the previous section (with no deposition). In this section, four more values of λ are tested (0.001, 0.01, 0.1, and 10) and we compare the results for the porosity and fluid pressure after three, five, and ten million years. We again take the values in the middle of our basin where $x = 10$ for our results.

4.5.1.1 Porosity

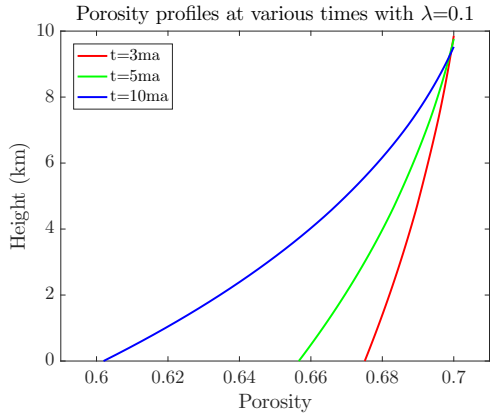
Figure 4.5 shows the porosity profiles at different times for different values of λ. We comment on the small sedimentation number case first, where $\lambda = 0.001$ (Figure 4.5a). We observe that the domain has a larger value of ϕ after ten million years compared to other profiles, and therefore has compacted less. This is to be expected as discussed previously, with the fluid not being able to escape as freely and therefore the basin



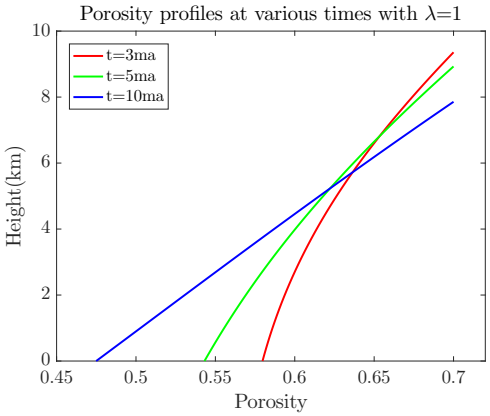
(a) $\lambda = 0.001$



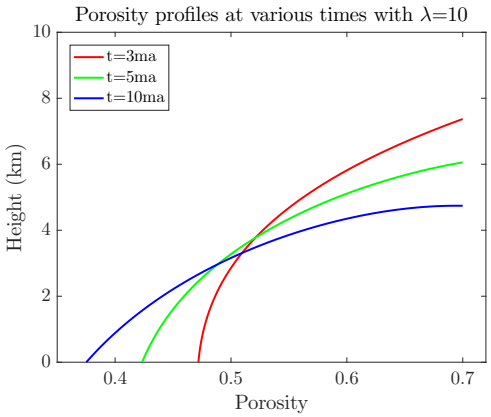
(b) $\lambda = 0.01$



(c) $\lambda = 0.1$



(d) $\lambda = 1$



(e) $\lambda = 10$

Figure 4.5: Porosity profiles for $\lambda = 0.001, 0.01, 0.1, 1, 10$ after three, five, and ten million years.

unable to compact as much. Further, we see that the basin has compacted more towards the bottom of the basin, and towards the top half of the basin, the porosity remains close to the surface porosity value of 0.7 even after 10 million years.

We see a little more compaction for the case where $\lambda = 0.01$ (Figure 4.5b), and the difference between this and the case where $\lambda = 0.001$ is particularly noticeable after about five million years. Prior to the five million year mark, we see that the porosity profiles differ only by a small amount. For a clearer and direct comparison between these two cases (since the differences are small), see Figure 4.6. The qualitative behaviour is similar to the previous case, where compaction is seen mostly towards the bottom of the basin and the top end of the basin remain around the surface porosity.

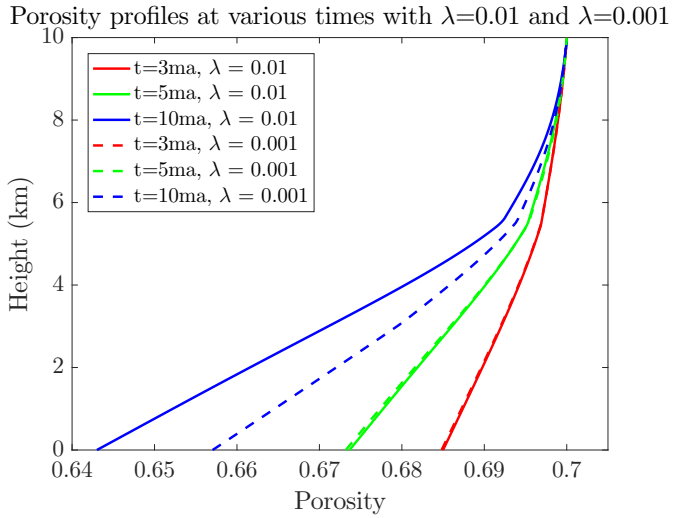


Figure 4.6: Direct comparison for the porosity profiles using $\lambda = 0.01$ and $\lambda = 0.001$ for various times to show the small differences between the two cases.

A further reduction is seen when $\lambda = 0.1$ (Figure 4.5c), or equivalently, as the permeability becomes larger. There is a more homogeneous gradient of compaction and a good amount of compaction can be seen throughout the whole basin. The porosity reduction seems more steady with continuously more compaction seen towards the bottom of the domain.

Where $\lambda = 1$ (Figure 4.5d), we begin to see qualitatively different behaviour in the porosity profile than previously. When the permeabilities were smaller, we observed more compaction at the bottom and little compaction towards the top of the basin. However, in this case, we have almost a linear compaction profile after ten million years and a significant reduction in porosity overall. This agrees with what we had expected since a larger permeability of the rock corresponds to a quicker rate of compaction.

Finally, we observe significant changes to the porosity profiles over time when $\lambda = 10$ as shown in Figure 4.5e. Contrary to the behaviour presented when small values of λ are used, we see that when $\lambda = 10$, compaction has taken place more towards the top of the basin than the bottom and the reduction is more steady towards the bottom of the basin.

Figure 4.7 shows the porosity profiles using the five different values of λ after ten million years on the same scale. The qualitative differences in the profiles can clearly be seen, with the smaller values of λ presenting a 'flatter' porosity profile, with $\lambda = 1$ presenting an almost linear profile, and the largest value presenting a convex profile where compaction is most significant at the top of the basin.

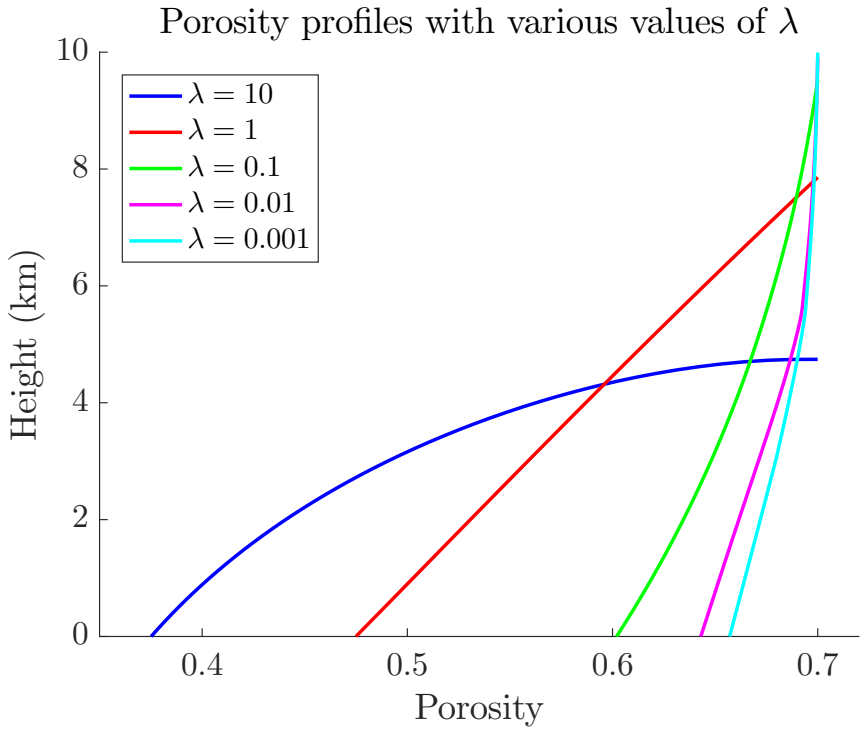


Figure 4.7: Porosity profiles after ten million years using five different values of λ.

We now present the same results for the pore pressure for different values of the sedimentation number before we summarise our observations.

4.5.1.2 Pore fluid pressure

The pore pressure results for different values of λ are shown in Figure 4.8. The values of the pore pressure are taken at $t = 0$ to show the pressure profiles before compaction has taken place. The pressure values are again taken at the point where $x = 10$.

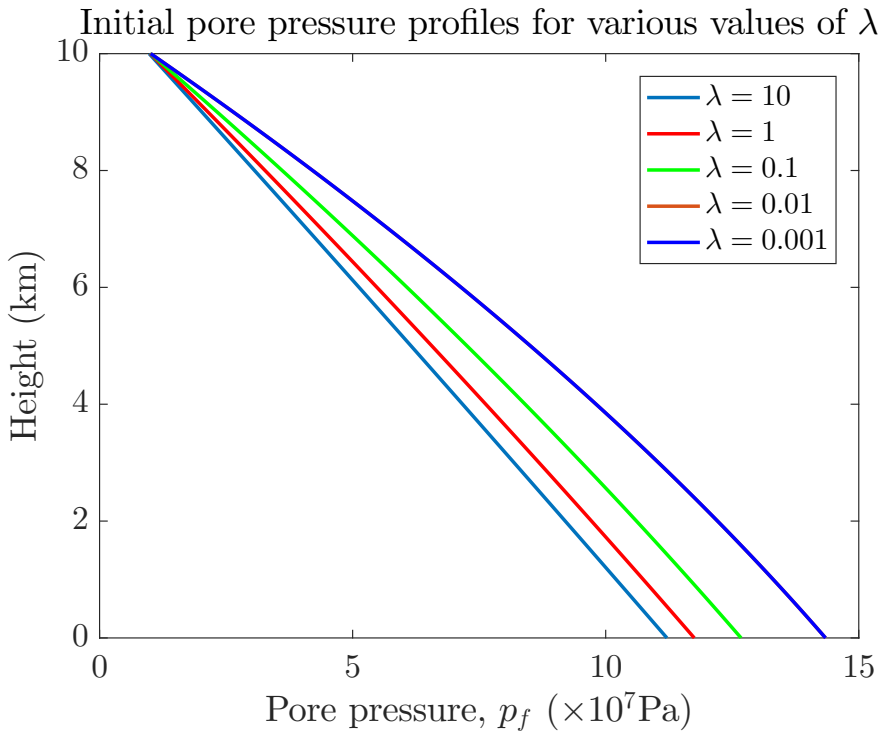


Figure 4.8: Pore pressure results before compaction for five different values of λ.

First, note in Figure 4.8 that hidden behind the dark blue line, which corresponds to the case where $\lambda = 0.001$, there is an orange line which corresponds to the case where $\lambda = 0.01$, and the difference between the two is almost negligible. The case where $\lambda = 0.01$ results in pore pressure values that are approximately $\mathcal{O}(10^{-2})$ smaller than when $\lambda = 0.001$ is used. As λ increases, we observe that the pore pressure becomes almost hydrostatic and presents almost no pressure build up as $\lambda \to 10$. The results we see are as expected — as λ increases, the pore pressure decreases.

4.5.2 Summary of results using constant permeability

In this section, we presented the solutions for the porosity and pore pressure for various values of the dimensionless sedimentation number, λ. We assumed the permeability to be constant with respect to porosity and examined the effects of different values of λ for a basin consisting of shale-like materials.

Recalling that

$$\lambda = \frac{k_0 \rho_0 g}{\mu_f H_0}, \tag{4.5.5}$$

using smaller values of λ is equivalent to having low permeability or large sedimentation rate and large values of λ corresponds to having high permeability or low sedimentation

rate. Physically, we expect the pore fluid to be able to escape the basin with less ease if the permeability is low, and therefore compaction is a more difficult process. On the other hand, if the permeability is large and the pore fluid can therefore be expelled from the domain with ease, we expect more compaction to take place.

These expected results are what we find for our various values of λ used (see Figures 4.5 and 4.7). For small values, we see that in ten million years, the basin has only reached a minimum porosity of around 0.65, whilst the basin reaches porosities down to around 0.375 when λ is large. Further, for values of $\lambda \ll 1$, we see that the porosity profiles do not differ much from each other, and that significant changes in the porosity are seen when λ is equal to 1 or higher.

More interestingly, we see that the value of λ affects the qualitative behaviour of the porosity. For smaller values of λ, we see that the porosity remains near ϕ_0 towards the top of the basin, and compaction is relatively significant towards the bottom. The porosity profile becomes more linear as λ increases, and eventually, for large λ, we see that the porosity reduces more towards the top of the basin rather than the bottom.

Let us discuss this in a more physical setting. If the permeability is low, it is more difficult for the fluid to escape and there is a larger build up of pressure in general (as also seen in the pore pressure results in Figure 4.8) than when the permeability is high. Further, if the sedimentation rate is high, such that the materials are being deposited faster than the basin is allowed to compact, we would expect the bottom of the domain to compact more than the top as the top of the domain is not able to accommodate the sudden flow of fluid being expelled from the domain. This is indeed what we find.

On the other hand, if the permeability is high, it is easier for the fluid to escape so we experience fast compaction. Alternatively, if the sedimentation rate is low, we would expect the basin to be able to compact more evenly and steadily, which is again what we find. Note that the qualitative behaviour of our porosity profiles for various values of λ agrees with the results found in literature. For example, Audet and Fowler (1992) use the same definition of λ for a 1D simplified model for the pore pressure and porosity only and find similar qualitative behaviours for large and small values of λ.

4.6 Porosity-dependent permeability model

In general, the permeability depends largely on the porosity of the rock and we have thus far shown that a few orders of magnitude of change in the permeability can affect the resulting profiles within the basin. It is therefore unrealistic to use a constant permeability, which is a simplification found in most literature. Therefore, we now use a Kozeny-Carman type permeability-porosity model as discussed in Chapter 2 and discuss whether it is indeed necessary to use a varying permeability model. We will use the general Kozeny-Carman form where $b = 0$ (refer to Section 2.3.2.1), and write

$$k(\phi) = k_0 \left(\frac{\phi}{\phi_0} \right)^a, \tag{4.6.1}$$

as also used by Yang (1999) and Fowler and Yang (1998), where a can vary depending on the lithology we model in each simulation. Since we use the parameters for shale, ϕ_0 still equals 0.7. We let the exponent in (4.6.1) be $a = 8$ which is appropriate for shale following Smith (1971) and Angevine and Turcotte (1983).

To analyse the behaviour resulting from a varying permeability model, we compare our results for a shale-like rock to that obtained when we let k take a constant value for all time throughout the domain. We test the effects of a porosity-dependent permeability model against the previously obtained profiles of $\lambda = 1$ and $k = 1$. Note that we expect k to vary between $\mathcal{O}(1)$ and $\mathcal{O}(10^{-2})$ given the values of ϕ found.

We present the results for the porosity taken at $x = 10$ after five million and ten million years, and these are shown in Figure 4.9. All other parameters are as defined in Section 4.1, including $k_0 = 10^{-17}$ for both cases.

We have found a distinctive kind of behaviour when a varying permeability model is used. The basin appears to have compacted more towards the top of the basin than the bottom, which is the qualitative behaviour seen for large λ. Further, when a varying permeability has been used, the basin has compacted more towards the top of the basin than the case where $\lambda = 1, k = 1$, even though the value of λk in the varying permeability model cannot exceed 1. However, towards the bottom of the basin, we see that the porosity reduction is much less significant than in the case where $\lambda, k = 1$.

Note also that the bottom of the basin for the varying permeability case has not compacted much after the five million year mark, where the porosity remains close to 0.55 whilst both other cases have presented a significant porosity reduction. This is because as the porosity is reduced, k is reduced and the porosity reduces at a slower rate and this is what we see at the bottom of the basin.

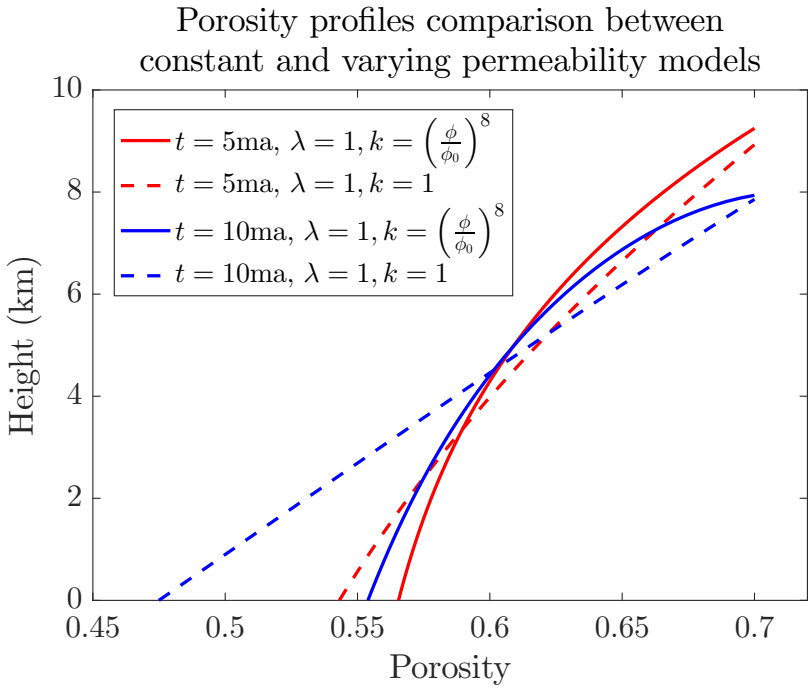


Figure 4.9: Porosity results after five and ten million years using a varying permeability model.

Now let us consider the top of the basin. The basin has compacted more than the case for $\lambda, k = 1$, and this is likely due to the bottom of the basin not being able to accommodate the compaction process since it is no longer as permeable. Hence, the top of the domain, where the rock is still relatively more permeable, experiences the compaction.

It is clear from the results in Figure 4.9 that using a varying permeability model has a significant effect on the qualitative behaviour of the porosity. We can conclude from the results that, in general, a varying permeability model is required to produce more realistic results. However, a constant permeability model may still be appropriate when very thin layers are considered and therefore the porosity values throughout the basin are within a small range.

4.7 Different compaction mechanisms

In this section we briefly present the results for the porosity profiles in a compacting basin under either mechanical or chemical compaction. Figure 4.10 shows the porosity results when the basin is subject to only mechanical or chemical compaction. The parameters remain the same as previously, with $\lambda, k = 1$.

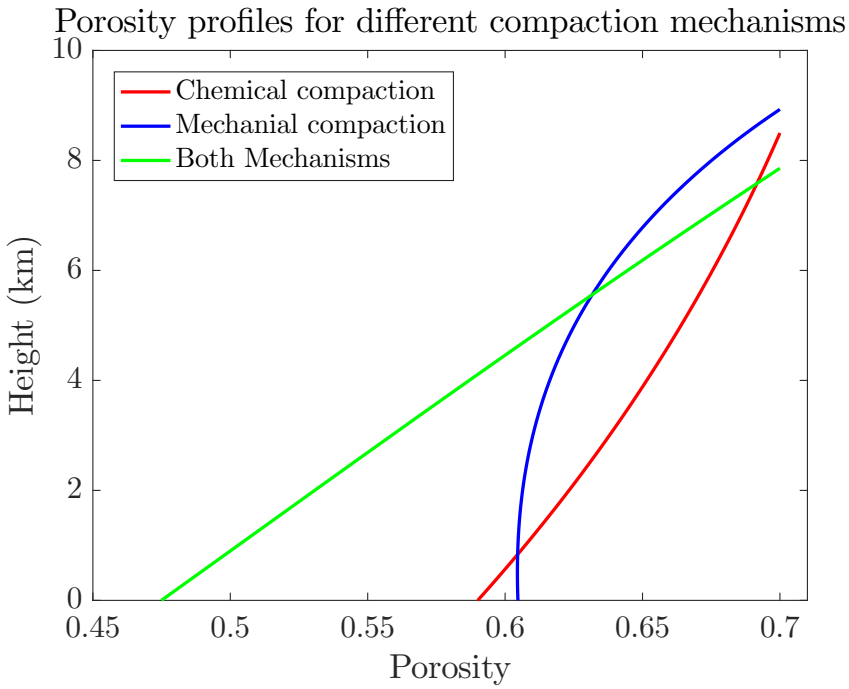


Figure 4.10: Comparison between the porosity profiles using different values of μ_{r0} after ten million years.

From the graphs in Figure 4.10, we can see that the qualitative behaviours of the porosity under the two compaction mechanisms are different. Chemical compaction, which is modelled as

$$\frac{\partial \phi_{\text{chem}}}{\partial t} = -\Upsilon \frac{C(\phi)}{\mu_r}(p_r - p_f), \tag{4.7.1}$$

seems to be a more linear process than overburden compaction. In the case where mechanical compaction, modelled as

$$\frac{\partial \phi_{\text{mech}}}{\partial t} = -\phi_0 \Gamma \exp\left(-\Gamma(p_r - p_f)\right) \frac{\partial}{\partial t}(p_r - p_f), \tag{4.7.2}$$

is the only contribution towards the porosity loss, we see that, with the parameters used, the basin has compacted faster towards the bottom of the basin than the top.

Recall our porosity profile for the case where $\lambda, k = 1$ and where both mechanical and chemical compaction terms were included in the compaction equation, shown in green in Figure 4.10. After ten million years, we found the porosity followed an approximately linear profile. From the results in this section, we can conclude that incorporating both mechanical and chemical contributions to the compaction presents significantly different results than when only one of the two mechanisms are modelled.

Further, with the parameters used (which are based on empirical values (Senior et al., 2016)), we see that chemical compaction is not negligible and should be included

in the model. Including the chemical compaction as well as mechanical compaction in the model provides further insight into the effects of mechanisms other than overlying loading. Hence, we conclude that whilst many authors neglect the chemical compaction term in the porosity model, it is crucial to include both the mechanical and chemical compaction terms in a model for compaction in sedimentary basins.

4.8 The viscosity effect

The viscosity of the rock is also neglected in most models found in literature, but we model the rock here as a highly viscous fluid, where the viscosity scaling μ_{r0} is large. In our model, the viscosity is explicitly incorporated in two different equations. First, the viscosity term is seen in one of the rock equations, which in its dimensionless subsystem form reads

$$\alpha\nabla\cdot((1-\phi)\underline{\underline{\boldsymbol{\tau}}}(\boldsymbol{v}_r))-\nabla((1-\phi)p_r)=\nabla(\phi p_f)+((1-\phi)\rho_r+\phi\rho_f)\hat{\boldsymbol{z}}, \tag{4.8.1}$$

via the stress tensor and therefore the viscosity scale appears in the strain rate number α defined by

$$\alpha=\frac{\mu_{r0}H_0}{\rho_0 g d^2}. \tag{4.8.2}$$

It is also included in our compaction equation, which in the dimensionless form and a frame moving with the rock velocity reads

$$\frac{\partial\phi}{\partial t}=-\phi_0\Gamma\exp\left(-\Gamma(p_r-p_f)\right)\frac{\partial}{\partial t}(p_r-p_f)-\Upsilon\frac{C(\phi)}{\mu_r}(p_r-p_f), \tag{4.8.3}$$

and therefore the viscosity scale appears within the chemical compaction term with

$$\Upsilon=\frac{\rho_0 g d^2}{\mu_{r0}H_0}. \tag{4.8.4}$$

The change in viscosity as compaction occurs is not widely known. However, we know that the sediments under pressure and compaction becomes more viscous as they begin to cement into solid rock over time. Hence, we can assume that the viscosity will increase with time and decreasing porosity. On the other hand, if the basement of the basin lies close to the mantle (the underlying crust is very thin), then the excess temperature can reduce the viscosity of the domain.

We therefore test the sensitivity of the results to the change in viscosity for some values of μ_{r0}, and for convenience we keep all the parameters as before with $\lambda, k = 1$. Additionally, we neglect mechanical compaction for this test, so that the compaction

is modelled by the following equation (using the partial derivative again as we move the mesh with respect to the rock velocity):

$$\frac{\partial \phi}{\partial t} = -\Upsilon \frac{C(\phi)}{\mu_r}(p_r - p_f). \tag{4.8.5}$$

Note further that the heat flux value q at the bottom of the basins is kept constant throughout all tests. We test four cases where $\mu_{r0} = 0.5 \times 10^{20}, 1 \times 10^{20}, 0.5 \times 10^{21}$, and 1×10^{21} kg m^{-1} s^{-1} and present the resulting porosity profiles in the basin after ten million years. The porosity profiles displayed in Figure 4.11 are taken where $x = 10$ in the basin, since our solutions are still mostly independent of the x-direction.

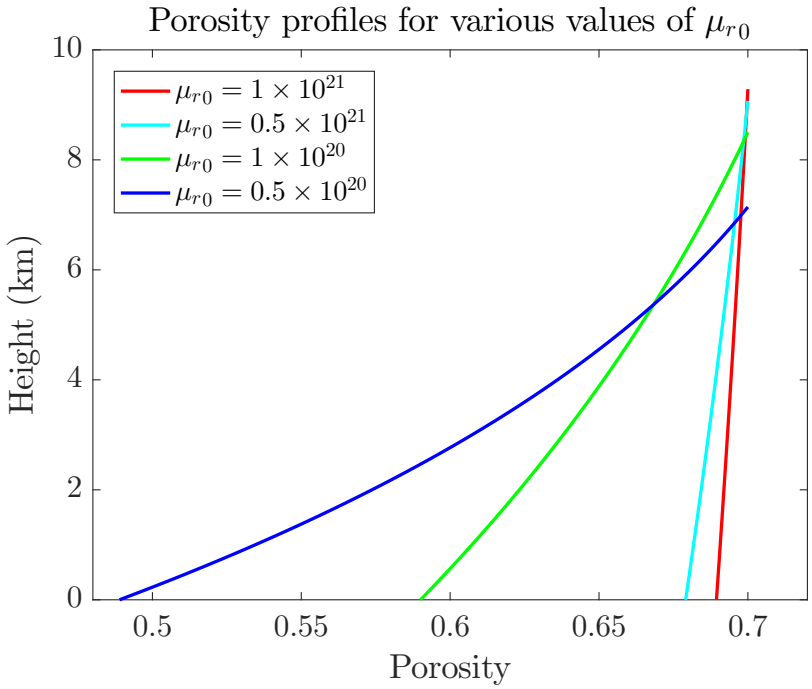


Figure 4.11: Comparison between the porosity profiles after ten million years using different values of the viscosity scaling parameter μ_{r0} with corresponding unit kg m^{-1} s^{-1}.

We see from Figure 4.11 that changing the value of the dimensionless scaling of the rock viscosity has a significant effect on the basin compaction. For $\mu_{r0} \sim \mathcal{O}(10^{21})$ kg m^{-1} s^{-1}, we have very little compaction and the porosity values we see are even smaller than those obtained when small values of λ are used (which corresponds to using a small permeability or high sedimentation rate — see Figure 4.7).

For μ_{r0} equal to or smaller than 1×10^{20} kg m^{-1} s^{-1}, we see that we have a significant drop in the porosity compared to when larger values are used. We can deduce from Figure 4.11 that for values of viscosity larger than $\mu_{r0} = 0.5 \times 10^{21}$ kg m^{-1} s^{-1}, the

porosity loss will be almost negligible. However, there are significant changes to the porosity profiles when values less than $\mu_{r0} = 0.5 \times 10^{21}\,\mathrm{kg\,m^{-1}\,s^{-1}}$ are used, and compaction becomes more sensitive to the changes in viscosity. We believe that the results are particularly affected by the changing viscosity in the chemical compaction term, rather than in our stress tensor. It is clear from the form of the equations that the rate of change of porosity is directly affected by the reciprocal of the rock viscosity. We do not further test the validity of this claim, but in any case, we have found that the viscosity affects the compaction behaviour significantly.

4.9 Different effective stress models

One of the major additions to our model compared to those found in literature is the calculation of the rock pressure. In particular, we choose to model the 'effective stress' as the difference between the rock and fluid pressure, rather than the difference between the lithostatic pressure and fluid pressure. With our choice of effective stress, we are able to incorporate both the vertical effective stress (which is mostly used in literature and represents pressure only due to overlying weight) as well as other contributions resulting from interphasial and viscous forces.

There are also other effective stress models which we believe we can use. Let us rewrite our compaction equation in terms of some effective stress, $\bar{p}$. Then the porosity equation for a moving mesh reads

$$\frac{\partial \phi}{\partial t} = -\phi_0 \Gamma \exp\left(-\Gamma \bar{p}\right) \frac{\partial \bar{p}}{\partial t} - \Upsilon \, \frac{C(\phi)}{\mu_r} \bar{p}, \tag{4.9.1}$$

where until now, $\bar{p} = p_r - p_f$ in our model and most authors in literature use $\bar{p} = p_L - p_f$, where $p_L(x) = \int_0^{h_N} (1-\phi)\rho_r + \phi\rho_f \, dz$.

Let us also consider two other effective stress models which may be used. First, consider

$$\begin{aligned} \bar{p} &= ((1-\phi)p_r + \phi p_f) - p_f \\ &= (1-\phi)(p_r - p_f). \end{aligned} \tag{4.9.2}$$

This effective stress model is driven by assuming that compaction is dependent of the difference between the pore pressure and the phase-averaged pressure surrounding it. Consider a small volume of pore fluid. The surrounding forces can be thought to depend on the pressure exerted by both fluid and rock phases, rather than just the rock. Hence, we arrive at the model given in (4.9.2).

Alternatively, consider the original discussion in Chapter 2, where we mentioned that chemical compaction can be thought to be a local process on the microscopic scale, whereas mechanical compaction takes places on a larger basin-wide scale. Hence, we may consider modifying the compaction equation to

$$\frac{\partial \phi}{\partial t} = -\phi_0 \Gamma \exp\left(-\Gamma(p_L - p_f)\right) \frac{\partial}{\partial t}(p_L - p_f) - \Upsilon \frac{C(\phi)}{\mu_r}(p_r - p_f). \tag{4.9.3}$$

In this modified equation (4.9.3) where we use mixed models for $\bar{p}$, the mechanical compaction component (first term on the right hand side) depends on the difference between the lithostatic pressure and the fluid pressure, thereby modelling mechanical compaction as simply the overlying weight. The second term on the right hand side of (4.9.3) remains a function of the rock pressure and fluid pressure, thereby considering the chemical compaction process to be a relatively local mechanism.

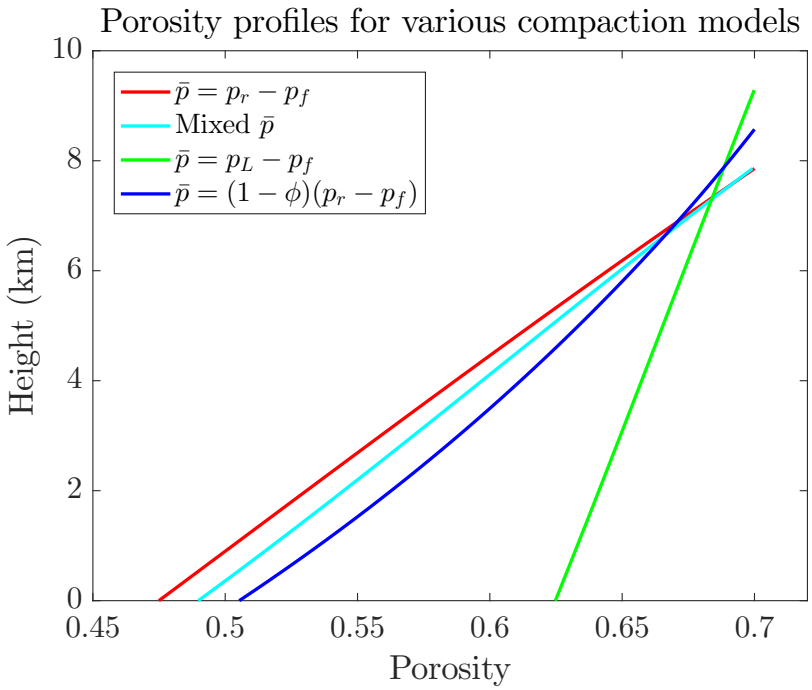


Figure 4.12: Comparison between the porosity profiles using different models for the effective stress.

It is difficult to deduce correctly which of the models discussed here is the most suitable, since laboratory experiments will never be able to test or replicate the correct behaviour of basins millions of years ago. However, we can at least test their qualitative behaviours on compaction here. In Figure 4.12, we compare the different compaction models discussed using the four different effective stress models. The same parameters as before are used for the solver, with a constant permeability model and $\lambda = 1$.

In Figure 4.12, we see that the three cases where the rock pressure is used present more compaction in the basin than when only lithostatic pressure is used (besides from the fluid pressure). This is likely due to the lack of consideration of the forces arising from the interphasial pressure between the rock and fluid as well as viscous forces. These processes were included in the modelling of the rock pressure, which we have also solved for, whereas the lithostatic pressure cannot model any forces other than overlying load under gravity.

4.10 Summary of Chapter 4

In this chapter, we presented the results of numerical simulations in two or three dimensions for the fluid and rock pressure and velocities, porosity, and temperature for several fundamental scenarios of a sedimentary basin undergoing compaction. The results provided us and PDS with a catalogue of different insights into the evolution of a basin in the absence of any complex geological features, and presented an example of how our model can be extended from two to three dimensions easily. We now summarise each case and give concluding remarks.

4.10.1 Base results for sedimentation and compaction

We first presented simulations of the two- and three-dimensional base problems. We then compared the two-dimensional results with sedimentation to those obtained without sedimentation. In general, the qualitative behaviour of each of the solutions were the same. We found that when sedimentation takes place, the basin undergoes a larger porosity loss, which is expected given the additional load from deposition. In general, we conclude that sedimentation alone does not change the qualitative behaviour of the basin, and therefore choose to neglect it in the following simulations. However, we have shown the method with which to include it to our base solver if necessary.

4.10.2 The effect of λ

We tested the effect of using different values of the dimensionless sedimentation number, λ, where

$$\lambda = \frac{k_0 \rho_0 g}{\mu_f H_0}. \tag{4.10.1}$$

Small values of λ correspond to having low permeability or high sedimentation rate, and large values of λ correspond to having high permeability of low sedimentation rate.

We presented the results for all variables when $\lambda = 1$, and proceeded to compare the porosity and pore pressure results when different orders of magnitudes for λ were used. For the results, we used a constant permeability model for k, where we let $k = 1$.

We assume our basin is composed of shale-like sediments, and for such materials, we find that the permeability can vary between approximately five orders of magnitude, from $\mathcal{O}(10^{-16})$ to $\mathcal{O}(10^{-20})$. Scaling the reference permeability k_0 accordingly, this is equivalent to using $\lambda = 0.001$ to $\lambda = 10$. Hence we presented the porosity and pore pressure results using $\lambda = 0.001, 0.01, 0.1, 1$, and 10.

We found that the compaction behaviour varies significantly as λ varies. For smaller values of λ we found that the pore pressure is significantly higher than the hydrostatic pressure, and the porosity reduction is small. Further, we found that any significant porosity loss takes place towards the bottom of the basin. The porosity reduces more steadily and at a greater rate as λ approaches 1, and the pore pressure becomes closer to the hydrostatic state. At this value of λ, we found that the porosity profile is almost linear, where it decreases with increasing depth. Finally, at our largest value of $\lambda = 10$, we find that compaction takes place more towards the top of the basin rather than the bottom (like when λ is small). The pore pressure is also found to be near hydrostatic.

The results we found are in line with our physical intuition. For low permeabilities, we would expect the fluid to be less able to escape, therefore accumulating more pressure in the fluid and allowing only a small amount of compaction. This is also equivalent to using a high sedimentation rate (H_0), where we would expect the bottom of the basin to compact more. For high permeabilities, the fluid is expelled from the basin with ease, and we found a large amount of compaction throughout the basin with the pore pressure near hydrostatic pressure. This is equivalent to having a low sedimentation rate, where the top of the basin is able to cope with the slow additional loading, and therefore the top of the basin is able to compact more than the bottom of the basin.

The qualitative behaviour of the porosity profiles found are in line with what has been previously found in literature using simpler models (for example, by Audet and Fowler (1992)). Hence, we can conclude that our model which incorporates the presence of more geophysical phenomena (such as chemical compaction, consideration of rock stresses and viscosities, coupling of all fundamental variables) is able to produce correct compaction behaviour.

4.10.3 Comparison between constant and porosity-dependent permeability models

We had previously used $k = 1$ in our simulations, but realistically, k is sensitive to the value of porosity. We chose our permeability model to follow a Kozeny-Carman type with

$$k = \left(\frac{\phi}{\phi_0}\right)^8, \tag{4.10.2}$$

where the dimensional scaling k_0 has been incorporated in the definition of λ. Clearly, with the chosen permeability model, k decreases rapidly with decreasing ϕ, and we expect different behaviour in our simulation results.

We compared the case where k is constant with when the porosity-dependent permeability model is used. When compared to the case where $\lambda = 1$ and $k = 1$, we found that for the porosity-dependent permeability model using $\lambda = 1$, compaction takes place more at the top of the basin (where $k \sim \mathcal{O}(1)$) and much more slowly with time towards the bottom of the basin (where $k \sim \mathcal{O}(10^{-1})$).

From the simulation results for the porosity-dependent permeability model, combined with previous results for small λ, we can conclude that using a varying permeability model will provide more accurate and physical results than when a constant model for k is used, though a constant permeability model may still provide sufficient results for thin layers over a short period of time (for example, for a depth of less than 1km for a period of one million years). This is due to the sensitivity of the value of k on the porosity. Hence, the porosity profile would be qualitatively different if a non-constant permeability model was used compared to if a constant model was used.

4.10.4 Mechanical and chemical compaction

One of the geophysical phenomena often neglected that we include in our model is the process of chemical compaction. Mechanical compaction usually represents the compaction due to forces arising from overburden weight, whereas chemical compaction aims to model the reduction in porosity due to grain rearrangement and other chemical processes between the fluid and rock that may lead to a porosity change.

We separated the combined compaction model into two separate models — one modelling mechanical compaction only, and the other modelling chemical compaction only. We found that there are fundamental differences between using the two models, where chemical compaction produces an almost linear profile where the porosity decreases with decreasing height, and the mechanical compaction produces a convex

profile. Hence, we concluded that the two mechanisms produce different behavioural contributions to the compaction.

More importantly, we found that, using the parameters found empirically and from other data (Senior et al., 2016), chemical compaction produces a significant contribution to the overall porosity change of the basin over time. Hence, we believe that it is crucial to include the chemical component (currently often neglected in thr literature and models used in industry) to the porosity equation to better model as many of the geophysical processes as possible that may contribute towards the compaction within the basin.

4.10.5 The viscosity effect

Viscosity is an important factor in our model which is again largely neglected. We believe that as the sediments lithify and turn from sediments to rock, the viscosity of the bulk material will increase, since hardening of the rock matrix will hinder its ability to flow. All sedimentary basins over time will experience lithification for the sediments to bind into rock, so we believe that accounting for multiple values of viscosity is an important factor.

Hence, we tested a few different values for μ_{r0} based on the average sediment viscosity value found for shale sediments. We let $k = 1$ and all other parameter values were kept the same as previously. We found that when the sediments are more viscous ($\mu_{r0} \geq 0.5 \times 10^{21}$), the porosity hardly decreased. However, for less viscous rock ($\mu_{r0} \leq 1 \times 10^{20}$), the porosity profile was found to be sensitive to the value of the rock viscosity.

From our results, we learned that viscosity can have a large effect on the results. Although we do not model the cementation process in our model, we believe that it should be incorporated in future work to account for the potential significant consequences of the process.

4.10.6 Different effective stress models

One of the major changes in our model to those widely used is our use of the rock pressure instead of the lithostatic pressure. The calculation of the rock pressure is seldom seen in other models, though we believe that the rock pressure directly affects the behaviour of the enclosed fluid. Indeed, in the derivation of our conservation of momentum equations, we assumed that the rock and fluid undergo not only overlying

weight under gravity, but also viscous and interfacial forces. Hence, we are able to incorporate more processes that the rock and fluid may be experiencing.

We tested four different effective stress models to compare their behaviour. First was the one used everywhere other than in this section, where the effective stress is defined to be the difference between the rock pressure and fluid pressure. The second was one commonly found in literature, where the effective stress (often called the vertical effective stress) is defined to be the difference between the lithostatic pressure and fluid pressure. We also considered a model where the mechanical compaction is assumed to depend on the difference between the lithostatic pressure and fluid pressure, whereas chemical compaction is assumed to depend on the difference between the rock pressure and fluid pressure. This model then assumed that mechanical compaction only depends on the overlying weight on a larger scale than the chemical compaction, which is assumed to be significant on a microscopic scale, where the fluid pressure is directly influenced by the immediately surrounding rock matrix. Lastly, we considered the case where the effective stress is defined to be the difference between the phase-averaged pressure and the fluid pressure.

We saw that whenever the rock pressure is used, the basin experiences more compaction, and the results differ significantly from when only lithostatic pressure is used in the definition of the effective stress. We believe that this is due to the neglect of all the forces acting on the rock and fluid as previously mentioned. The remaining profiles where the rock pressure is used in the effective stress definition are not hugely different from each other. Unfortunately, we cannot determine which of the remaining three definitions of the effective stress is the most accurate, but we can conclude that the rock pressure should be included to model as many processes taking place in the basin as possible.

4.10.7 Concluding remarks

In this chapter, we presented our numerical simulation results for a number of different cases which represent various different geological scenarios, and also showed that our model and solver can easily be extended to accommodate a third dimension. Some results we found were in line with physical intuition or what has previously been found in literature or by PDS. We found that a varying permeability model would model the compaction more accurately than using a constant permeability model.

We also found some results which differed from those used in the literature or in industry. We found that chemical compaction should not be neglected, since it can provide a significant contribution to compaction. Hence, this is an improvement to

what has often been used previously. Further, we were able to produce good results for the rock variables, and concluded that the modelling of rock variables are also crucial in determining more accurate behaviour of sedimentary basins.

In summary, our models were able to determine the profiles within a basin with a more diverse range of physical processes, such as viscous forces as well as chemical compaction. Our simulation results provided a good insight into the compaction of sedimentary basins using different control parameters and constitutive equations, such as the effective stress or permeability. From our results, PDS can now determine which parameters to vary, if necessary, to model different geological situations (such as lithification, or purely mechanical compaction, and so on).

Chapter 5

Compacting basins in the presence of complex geological features

So far, we have examined the effects of different rock properties and compacting mechanisms in the evolution of sedimentary basins. In this chapter, we solve for the pressure, velocity, porosity, and temperature profiles in sedimentary basins with geological features such as faults and sills, which is of highest importance to our industrial collaborator. We observe and discuss the resulting behaviours within the basins.

5.1 Laterally varying stresses

For the solver results we obtained prior to this chapter, we have found the behaviour to be mostly vertical and almost independent of any variations in the $x-$direction for all variables. This is the qualitative behaviour which has been found from most basic compaction models in literature, but we have previously noted that many of the models are over-simplified and do not take into account more realistic geological features. One of the prominent features of our solver used for our model is that it is able to compute the variable profiles in two or three dimensions. In this section, we present the results of a more realistic case which may show two dimensional behaviour by including some more physical mechanisms into our base model.

Thus far, we have considered there to exist a layer of water of constant depth across the basin. This was modelled via the top stress boundary condition in the rock equations, given by

$$\boldsymbol{n} \cdot (-p_r \boldsymbol{I} + \alpha \underline{\underline{\boldsymbol{\tau}}}) \boldsymbol{n} = -p_{\text{top}} \tag{5.1.1}$$

(refer to Figure 3.1), where we defined $p_{\text{top}} = 1$ in all previous simulations. However, it is physically more realistic to model the compacting basin subject to varying normal

stresses at the top of the basin, and we estimate that this is usually dependent on the climate over geological periods. Hence, we now assume that the normal component of the normal stress varies with space along the top of the basin. We then would expect some laterally varying behaviour in our profiles that we solve for, rather than the predominantly vertical behaviour previously observed.

Throughout the subsequent simulations, we now let

$$p_{\text{top}} = -\left(1 + 0.01 \sin\left(\frac{\pi x}{20}\right)\right), \tag{5.1.2}$$

with the basin domain still defined by $\Omega = \{0 \leq x \leq 20, 0 \leq z \leq 10\}$ and using all parameters as in Chapter 4 with $k = 1$. Note that this choice for the pressure on the top boundary of the basin is equivalent to having a large 'puddle' on top of the basin, where the water layer is deeper towards the middle of the basin than its edges. The solutions after ten million years for the simulation with p_{top} as in (5.1.2) are shown in Figure 5.1.

In Figure 5.1, we can clearly see two-dimensional behaviour in our solutions. These are most apparent in the solutions for the rock and fluid velocities. Let us comment on the rock velocity first. The vertical component of the rock velocity is given in the second column and third row of the figure. We see that the vertical rock velocity is largest in magnitude towards the centre of the basin along the top boundary, and is comparable to the rock velocity found when $p_{\text{top}} = -1$ is used. However, towards the sides of the basin, the downward velocity of the rock is smaller than in the centre, even though $p_{\text{top}} \leq -1$ at all points along the top boundary. Further, we find that compared to the height of the basin after ten million years where $p_{\text{top}} = -1$, the height of the basin in the centre is smaller in the case of laterally varying stresses, whereas it is higher on the sides. This suggests that the sides of the basin accommodate for the increase in normal stress towards the centre, and whilst the sides still undergo some downward pressure, the vertical movement is lessened and relatively bulge up as the centre is pressed. We see a notable dip towards the centre of the basin, which would be expected with the increase in pressure around the middle.

Let us discuss the vertical fluid velocity, as shown in the right hand side column and the second row in Figure 5.1. We again observe some lateral variation in the vertical fluid velocity across the basin, most notably along the top of the basin. We see that towards the edges of the top boundary, the fluid is being expelled from the basin the fastest, whereas it is slow towards the middle. This is physically intuitive as we would expect that if more pressure is applied towards the centre, the fluid would have to be expelled from where there is less pressure.

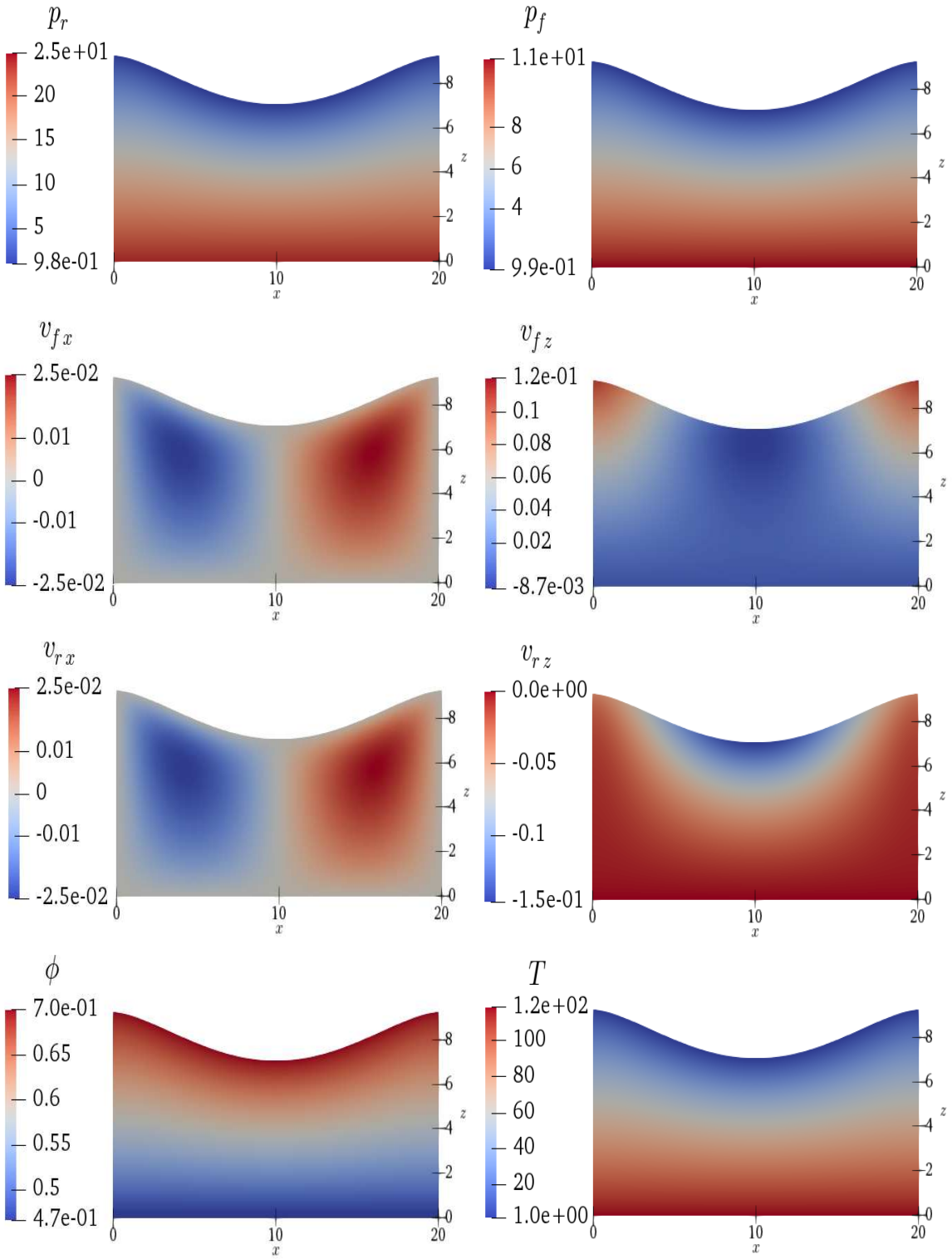


Figure 5.1: Solutions for all variables after ten million years with laterally varying stresses at the top of the basin.

Now observe the horizontal velocities for both the fluid and rock. We see that the behaviour of the two profiles (left hand side column on the second and third rows in Figure 5.1) for the horizontal velocities are almost identical. They both present a horizontal flow which moves away from the centre of the basin. This is as expected since the fluid and rock would move away from where the pressure is most applied.

The other profiles from the pressures, porosity, and temperature do not show significant horizontal variations in the solutions, though with closer observation, we do see that there are small changes laterally towards the top of the basin in particular. With the given normal stress condition as in (5.1.2), we believe that the solution variables are not largely affected towards the bottom of the basin when compared to the case where a constant normal stress condition is used.

5.1.1 Summary of the effect of varying rock stress conditions

Until this chapter, we found the solutions for all variables to only vary significantly in the vertical direction. In order to show that a simple change in parameters can present two-dimensional behaviour, we changed the top boundary rock stress condition from

$$p_{\text{top}} = -1 \tag{5.1.3}$$

to

$$p_{\text{top}} = -\left(1 + 0.01 \sin\left(\frac{\pi x}{20}\right)\right). \tag{5.1.4}$$

This has resulted in a clear two-dimensional behaviour in both rock and fluid velocities, and a more subtle lateral variation in the solutions for the other variables. We see that our solver, which is able to accommodate the extra dimension, is able to provide good results that are physically intuitive.

Another effect we have seen from the change in boundary condition is the deformation of the basin geometry, as expected. The basin has deformed according to the applied pressure, and the sides of the basin have accommodated for the extra pressure applied towards the centre of the basin, and do not move downwards as much as when a constant normal stress condition is used. To better observe how the nodes within the discretisation of the basin have moved, we present the finite element mesh for the solution after ten million years in Figure 5.2.

From the results we have found in this section, we can conclude that a small change in the normal stress boundary condition for the rock has resulted in significant changes in the horizontal direction in our variables. We expect that it is unrealistic to model real geological situations via a constant normal stress condition across the

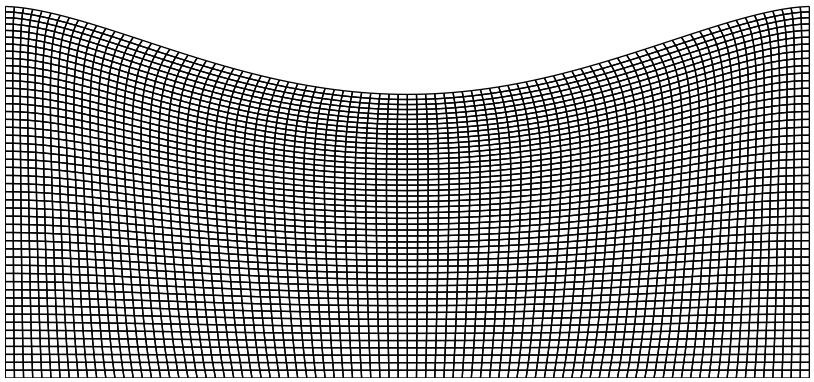


Figure 5.2: Discretised grid after ten million years when a laterally varying normal stress condition is used.

width of the basin. This is because whilst the porosity values may not vary laterally significantly, we have clearly shown that the mesh varies in the x-direction as well as vertically. Hence, it is not realistic to be able to take an 'vertical strip' approach when computing our model, as the 'strips' will no long be vertical. It may be able to take such an approach if the vertical segments were very thin, but for long period of time for longer than 10 million years, one would require a very fine grid for the solutions on each segment to be appropriate. Hence, this would affect the computation time greatly, and it is much more efficient to carry out a 2D simulation rather than requiring a large number of segments to solve on. Additionally, we see that the magnitude of the horizontal velocities are comparable to the vertical velocities for both the rock and fluid, and solving in vertical strips will not be able to account for such behaviour.

Further, since even a small change in the value of the boundary condition has resulted in different compactional behaviour, we believe that calculations extending to the second lateral dimension are necessary to determine the more realistic evolution of a sedimentary basin. Hence, we believe that it is unrealistic to assume that compaction in reality is a purely vertical process, as mostly seen in current literature.

5.2 Geological faults

Faults in sedimentary basins are one of the most common geological features observed in sedimentary basins. Due to their ubiquity, we believe that it is essential to understand the behaviour of the rock matrix and its properties in the presence of faults. In this section, we present a method with which we can model the pressure and other variable profiles near a fault in a sedimentary basin. We examine the profiles near purely vertical, and diagonal faults.

5.2.1 Modelling of faults

We assume throughout this section that, along the fault line in a basin, the fluid is able to flow with ease. Since essentially a fault line is a crack, we believe that the permeability would be large near this crack. Hence, we model the fault into our system by defining the permeability along the line. For our basin domain, which we still take to be $\Omega = \{0 \leq x \leq 20, 0 \leq z \leq 10\}$, we define the permeability to be equal to

$$k = \max\left(\frac{\exp(-y^4)}{0.001}, 0.5\right), \tag{5.2.1}$$

where y is the distance to the fault line. Then, along the most centre part along the fault, we have a large permeability, which rapidly decreases as we move away from the fault line until a 'background' permeability of 0.5 is reached. If, for example, the fault line was along $x = 10$ vertically down the basin, then the permeability is as shown in Figure 5.3. The permeability model as given in (5.2.1) is a modification from that suggested and used by Bangerth et al. (2016) in their flow computations for ground water simulations with a crack. The values of the constants taken in (5.2.1) were decided after discussing shale material parameters with Senior et al. (2016), so that the values produced by the model are realistic.

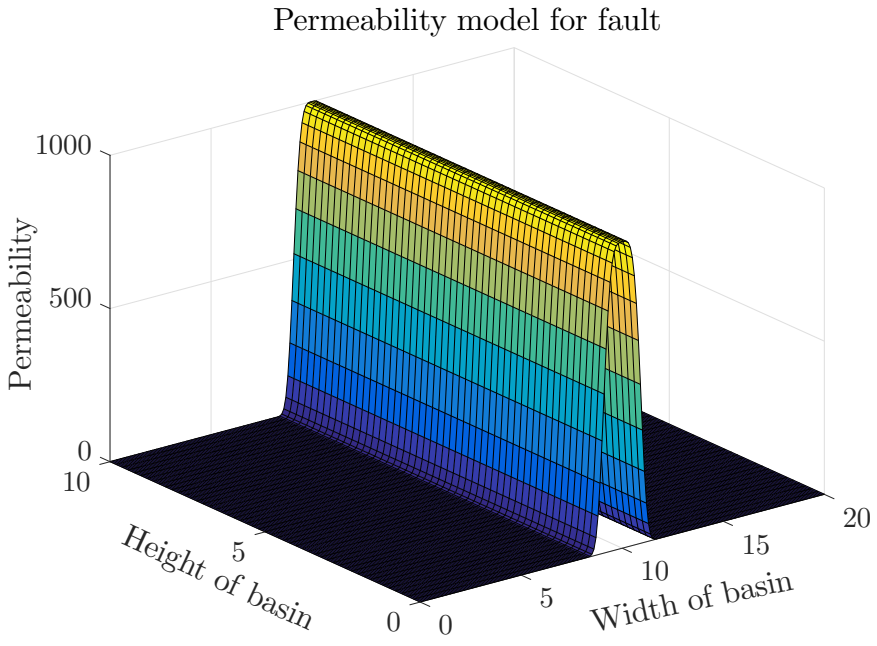


Figure 5.3: Permeability profile in the presence of a fault along $x = 10$.

This change in the permeability model is the only variation in parameters we make in order to model faults into our foundation model in previous chapters. Note further

that throughout this section, we do not move the mesh according to the rock velocity. This is because we expect some abnormal behaviour in the flow along the fault line, which we are currently modelling to contain both rock and fluid, rather than just fluid as it would be in reality. When we consider the method with which we move our mesh, we believe that the mesh movement may may interfere with the location of the fault, as well as the flow along and near the fault line. Hence, we omit any mesh reconstruction during fault modelling.

5.2.2 Grid refinement

At the initial stages of running the simulations in the presence of faults, we found that the finite element mesh which we use was required to be very fine in order to accommodate the rapid decrease in permeability as defined in (5.2.1) near the fault line. We further found that refining the mesh globally was computationally inefficient since the elements needed to be small along the fault line but the variation in the values of the solution was relatively insignificant everywhere else in the basin. Hence, we introduced an adaptive refinement technique into our solver when running simulations in the presence of faults in our domain. We briefly discuss the numerical implementation for adaptively refining our mesh.

For the refinement, after solving at a certain timestep, we first find the local smoothness of the solutions by calculating the jumps of the solutions over the edges of cells in the grid. Via an integrated function in `deal.ii`, we refine a particular percentage of the elements containing the highest jumps of a particular variable. We can also coarsen a particular percentage of the elements containing the lowest jumps. Throughout this section, we decide to refine 10% of the grid and coarsen 3% of the cells based on the jumps of the gradients of the rock solutions only. Note that we could alternatively set the adaptive refinement criterion to be based on the permeability field rather than the rock solutions. However, in order to demonstrate and present the general method with which we aim to carry out the mesh refinement for any given scenario, we use the rock solutions for the refinement. The technique we use here is based on the error estimator scheme devised by Kelly et al. (1983) originally designed for use on Laplace equations. The criterion we use is a modified Kelly estimator, with the estimator which measures the jumps in gradients for each cell K defined by

$$\eta_K^2 = \frac{h_k}{2p} \sum_{e_i \in \delta K} \int_{\delta e_i} \left[a \frac{\partial u_h}{\partial \boldsymbol{n}_i} \right]^2 \mathrm{d}e_i, \tag{5.2.2}$$

where h_k is the maximal face diagonal, p is the degree of the approximating polynomial, e_i are the edges of the cell (where clearly $i = 1, .., 4$ since we use rectangular elements), $[\cdot]$ denotes the jump across e_i, a is a scaling coefficient, and u_h is the computed numerical solution. The error estimator and integral within the terms are all automatically processed via cell iterators, appropriate Gauss quadrature formulas, and other functions within `deal.ii`.

Recall that the initial solutions for the temperature and porosity are known, and using these, we estimate the initial profiles for the rock and fluid velocities and pressures. Proceeding to the next time step, we then solve for the porosity and temperature at this timestep. At this point, we solve for the rock and fluid solutions, and immediately re-solve for the rock and fluid solutions after refining based on the first set of rock solutions at this timestep. Note that the porosity and temperature solutions we found for the same timestep are distributed over the new mesh before solving for the rock and fluid solutions on the refined grid. We adaptively refine 3 times at this timestep before moving on to the next timestep. We do not refine the mesh again in our simulations.

5.2.3 Vertical faults

We observe the behaviour of our six variables in the presence of a purely vertical fault down the centre of our basin (where $x = 10$). Hence, the permeability in the basin is defined to be

$$k = \max\left(\frac{\exp(-(x-10)^4)}{0.001}, 0.5\right). \tag{5.2.3}$$

The resulting profiles after ten million years for the pressure, velocities, porosity, and temperature are presented in Figure 5.4. Further, the refined grids at each adaptive refinement step are shown in Figure 5.5.

At first glance, we immediately see the presence of some disturbance along the fault line. All profiles show predominantly vertical behaviour (in the basin away from the fault line) similar to those obtained when there is no fault. However, the z-component of the velocities clearly shows some horizontal variations, again suggesting that two-dimensional modelling is necessary.

From the porosity profile, we conclude that a vertical fault does not affect the general compaction behaviour. The temperature profile seems almost unaffected by the vertical fault line. However, we see from the vertical components of the velocities that the presence of a fault line causes lateral variations. We see that around the fault line, the fluid is moving rapidly down along the line, whereas it moves up and out of

the basin in the rest of the basin in the compaction process. The fluid is clearly being sucked towards and down the fault line.

Note that along the fault line itself, we find some unrealistic values for the profiles. In particular, the rock pressure values soar and drop back down significantly along the fault line, and we see similarly large and unrealistic values for the velocities along the fault line. This is confirmed by the refinement which is based on the rock solution. Figure 5.5 clearly shows that the mesh has been refined mostly along the fault line. We believe that the unrealistic values along the fault line are obtained due to such rapid changes in the value of k along the fault line which may not be resolved properly in our numerics. Further, our model for a fault assumes that rock and fluid co-exist along the fault line like the rest of the domain, when in reality, there would be no rock and only fluid along the fault line. We do not accommodate for this physically in our domain. However, we do not concern ourselves with the particular values along the fault line since we are more interested in the behaviour of the basin away from the fault line.

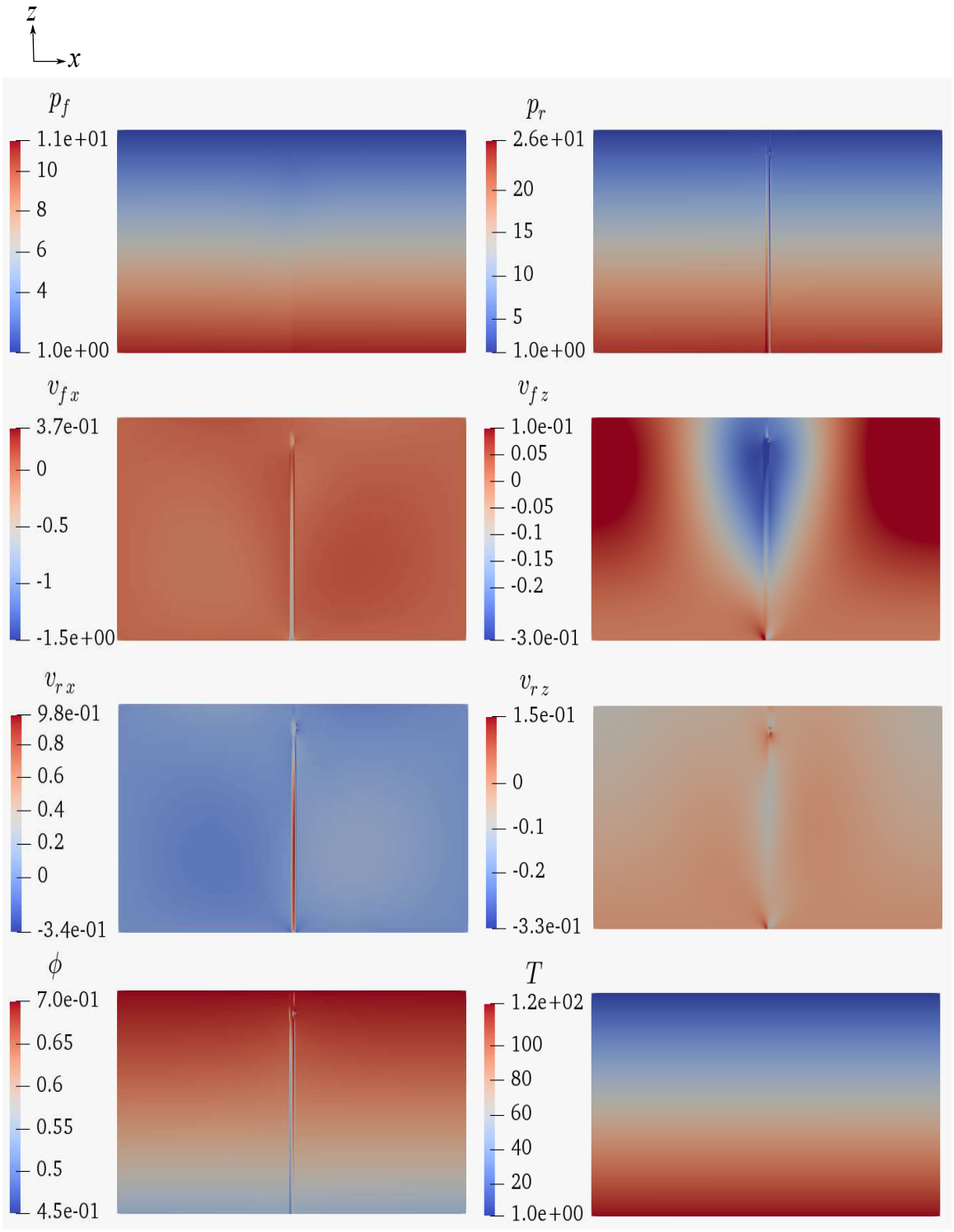
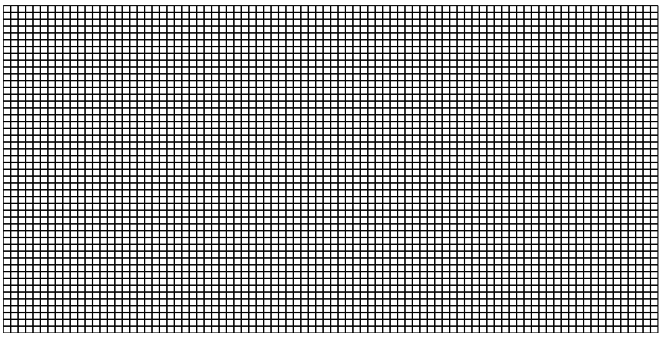
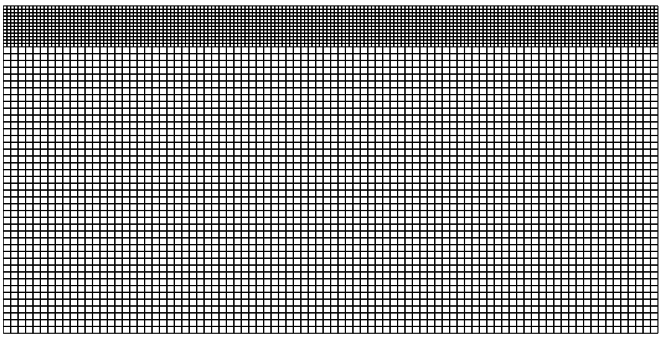


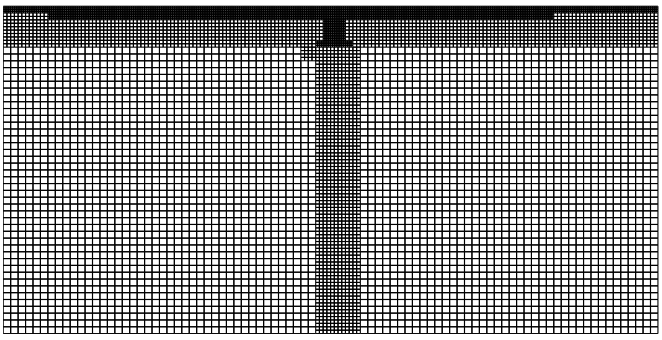
Figure 5.4: Solutions for all variables after ten million years in the presence of a vertical fault. Recall that we do not move the mesh here as discussed in Section 5.2.1, and the domain is always defined by $\Omega = \{0 \leq x \leq 20, 0 \leq z \leq 10\}$.



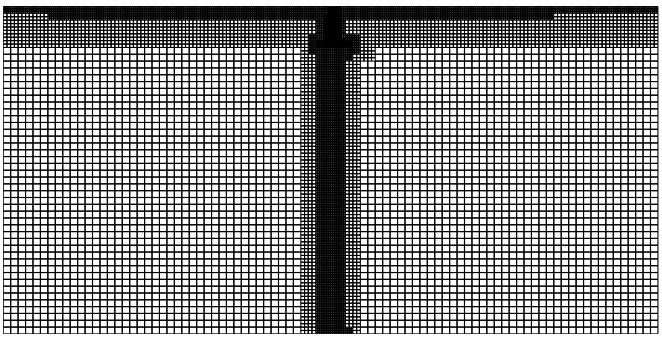
(a) Initial grid.



(b) Mesh after first adaptive refinement.



(c) Mesh after second adaptive refinement.



(d) Mesh after third adaptive refinement.

Figure 5.5: Resulting finite element grids at each adaptive refinement level in the presence of a vertical fault. Note that we also observe significant refinement along the top boundary. This is likely due to the number of relatively complicated boundary conditions that are imposed there, including the normal rock stress condition.

5.2.4 Multidirectional faults

We now consider a fault which also has horizontal variations. We define the permeability model in the basin with a diagonal fault along the equation $z = 4 + \frac{x}{10}$ to be

$$k = \max\left(\frac{\exp(-(z - 4 - \frac{x}{10})^4)}{0.001}, 0.5\right). \tag{5.2.4}$$

The solutions for this case after five million years is shown in Figure 5.6. The resulting grids after each refinement step are shown in Figure 5.7.

Once again, the temperature profile does not seem largely affected by the fault line. The other profiles however show interesting behaviour. Since our fault line now goes across the basin interfering with the predominantly vertical compaction behaviour, we find that this affects the general flow of the rock and fluid in the basin.

Let us consider the pore pressure. We find that the pressure builds up more below the fault line compared to the case where there is no fault line. The extra pressure increase below the fault line can clearly be seen. This can be explained by the fact that the fault line will disrupt the flow of fluid. When previously, the fluid was able to escape upwards through the basin freely without obstruction, the fluid is now contained (often described as 'compartmentalised') below the fault line and with some fluid having to flow along the fault line rather than upwards out of the basin. We see a similar behaviour in the vertical component of the fluid velocity where its magnitude is smaller below the fault line compared to above it, suggesting that the fluid is escaping from the bottom portion of the basin slower than the top portion. We find that in general, the basin does not compact as much with the fault line going across the basin, which is to be expected if the pore pressure is larger there when compared to the case without a fault.

We again find a large jump in most of the solutions across the fault line, as again confirmed by the grids seen from adaptive refinement (Figure 5.7). In fact, in the case for the multidirectional fault, the solver eventually crashes (after five million years) due to the large jump in the rock pressure solution in particular at the level of refinement we have been able to compute. This jump is due to the reasons discussed in the previous subsection, where the rapid change in k is perhaps not able to be accommodated in our numerical solver and our mesh size. However, we are able to examine the changes in the qualitative results even after five million years especially away from the fault line, and find that the variables behave as expected in the presence of a fault line.

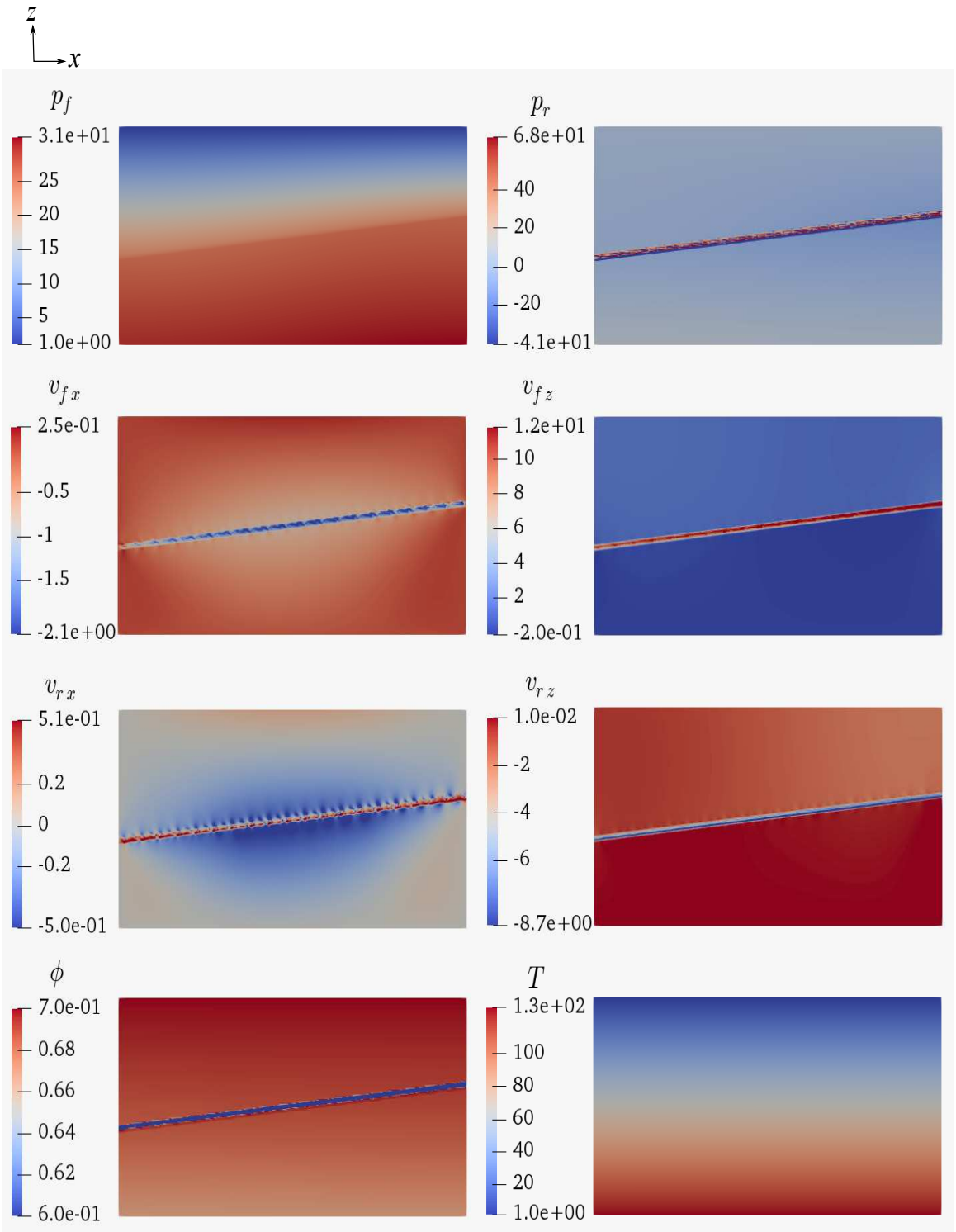
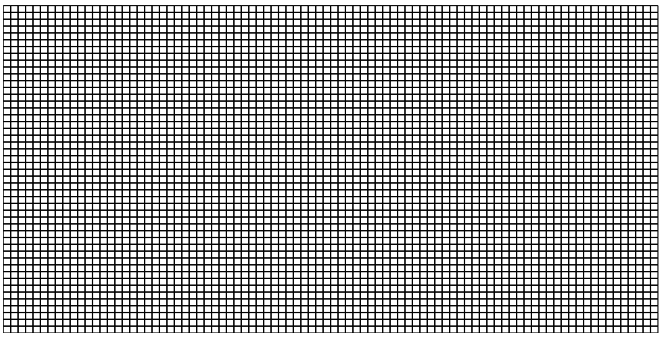
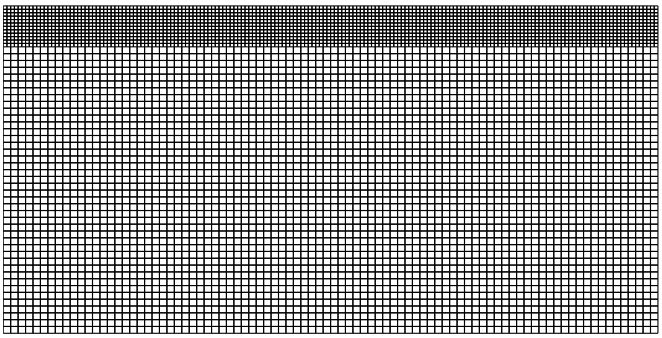


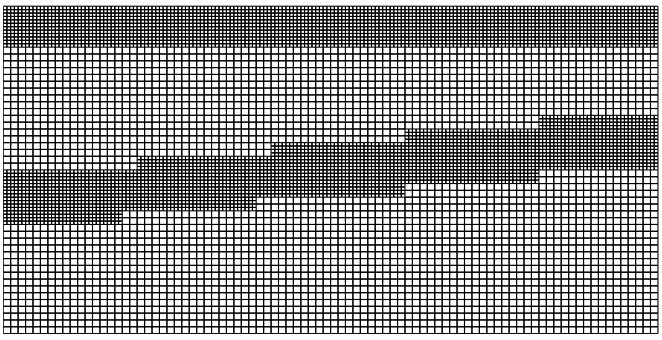
Figure 5.6: Solutions for all variables after five million years in the presence of a diagonal fault. Again, the mesh is not moved such that $\Omega = \{0 \leq x \leq 20, 0 \leq z \leq 10\}$.



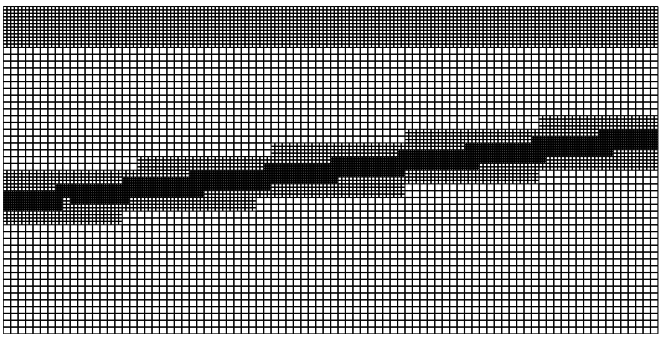
(a) Initial grid.



(b) Mesh after first adaptive refinement.



(c) Mesh after second adaptive refinement.



(d) Mesh after third adaptive refinement.

Figure 5.7: Resulting finite element grids at each adaptive refinement level in the presence of a a diagonal fault. We again observe some refinement near the top boundary.

5.2.5 Discussion of results

We have found that we obtain some large jumps in our solutions. This is due to the way we model the fault, where we allow the permeability to rapidly increase then decrease across the fault line. This in turn affects the pressure gradient, which then affects the rock solutions. Since the remaining variables are largely dependent on the rock solutions, we find that the non-smooth behaviour carries through into our other variables.

However, the behaviour away from the fault line is as expected qualitatively. In fact, although the solution values along the fault line may seen unrealistic and essentially incorrect, it is not unreasonable to ignore the seemingly incorrect behaviour. This is since in reality, by the structural definition of a fault, there is no rock present along the fault line. Hence, whatever solution values we obtain along the fault line for the rock are irrelevant since the material does not exist along the fault. Further, we are in general interested in the overall qualitative behaviour away from the fault line, rather than immediately surrounding it. Therefore, we need not be concerned by the unrealistic values along the fault line itself.

The modelling of faults can be improved if the solver could model a void of rock along the fault line. We could impose some jump conditions on the variables instead in order to allow for the continuum. Alternatively, we could also try refining the cells around the fault line even further, and see if this improves the results.

Whilst our fault modelling method has its downfalls, we can conclude that we are in general able to obtain the expected behaviour qualitatively using our solver via this method. Whilst we are unable to exactly model the behaviour on and very close to the fault line, we are able to solve for the variables in the remaining parts of the basin. We clearly see compartmentalisation occurring, with the fault line seemingly dividing the basin into two compartments that behave separately to one another.

5.3 Sills and dykes

Recall that sills and dykes are magmatic intrusion in sedimentary basins. Under their presence, the basin undergoes a large influx of heat from the magma that has entered. Similar to sedimentation, the timescale with which an intrusion takes place is relatively short compared to the compaction process. To model sills, we use the

source term S_T in the temperature equation, given by

$$\frac{\partial}{\partial t}((\phi\rho_f c_f+(1-\phi)\rho_r c_r)T)+\nabla\cdot((\phi\rho_f c_f \boldsymbol{v}_f+(1-\phi)\rho_r c_r \boldsymbol{v}_r)T) = \frac{1}{\mathrm{Nu}}\left(\nabla\cdot(\kappa_T\nabla T)+S_T\right), \tag{5.3.1}$$

in its dimensionless form. This source term is modelled such that the sill intrusion takes place at a certain point in time only. For our model, we define the source term to be (Senior et al., 2016)

$$S_T = \begin{cases} 150(H(t-3)-H(t-3-\Delta t)), & 5<z<5.5, \\ 0, & \text{otherwise}, \end{cases} \tag{5.3.2}$$

where $H(t)$ is the usual Heaviside function and Δt is the timestep size, so that the sill intrusion is taking place at 3 million years for the duration of one timestep. We then observe the changes in the temperature profile from the point of sill intrusion and examine its effect on the other profiles, if any.

For these simulations, we use the same parameters as in Section 4.5 with the timestep at 0.1 (equivalent to 0.1 million years). We solve the same equations for the remaining variables, with the temperature equation as in (5.3.1). We allow for compaction so that the mesh moves accordingly.

5.3.1 Simulation results with a sill intrusion

We show the resulting profiles at $t = 3$ (equivalent to 3 million years) in Figure 5.8. At first sight of Figure 5.8, we see that the temperature in the right bottom corner of the figure is largely affected by the sill as expected. There is a significant surge of temperature around $5 < z < 5.5$ where the sill intrusion has taken place. The remaining profiles however do not seem largely affected by the sill at that time.

5.3.1.1 Temperature results

Let us examine the temperature evolution more closely from the point of sill intrusion. Figure 5.9 presents the temperature profiles in 0.2ma increments (equivalently) from $t = 3$ up to $t = 3.8$. The blue line shows the temperature at the point of sill intrusion, and we see that the temperature soars around the sill. From then on, the temperature relatively rapidly decreases away from the sill, and around the sill itself, the temperature steadily decreases with time. The heat is diffused from around the centre of the sill towards the bottom of the basin, where the temperature briefly rises, but then subsides from around $t = 3.6$ (after 3.6 million years).

To examine the longer-term effects of the sill, we turn to Figure 5.10, where we now plot the temperature for 3, 5, and 10 million years. Further, we also plot the temperature profiles at the same times when there has been no sill intrusion. We see that the temperature at the bottom of the basin is still higher after 5 million years immediately following a sill intrusion than without. Hence, we conclude that the sudden heat flux towards the middle of the basin is still being diffused out of the basin even after 2 million years. At the 10 million year mark, the temperature has significantly subsided from the sill intrusion, but is still relatively higher than when there has been no sill, with the temperature roughly twice of that when there has been no sill intrusion.

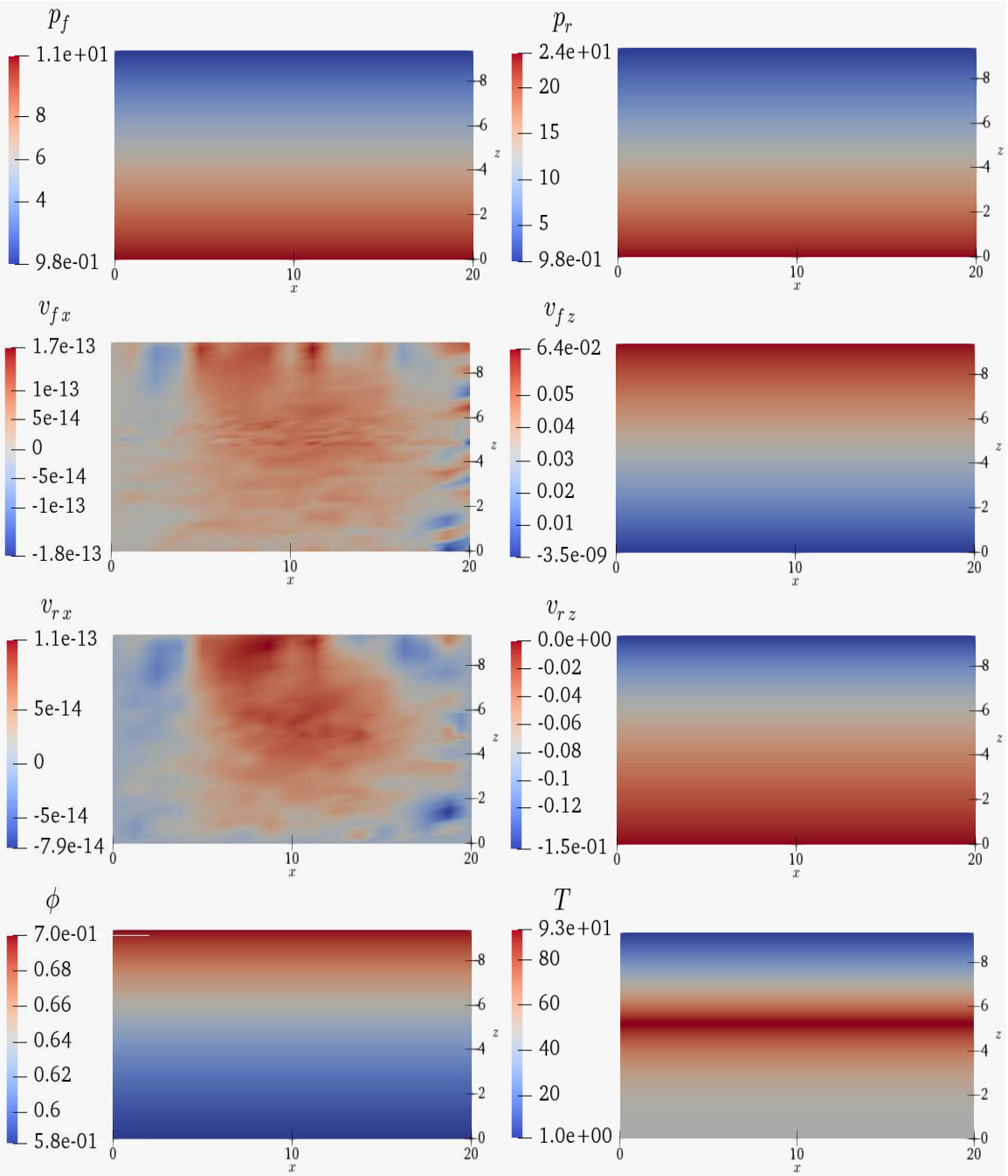


Figure 5.8: Solutions for all variables with a sill intrusion after 3 million years.

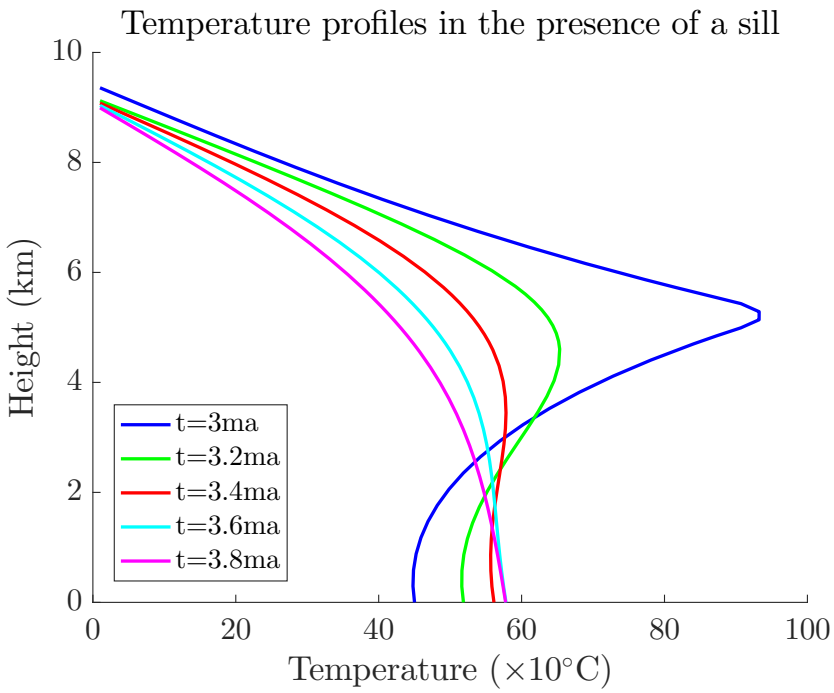


Figure 5.9: Temperature profiles in 0.2ma time increments from the time of sill intrusion (3ma).

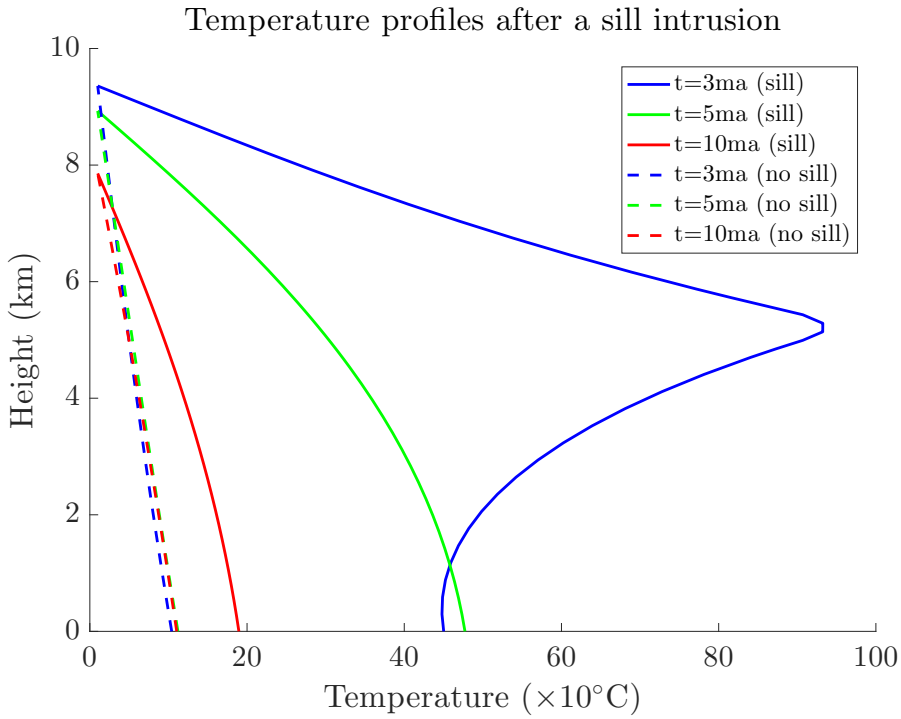


Figure 5.10: Temperature solutions at 3 and 5 million years, with and without sill intrusion.

5.3.1.2 Porosity results

Recall that the temperature at this stage did not largely impact the rock and fluid equations for the pressure and velocities. Realistically, the density would also depend on the temperature, but we have taken this to be constant in our simulations. However, the rock viscosity, which is given in its dimensionless form by

$$\mu_r = \exp\left(\frac{E}{RT_0}\left(\frac{1}{T} - 1\right)\right), \tag{5.3.3}$$

is dependent on temperature and this parameter is seen in the rock and porosity equations. We find that for the rock variables, the change in rock viscosity due the the temperature changes does not significantly change the results, and the profiles for the rock pressure and velocity remain qualitatively the same as those without a sill. However, we see some significant differences in the results for the porosity when there is a sill. The porosity results for 5 and 10 million years for when a sill has been present and when there has been no sill is presented in Figure 5.11.

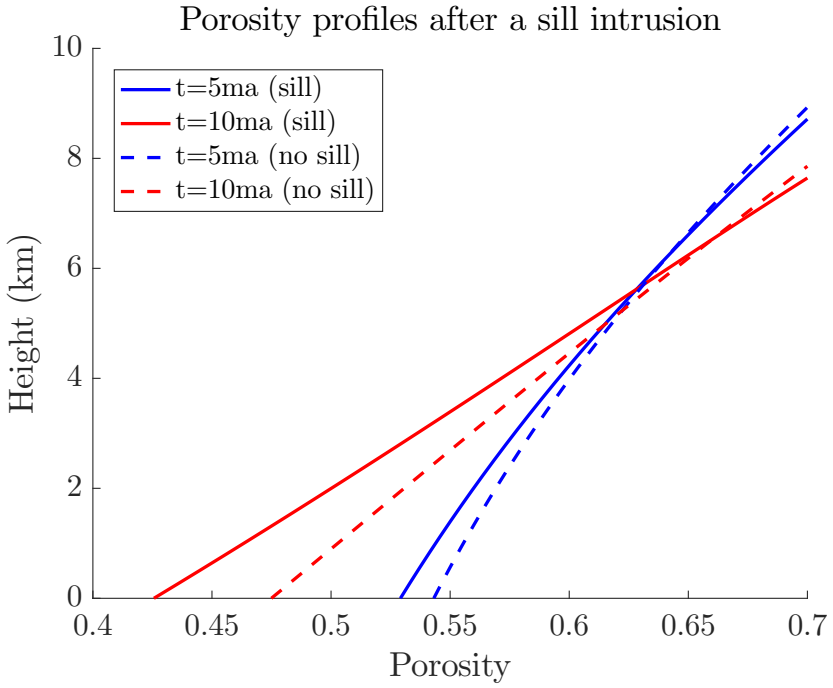


Figure 5.11: Porosity profile comparisons between simulations with and without sill intrusion.

We see that the porosity decreases more rapidly when a sill has been present. We can explain this observation by considering our (dimensionless) porosity equation,

which is given by

$$\frac{\partial \phi}{\partial t} = -\phi_0 \Gamma \exp\left(-\Gamma(p_r - p_f)\right) \frac{\partial}{\partial t}(p_r - p_f) - \Upsilon \frac{C(\phi)}{\mu_r}(p_r - p_f). \tag{5.3.4}$$

Here we use the partial derivative in time rather than the material derivative, since we are allowing the mesh to move with the rock velocity. In the second term on the right hand side of (5.3.4), we see that the rock viscosity term affects the chemical compaction directly. Recalling the definition of rock viscosity, (5.3.3), we can conclude that as the temperature increases, the viscosity rapidly decreases. We also recall that in general, fluid flows more easily with smaller viscosity, whereas more viscous fluids flow much slower. Hence, in this case where the temperature is significantly increased by the sill, we have that the viscosity of the rock (which is modelled as a fluid) reduces, and therefore the rock is expected to flow with much more ease, with pressure solution also becoming a much easier process. With this, we further expect the rock to be able to compact with much more ease, and therefore, we expect much more compaction as observed in our simulations. Note that this is in line with the viscosity effect results we found in Chapter 4.

From the equation (5.3.4) alone, we can also expect that with a smaller μ_r, the second term on the right hand side of (5.3.4) becomes larger in magnitude, and therefore the rate of change of ϕ with time becomes larger in magnitude. This in turns means that there is a bigger reduction in the porosity when compared to the case where the temperature is much smaller, and hence we would expect more compaction, as observed.

5.3.2 Summary of simulations with a sill

We have seen that the presence of a sill can drastically alter the temperature results in compacting basins. Further, the large temperature increase in the basin when the sill is introduced results in an increased reduction in the porosity when compared to simulations obtained when a sill is not introduced. We find that the remaining profiles do not differ largely between the two simulations.

In the introduction, we discussed that many authors in current literature do not couple the porosity, pressure, and velocities with the temperature, and many claim that the temperature can be separated as it does not significantly affect the other variables. However, we have shown clearly in this section that the porosity is largely affected by temperature changes, especially in the presence of a sill. Hence, in a compacting basin where there has been a sill intrusion, we believe that it is imperative

to couple the temperature to the other variables, and we must solve for the variables together to obtain accurate results.

Note that whilst we have not see large differences in the pressures and velocities here, we have made some assumptions that may hide potential further effects of the sill. One of these assumptions is that we have assumed the area of the basin where the sill intrusion has taken place to still possess the same rock and fluid properties as before. Realistically, the area of the basin where the magma has seeped through would have different properties to the rock in the rest of the domain, as the magma acts to destroy the original rock, replacing it with materials with different properties. Further, realistically, we cannot assume that the sill area has the same compacting properties as cooling magma, and once cooled, the sill intrusion can almost act as an impermeable barrier to the surrounding fluid and rock in certain instances. However, even with these assumptions, we have shown at least that the temperature equation cannot be neglected when solving for the porosity, which is a vital component to understanding the evolution of sedimentary basins.

5.4 Summary of Chapter 5

In this chapter, we examined the effects of complex geological features on a sedimentary basin. We discussed the methods with which we incorporate the features, and presented the resulting simulations in each case. We considered laterally varying stresses, faults, and sills. The additional numerical techniques which we used for simulations with faults were also discussed.

To examine the effects of a laterally varying stress, we simply changed the stress boundary conditions for the rock equations at the top of the basin into one that is dependent of the horizontal dimension. We found that even a small change in the value of the top stress, along with the lateral variation, causes a large change in the qualitative behaviour within the basin. In particular, we found that the magnitude of the horizontal velocities are comparable to the magnitude of the vertical velocities, and therefore, it is unrealistic to omit the lateral dimension in our calculations. In reality, we know that the stress on top of the basin will not be homogeneous. Hence, we conclude from these simulations that the basin is sensitive in both directions to small variations of the top stress, and therefore, we believe that multi-dimensional modelling is essential. Whereas most authors and PDS still simplify the compaction process into a vertical one, we have shown that this is not a valid assumption for real sedimentary basins since it will not produce accurate results, or it would require much

longer computational times due to the number of vertical segments one would need to solve.

Faults are one of the most commonly found geological features and we choose to model them via the permeability in our model. Instead of solving for the compaction behaviour in two separate regions split by a fault, we model the fault line as a crack along which fluid can easily flow (relative to the rest of the basin). We find that even in the presence of a purely vertical fault, the basin experiences horizontal variations. The vertical fault primarily changes the fluid movement within the basin, but most other profiles remain similar to the base simulations. We observe significant behavioural changes with the diagonal fault, where the basin experiences compartmentalisation. Below the fault line, we find that pressure builds up significantly whereas it is released more above. We find that the fluid becomes trapped under the fault line and this is indeed what we see in real geological basins.

Sills were modelled as a large heat flux source term in the energy equation. After placing a sill horizontally around half way up the basin, we found that the entire basin undergoes a large temperature increase, which subsides over time towards the profile without a sill. Importantly, we find that the large increase in temperature acts to reduce the porosity significantly more than the case without a sill. This is likely due to the viscosity increasing with temperature, and therefore allowing for quicker compaction. Further, it is clear that the porosity and temperature are closely related and sensitive to one another. Hence, we conclude that it is crucial to couple these equations together and solve them concurrently as we have done here.

Chapter 6

Conclusions

In this thesis, we studied the geological processes within a compacting sedimentary basin and derived a mathematical model and respective solver to better understand these processes. These were improvements on those currently used by our industrial partner, PDS, as outlined in Chapter 1. We also examined the effects of different geological features on the basin numerically. In this chapter, we summarise our work and findings.

6.1 Summary of derived model and solver

In Chapter 2, we derived a model from first principles that describes the fluid and rock movement, and the porosity and temperature evolutions within a compacting sedimentary basin on geological timescales. The model derived supports multiple space dimensions rather than one vertical dimension, the latter of which is commonly used in literature, and describes the rock pressure and velocity evolution, which is not commonly done. From understanding the rock movement, we were able to derive a new porosity model which in our opinion allows for a more accurate description of the interaction between the rock and fluid phases. The porosity equation was also generalised to be able to account for both mechanical and chemical contributions to compaction.

All major properties in the basin (rock and fluid pressures and velocities, porosity, and temperature) are considered as a coupled system in our model, so that their co-dependency is preserved as the basin evolves in time. Our model is written in such a way that it can easily be extended to support any rock types via the constitutive equations, as well as to incorporate further geological features which might be of interest to users. We defined and suggested various constitutive models which would be appropriate in modelling different lithologies and material properties, and our model

serves as a good foundation on which one can incorporate multiple processes. Having derived the model, we nondimensionalised the system and identified the dimensionless parameters that control our model. We recovered the 'sedimentation number', given by λ, which has previously been used in literature, as well as defining new control parameters for the rock, porosity, and temperature models. The newly derived model acted to address PDS' need for a more complex, multi-dimensional unified model, with which multiple geological phenomena and various material parameters can be incorporated at once.

In Chapter 3, we presented the method by which we solve our fully-coupled system of equations with appropriate initial and boundary conditions, which is essential for industrial purposes. We divided the six equations in our model into four subsystems which were solved successively. To solve our system, we employed the finite element method and used the numerical toolbox `deal.ii`. We defined the discretisation for each subsystem and also defined how we incorporate the initial and boundary conditions.

In order to ensure that our solver worked correctly, we used the method of manufactured solutions to verify the solvers for each subsystem. The subsystem equations were simplified, and by adjusting our equations and conditions appropriately, we examined the numerical errors between test solutions to the numerical solutions we obtained. We found that the numerical errors converged with the expected rates as the mesh size was decreased (for all our subsystems) and as the timestep size was decreased (in our time-dependent equations). Hence, we were able to conclude that all our subsystem solvers behave as expected.

We then provided the method with which we can incorporate sedimentation into the model. This was done numerically by manipulating the basin geometry in a brute force manner, where we created the deposited layer based on the existing geometry and updated the domain with the new layer. This was to demonstrate how to extend our solver to incorporate this process. We also provided the method with which we move the mesh with respect to the rock velocity.

6.2 Summary of results and findings

In Chapters 4 and 5, we presented the simulation results for sedimentary basins under the effect of different geological processes and features. These would provide PDS and other relevant industries with further insight into the general behaviour of the generalised model under different circumstances. Chapter 4 involved results from

simulating the basin evolution by incorporating processes that depend on material properties and different constitutive equations. Chapter 5 considered spatial geological features and examined the effects of these on the evolution of a sedimentary basin.

We began by solving our base model in two and three dimensions, and presented the results for a basin undergoing sedimentation. We then solved our system with a constant permeability model, and examined the compaction behaviour of the basin without sedimentation. Our first simulation defined $\lambda = 1$ and solved for the different variables. We first found that with the simplest form of our coupled model, the general behaviour of the basin properties is in the vertical direction only, as found by previous authors. The rock pressure is indeed larger than the pore pressure, with their difference determining the rate of compaction. The temperature variations were found to be steady, and we found that the rock moves vertically downwards as the fluid expels from the basin vertically, as expected.

We then presented results for various values of permeability, which essentially examined the effect of different values of λ on the system. This has been studied by various authors with much simpler models. Five different values of λ were considered, ranging from the lowest to highest orders of magnitude found for shales. We found that as permeability decreases, compaction becomes a more difficult process.

Further, we found that the qualitative behaviour of the porosity profile changes with various values of λ. For small values of the sedimentation number, which correspond to more impermeable rocks or very fast sedimentation, we find that compaction (porosity loss) is more prominent toward the top of the basin. As λ increases, the porosity profile becomes more linear, and at the largest order of magnitude for the permeability (and therefore the largest test value of λ), we find that compaction is now more prominent toward the bottom of the basin. The pore pressure also behaved as expected, where the pore pressure at the bottom of the basin was larger with smaller values of permeability.

We then used a varying permeability model to understand the sensitivity of the basin evolution to a porosity-dependent permeability. We find that using a varying permeability model produces significantly different qualitative results, especially with increasing time. After five million years, the values of the porosity at different points of the basin are not too dissimilar between the results obtained with constant and varying permeability models. However, we notice significant differences after ten million years, where although the compacted height of the basin is relatively close, the porosity profile in the basin is widely different. We find that for a porosity-dependent permeability, the top of the basin, where the porosity is large, compacts more than

the bottom of the basin which does not compact nearly as much when compared to the case of $\lambda, k = 1$. Hence, we concluded that it is much more realistic to use a varying permeability model since the compaction behaviour is highly sensitive to the permeability variations within the model. However, constant permeability models may still be appropriate for short times, or for thin layers.

Previously, we mentioned that our porosity equation is able to consider both mechanical and chemical processes. It is unclear whether one mechanism is more prominent in the compaction process, with many researchers claiming that chemical compaction can be neglected. Therefore, we examined their individual contributions to the porosity loss. We found that both mechanisms give similar magnitude contributions to the compaction, which suggests that chemical compaction is crucial in modelling compaction behaviour accurately. We also found that their individual significance is seen to have different profiles. In particular, we found that mechanical compaction acts to reduce the porosity more in the bottom half of the basin, whereas chemical compaction is seen to be more evenly significant throughout the basin. Hence, we concluded that unlike what is suggested in literature (e.g., by Osborne and Swarbrick (1997)), chemical compaction can be a significant source of porosity reduction, and therefore cannot be neglected.

The viscosity of the rock, which we model as a viscous fluid, is often taken to be constant. In any case, it has not yet been considered as a major contributing factor in the literature, where the rock behaviour and movement are almost always neglected in the modelling of compaction. While cementation is not considered to be a major contributing factor in compaction, it is widely known that sediments will become less 'viscous' as the sediments start to form into hard rock over time. Hence, this motivates the examination of the rock viscosity effects on the basin. In our model, we derived a strain rate number, α, which controls the rock equations and the rock viscosity scale. Further, the rock viscosity is encountered in our chemical compaction term for the porosity equation. Hence, testing four different values of the rock viscosity (with half an order of magnitude between each value), we neglected the mechanical compaction component and compared the results. We found that the porosity evolution is highly sensitive to different viscosity scales. Therefore, we may conclude that cementation may be a significant contributing factor and cannot be neglected in compaction models.

One of our contributions to the compaction modelling work available in the literature is our definition of 'effective stress', which, in all of the literature we have encountered, is dependent on the difference between the lithostatic pressure (pressure

purely due to overlying vertical weight) and the pore pressure. We in turn define it to depend on the difference between the rock pressure and pore fluid pressure, and thereby being able to incorporate lateral variations and the interaction between the rock and fluid phases. Additionally, we presented two further possible models for the effective stress and compared their effects on the porosity evolution. We found that when the rock pressure is not used as part of the effective stress definition, the porosity solution is widely different than the other when the rock pressure is used. When the rock pressure is used, we find that the porosity profiles are qualitatively and quantitatively similar. From the data we have for shale compaction after ten million years, we find that the inclusion of the rock pressure in the effective stress provides more accurate results than when only the lithostatic pressure is used. This may be due to being able to model more processes on the microscopic scale and thus including the direct interaction between the two phases. We conclude that using the rock pressure in the effective stress is an appropriate improvement over older models, and allows us to more accurately describe the compaction process.

In Chapter 5, we considered spatial additions to the basin in our simulations. We have been adamant throughout this thesis that we must simulate compacting basins in at least two dimensions. To support this claim, we obtained results for a basin undergoing laterally varying stresses at the top of the basin. Note that in reality, this will be the case as no basin will have a completely homogeneous stress acting across the basin. Hence, we allowed for the top stress to be laterally varying, without the added lateral variation being too significant. We found that with horizontally varying values of the stress, even a very small change in its value along the top of the basin resulted in a significant change in the behaviour of the basin profiles. The rock movement alone was significantly affected, and we found that the basin moves accordingly with the given stress at the top. The fluid movement is also affected significantly, on a magnitude scale similar to that of the rock. The remaining profiles also undergo some lateral variations within the basin, though it is not as noticeable. We conclude that it is crucial to model and simulate the basin in at least two dimensions in order to realistically model the basin evolution. Whilst the lateral variations in some profiles may not be significant, we have clearly seen that the domain deforms significantly in the lateral directions as well as the vertical, and that using alternative methods such as dividing the domain in multiple vertical strips will not be appropriate due to computational efficiency. As such, it is unrealistic to assume that compaction is a purely vertical process that can be resolve in a domain of vertical strips and

corresponding one-dimensional models, when lateral considerations clearly must be included for real geological simulations.

Faults are often modelled numerically, and we instead modelled their presence in the basin through the constitutive model for permeability. We assumed that along the fault line, the fluid is able to flow with ease and therefore the permeability is large. Then, the rock becomes exponentially less permeable as one moves away from the fault line. The first important finding to support our previous claim is that two dimensions are required to model the basin realistically. Even with a vertically placed fault line, the basin experiences changes horizontally. We find that in this case, there is a small change qualitatively in the movement of the two phases, but compaction takes place similar to before. However, when a diagonal fault is used where the fault line is present across the entire basin, we find that the domain undergoes compartmentalisation. We find that the fluid is unable to escape from below the fault line, and that compaction below the fault becomes a more difficult process than normal. This is in line with what is found in real basins, and we conclude that our method is appropriate for modelling the fault.

Finally, sills were modelled in our system via a source term in our energy equation for the temperature. We observed that the large heat flux across a layer in the basin resulted in a large temperature rise throughout the entire basin. However, the temperature (relatively) quickly subsides toward its standard profile in the absence of sills. From the inclusion of the sill, we observed that the porosity is highly affected by the temperature. This was likely due to the rock viscosity being sensitive to the temperature, which in turn highly affects the porosity, in agreement with our previous findings on the effects of rock viscosity on compaction. Another important difference in our model to those found in literature was the coupling of the temperature into the full system, which permits the inclusion of sills in our model which otherwise would not be possible without this thermal coupling.

6.3 Possible directions for future work

Real geological processes in sedimentary basins are difficult to model and observe. Experimental data in laboratories may suggest that certain mechanisms can be neglected, but small-scale observations may not provide sufficient insight on the basin-scale. In this thesis, we have shown that small changes in the parameter values can highly affect the compaction behaviour. Hence, we believe that it is of industrial interest to properly model processes like cementation (perhaps by modelling the rock viscosity

to be dependent on porosity, rock velocity, and time). Also, we presented numerous different constitutive equations one may use for different lithological situations. It may be of interest to simulate the basin evolution using a wide range of these models to observe the differences between the effects of each situation.

In addition to possible mathematical extensions, improvements might be made on the numerical implementation of the systems. A different numerical method, where one does not separate the model into subsystems, may be used to solve our model. To solve the full model without splitting into subsystems, we will need a nonlinear solving scheme such as Newton's method (see Deuflhard (2011) for its history and review of modern Newton algorithms), and iterative methods such as the linear conjugate gradient method (Shewchuk, 1994) in combination for each Newton step. These mentioned algorithms as well as many more are well-documented and can be applied with `deal.ii`, and therefore would be appropriate. Indeed, an example solving Darcy- or Stokes-type systems using a linear conjugate gradient method with a Schur complement via `deal.ii` already exists (Bangerth et al., 2016).

In this thesis, we do not delve into the stability of our time-discretisation scheme for the porosity and temperature equations, and also make assumptions that allow us to use the scheme we use. We may consider the use of a coupled time-integration method, following the ideas presented by Feldman and Gelfgat (2009) for incompressible Navier-Stokes equations or by Muscat et al. (2019) for compressible unsteady flows. We use a direct solver to obtain our results, where more sophisticated methods might improve efficiency and tackle many more processes at once. For example, Alternatively, we may use an iterative solver

Further, whilst using `deal.ii` is appropriate for simpler cases like ours, more complicated situations involving more complex geometries in particular would require further tools. Whilst it is robust in computing solutions for simpler models, simulating the basin can only be done on a basic level. For example, it is not easy to resolve discontinuous domains or to modify the mesh correctly if we were to use compartmentalisation. Further, it would be difficult to simulate a basin with multiple geological features in separate parts of the basin domain. PDS have knowledge and access to more numerical techniques and tools that may be appropriate for more complex scenarios, and it may be of interest to apply these to our model.

A more complete modelling of geological faults could be beneficial. For example, in our modelling of faults, our fault line was assumed to be composed of both rock and fluid, whereas in reality, only fluid would exist there. To more accurately model this, we need a better handling of the geometries and the locations where different

phases are defined. More sophisticated numerical tools may again be useful. Further, a sill may act to change the material properties of rock within and surrounding it, and such changes were omitted in our model. We considered each spatial feature (faults and sills) separately, and for a more realistic and complete basin, it would eventually be important to consider the features together in one single basin, which is a simple generalisation to our results. Of course, it is of industrial interest to model as many features as possible to recreate real basins.

Bibliography

P. A. Allen and J. R. Allen. *Basin Analysis: Principles and Application to Petroleum Play Assessment*. Wiley, 3rd edition, 2013. ISBN 9781118450444.

R. N. Anderson. Oil production in the 21st century. *Scientific American*, 3:86–91, 1998.

C. L. Angevine and D. L. Turcotte. Porosity reduction by pressure solution: A theoretical model for quartz arenites. *Geological Society of America Bulletin*, 94: 1129–1134, 1983.

P. Arbenz. Introduction to finite elements and sparse linear system solving. Technical report, ETH Zürich, 2017. `http://people.inf.ethz.ch/arbenz/FEM17`.

M. Artemyev. Tethex. Technical report, Belarusian State University, 2016. `https://github.com/martemyev/tethex/wiki`.

L. F. Athy. Density, porosity, and compaction of sedimentary rocks. *AAPG Bulletin*, 14(1):1–24, 1930.

D. M. Audet. Mathematical modelling of gravitational compaction and clay dehydration in thick sediment layers. *Geophysical Journal International*, 122:283–298, 1995.

D. M. Audet and A. C. Fowler. A mathematical model for compaction in sedimentary basins. *Geophysical Journal International*, 110:577–590, 1992.

D. M. Audet and J. D. C. McConnell. Foward modelling of porosity and pore pressure evolution in sedimentary basins. *Basin Research*, 4:147–162, 1992.

M. J. Baines, M. E. Hubbard, and P. K. Jimack. Velocity-based moving mesh methods for nonlinear partial differential equations. *Communications in Computational Physics*, 10(3):509–576, 2011.

S. Balay, S. Abhyankar, M. F. Adams, J. Brown, P. Brune, K. Buschelman, L. Dalcin, A. Dener, V. Eijkhout, W. D. Gropp, D. Karpeyev, D. Kaushik, M. G. Knepley, D. A. May, L. Curfman-McInnes, R. T. Mills, T. Munson, K. Rupp, P. Sanan, B. F. Smith, S. Zampini, and H. Zhang. PETSc Web page, 2019. `https://www.mcs.anl.gov/petsc`.

W. Bangerth, G. Kanschat, T. Heister, and M. Maier. `deal.ii` documentation. Available online, 2016. `https://www.dealii.org/8.4.1/doxygen/deal.II/modules.html`.

W. Bangerth, G. Kanschat, T. Heister, and M. Maier. SparseDirectUMFPACK class reference. Available online within `deal.ii` documentation, 2019. `https://www.dealii.org/current/doxygen/deal.II/classSparseDirectUMFPACK.html`.

R. W. Bentley. Global oil & gas depletion: an overview. *Energy Policy*, 30(3):189–205, 2002.

D. Bernaud, L. Dormieux, and S. Maghous. A constitutive and numerical model for mechanical compaction in sedimentary basins. *Computers and Geotechnics*, 33: 316–329, 2006.

K. Bitzer. Two-dimensional simulation of clastic and carbonate sedimentation, consolidation, subsidence, fluid flow, heat flow and solute transport during the formation of sedimentary basins. *Computers and Geosciences*, 25(4):431–447, 1999.

K. Bjørlykke and P. K. Egeberg. Quartz cementation in sedimentary basins. *AAPG Bulletin*, 77:1538–1548, 1993.

D. Boffi, F. Brezzi, L. Gastaldi, L.F. Demkowicz, R.G. Durán, R.S. Falk, and M. Fortin. *Mixed Finite Elements, Compatibility Conditions, and Applications: Lectures given at the C.I.M.E. Summer School held in Cetraro, Italy, June 26 — July 1, 2006.* Springer Berlin Heidelberg, 2008. ISBN 9783540783190.

F. Brezzi and R. S. Falk. Stability of higher-order Hood-Taylor methods. *SIAM Journal on Numerical Analysis*, 28(3):581–590, 1991.

F. Brezzi and M. Fortin. *Mixed and Hybrid Finite Element Methods*. Springer-Verlag New York, Inc., New York, NY, USA, 1991. ISBN 0387975829.

C. J. Campbell and J. H. Laherrère. The end of cheap oil. *Scientific American*, 3, 1998.

R. T. Coates and M. Schoenberg. Finite-difference modeling of faults and fractures. *Geophysics*, 60(5):1514–1526, 1995.

A. Costa. Permeability-porosity relationship: A reexamination of the Kozeny-Carman equation based on a fractal pore-space geometry assumption. *Geophysical Research Letters*, 33(2):1–5, 2006.

P. Deuflhard. *Newton Methods for Nonlinear Problems: Affine Invariance and Adaptive Algorithms*. Springer Publishing Company, Inc., 2011. ISBN 364223898X.

P. A. Domenico and V. V. Palciauskas. Thermal expansion of fluids and fracture initiation in compacting sediments. *Geological Society of America Bulletin*, 90: 953–979, 1979.

J. Donea and A. Huerta. *Finite Element Methods for Flow Problems*, chapter 2, pages 33–78. John Wiley & Sons, Ltd, 2005. ISBN 9780471496663.

D. A. Drew and L. A. Segel. Averaged equations for two-phase flows. *Studies in Applied Mathematics*, 50(3):205–231, 1971.

Y. Feldman and A. Gelfgat. On pressure–velocity coupled time-integration of incompressible Navier–Stokes equations using direct inversion of Stokes operator or accelerated multigrid technique. *Computers & Structures*, 87(11):710–720, 2009.

A. C. Fowler and X-S. Yang. Fast and slow compaction in sedimentary basins. *SIAM Journal on Applied Mathematics*, 59(1):365–385, 1998.

A. C. Fowler and X-S. Yang. Pressure solution and viscous compaction in sedimentary basins. *Journal of Geophysical Research*, 104(B6):12989–12997, 1999.

T. Gerya. *Introduction to Numerical Geodynamic Modelling*. Cambridge University Press, 2010. ISBN 9780521887540.

M. R. Giles, S. L. Indrelid, and D. M. D. James. Compaction - the great unknown in basin modelling. In S. J. Duppenbecker and J. E. Iliffe, editors, *Basin Modelling: Practice and Progress*, pages 15–43. Geological Society London, Special Publications, 1998.

O. Gonzalez and A. M. Stuart. *A First Course in Continuum Mechanics*. Cambridge Texts in Applied Mathematics. Cambridge University Press, 2008. ISBN 9780521714242.

M. Gutierrez and M. Wangen. Modeling of compaction and overpressuring in sedimentary basins. *Marine and Petroleum Geology*, 22:351–363, 2005.

M. F. A. Halim. Geothermics of Malaysian sedimentary basins. *Geological Society of Malaysia Bulletin*, 36:163–174, 1994.

T. Hantschel and A.I. Kauerauf. *Fundamentals of Basin and Petroleum Systems Modeling*. Earth and Environmental Science. Springer Berlin Heidelberg, 2009. ISBN 9783540723189.

H. D. Hedberg. The effect of gravitational compaction on the structure of sedimentary rocks. *AAPG Bulletin*, 10(11):1035–1072, 1926.

H. D. Hedberg. Gravitational compaction of clays and shales. *Americal Journal of Science*, 31(184):241–287, 1936.

K.-I. Horai. Thermal conductivity of rock-forming minerals. *Journal of Geophysical Research*, 76(5):1278–1308, 1971.

J. M. Hunt. Generation and migration of petroleum from abnormally pressured fluid compartments. *AAPG Bulletin*, 74(1):1–12, 1990.

M. Izadi. Streamline diffusion method for treating coupling equations of hyperbolic scalar conservation laws. *Mathematical and Computer Modelling*, 45(1):201–214, 2007.

D. W. Kelly, J. P. De S. R. Gago, O. C. Zienkiewicz, and I. Babuška. A posteriori error analysis and adaptive processes in the finite element method: Part I–error analysis. *Int. J. Num. Meth. Engrg.*, 19:1593–1619, 1983.

M. King Hubbert and W. W. Rubey. Role of fluid pressure in mechanics of overthrust faulting. *Bulletin of The Geological Society of America*, 70:115–166, 1959.

A. Kjeldstad, H. P. Langtangen, J. Skogseid, and K. Bjørlykke. *Simulation of Sedimentary Basins*, pages 611–658. Springer Berlin Heidelberg, Berlin, Heidelberg, 2003. ISBN 9783642182372.

G. Korvin. Shale compaction and statistical physics. *Geophysical Journal of the Royal Astronomical Society*, 78(1):35–50, 1984.

K. J. Laidler. The development of the Arrhenius equation. *Journal of Chemical Education*, 61(6):494, 1984.

T. E. Lee, M. J. Baines, and S. Langdon. A finite difference moving mesh method based on conservation for moving boundary problems. *Journal of Computational and Applied Mathematics*, 288:1–17, 2015.

X. Luo and G. Vasseur. Contributions of compaction and aquathermal pressuring to geopressure and the influence of environmental conditions. *AAPG Bulletin*, 76(10): 1550–1559, 1992.

D. M. Mann and A. S. Mackenzie. Prediction of pore fluid pressures in sedimentary basins. *Marine and Petroleum Geology*, 7:55–65, 1989.

A. Masud and T. J. R. Hughes. A stabilized mixed finite element method for Darcy flow. *Computer Methods in Applied Mechanics and Engineering*, 191(39):4341–4370, 2002.

D. McKenzie. The generation and compaction of partially molten rock. *Journal of Petrology*, 25(3):713–765, 1984.

C. Morency and J. Tromp. Spectral-element simulations of wave propagation in porous media. *Geophysical Journal International*, 175(1):301–345, 2008.

L. Muscat, G. Puigt, M. Montagnac, and P. Brenner. A coupled implicit-explicit time integration method for compressible unsteady flows. *Journal of Computational Physics*, 398:108883, 2019.

C. E. Neuzil. How permeable are clays and shales? *Water Resources Research*, 30(2): 145–150, 1994.

H. W. Olsen. Hydraulic flow through saturated clays. *Clays and Clay Minerals*, 9(1): 131–161, 1960.

M. J. Osborne and R. E. Swarbrick. Mechanisms for generating overpressure in sedimentary basins: A reevaluation. *AAPG Bulletin*, 81(6):1023–1041, 1997.

H. Pape, C. Clauser, and J. Iffland. *Fractals and Dynamic Systems in Geoscience*, chapter Variation of permeability with porosity in sandstone diagenesis interpreted with a fractal pore space model, pages 603–619. Birkhäuser Basel, 2000. ISBN 9783034884303.

S. J. Pirson. *Handbook of well log analysis for oil and gas formation evaluation.* Prentice-Hall, Inc., Englewood Cliffs, New Jersey, 1963.

L. Recker. A roadcut at the entrance to Arches National Park in Utah exposes a normal fault related to solution of salt beneath the region, 2013. Available at `https://uk.pinterest.com/pin/157485318191512065/`.

H. H. Rieke and G. V. Chilingarian. *Compaction of argillaceous sediments*. Chapter 3. Elsevier Science, 1974. ISBN 9780080869278.

P. J. Roache. *Verification and Validation in Computational Science and Engineering*. Hermosa Publishers, 1998. ISBN 9780913478080.

F. Schneider, J. L. Potdevin, S. Wolf, and I. Faille. Mechanical and chemical compaction model for sedimentary basin simulators. *Tectonophysics*, 263:307–317, 1996.

J. G. Sclater and P. A. F. Christie. Continental stretching: An explanation of the post mid-cretaceous subsidence of the central north sea basin. *Journal of Geophysical Research*, 85:3711–3739, 1980.

W. Senior, S. Kole, and R. Groenenberg. Data supplied by Petrotechnical Data Systems. Private communication, 2016.

J. M. Sharp. Momentum and energy balance equations for compacting sediments. *Mathematical Geology*, 8(3):305–322, 1976.

J. M. Sharp and P. A. Domenico. Energy transport in thick sequences of compacting sediment. *Geological Society of America Bulletin*, 87(3):390–400, 1976.

J. R. Shewchuk. An introduction to the conjugate gradient method without the agonizing pain. Technical report, Carnegie Mellon University, 1994.

Y. Shi and C-Y. Wang. Pore pressure generation in sedimentary basins: Overloading versus aquathermal. *Journal of Geophysical Research*, 91(B2):2153–2162, 1986.

I. Shimizu. Kinetics of pressure solution creep in quartz: theoretical considerations. *Tectonophysics*, 245:121–134, 1995.

J. E. Smith. The dynamics of shale compaction and evolution of pore-fluid pressures. *Mathematical Geology*, 3(3):239–263, 1971.

M. A. Speece, T. D. Bowen, L. Folcik, J, and H. N. Pollack. Analysis of temperatures in sedimentary basins: the Michigan basin. *Geophysics*, 50(8):1318–1334, 1985.

R. E. Swarbrick, M. J. Osborne, and G. S. Yardley. Comparison of overpressure magnitude resulting from the main generating mechanisms. *AAPG Memoir*, 76: 1–12, 2002.

R. Tada and R. Siever. Pressure solution during diagenesis. *Annual Review of Earth and Planetary Science*, 17:89–118, 1989.

L. Tobiska and R. Verfürth. Analysis of a streamline diffusion finite element method for the Stokes and Navier-Stokes equations. *SIAM Journal on Numerical Analysis*, 33(1):107–127, 1996.

P. Ungerer, J. Burrus, P.Y. Doligez, P.Y. Chénet, and F. Bessis. Basin evaluation by integrated two-dimensional modeling of heat transfer, fluid flow, hydrocarbon generation, and migration. *AAPG Bulletin*, 74:309–335, 1990.

R. Verfürth. Error estimates for a mixed finite element approximation of the Stokes equations. *ESAIM: Mathematical Modelling and Numerical Analysis - Modélisation Mathématique et Analyse Numérique*, 18(2):175–182, 1984.

O. Walderhaug. Kinetic modeling of quartz cementation and porosity loss in deeply buried sandstone reservoirs. *AAPG Bulletin*, 80(5):731–745, 1996.

O. Walderhaug, P. A. Bjórkum, P. H. Nadeau, and O. Langnes. Quantitative modelling of basin subsidence caused by temperature-driven silica dissolution and reprecipitation. *Petroleum Geoscience*, 7:107–113, 2001.

M. Wangen. Pressure and temperature evolution in sedimentary basins. *Geophysical Journal International*, 110:601–613, 1992.

M. Wangen. Modeling porosity evolution and cementation of sandstones. *Marine and Petroleum Geology*, 15:453–565, 1998.

M. Wangen. Generation of overpressure by cementation of pore space in sedimentary rocks. *Geophysical Journal International*, 143:608–620, 2000.

M. Wangen. A quantitative comparison of some mechanisms generating overpressure in sedimentary basins. *Tectonophysics*, 334:211–234, 2001.

M. Wangen. Communication between overpressured compartments. *Geofluids*, 1(4): 273–287, 2002.

M. N. Yalçin. Basin modeling and hydrocarbon exploration. *Journal of Petroleum Science and Engineering*, 5:379–398, 1991.

X-S. Yang. *Mathematical modelling of compaction and diagenesis in sedimentary basins*. PhD thesis, University of Oxford, 1997.

X-S. Yang. Pressure solution in sedimentary basins: effect of temperature gradient. *Earth and Planetary Science Letters*, 176:233–243, 1999.

X-S. Yang. Modeling mineral reactions in compacting sedimentary basins. *Geophysical Research Letters*, 27(9):1307–1310, 2000.

X-S. Yang. Density-driven compaction and temperature evolution in porous media. *Applied Mathematics and Computation*, 126:243–254, 2002.

G. S. Yardley and R. E. Swarbrick. Lateral transfer: a source of additional overpressure? *Marine and Petroleum Geology*, 17:523–537, 2000.